UiT The Arctic University of Norway

Faculty of Science and Technology
Department of Physics and Technology

Optical remote sensing of water quality parameters retrieval in the Barents Sea

Muhammad Asim

A dissertation for the degree of Doctor of Philosophy (PhD), January 2023

Abstract

This thesis addresses various aspects of monitoring water quality indicators (WQIs) using optical remote sensing technologies. The dynamic nature of aquatic systems necessitates frequent monitoring at high spatial resolution. Machine learning (ML)-based algorithms are becoming increasingly common for these applications. ML algorithms are required to be trained by a significant amount of training data, and their accuracy depends on the performance of the atmospheric correction (AC) algorithm being used for correcting atmospheric effects. AC over open oceanic waters generally performs reasonably well; however, limitations still exist over inland and coastal waters. AC becomes more challenging in the high north waters, such as the Barents Sea, due to the unique in-water optical properties at high latitudes, long ray pathways, as well as the scattering of light from neighboring sea ice into the sensors' field of view adjacent to ice-infested waters.

To address these challenges, we evaluated the performances of state-of-the-art AC algorithms applied to the high-resolution satellite sensors Landsat-8 Operational Land Imager (OLI) and Sentinel-2 Multispectral Instrument (MSI), both for high-north (Paper II) and for global inland and coastal waters (Paper III). Using atmospherically corrected remote sensing reflectance (R_{rs}) products, estimated after applying the top performing AC algorithm, we present a new bandpass adjustment (BA) method for spectral harmonization of R_{rs} products from OLI and MSI. This harmonization will enable an increased number of ocean color (OC) observations and, hence, a larger amount of training data. The BA model is based on neural networks (NNs), which perform a pixel-by-pixel transformation of MSI-derived R_{rs} to that of OLI equivalent for their common bands. In addition, to accurately retrieve concentrations of Chlorophyll-a (Chl-a) and Color Dissolved Organic Matter (CDOM) from remotely sensed data, we propose in the thesis (Paper 1) an NN-based WQI retrieval model dubbed Ocean Color Net (OCN).

Our results indicate that R_{rs} retrieved via the Acolite Dark Spectrum Fitting (DSF) method is in best agreement with in-situ R_{rs} observations in the Barents Sea compared to the other methods. The median absolute percentage difference (MAPD) in the blue-green bands ranges from 9% to 25%. In the case

of inland and coastal waters (globally), we found that OC-SMART is the top performer, with MAPD <30% in the visible bands. It is also demonstrated that the proposed BA method achieves better spectral consistency between OLI and MSI-derived R_{rs} products for varying optical regimes than previously presented methods.

Additionally, to improve the analysis of remote sensing spectral data, we introduce a new spatial window-based match-up data set creation method which increases the training data set and allows for better tuning of regression models. Based on comparisons with in-water measured Chl-a profiles in the Barents Sea, our analysis indicates that the MSI-derived R_{rs} products are more sensitive to the depth-integrated Chl-a contents than near-surface Chl-a values (Paper I). In the case of inland and coastal waters, our study shows that using combined OLI and BA MSI-derived R_{rs} match-ups results in considerable improvement in the retrieval of WQIs (Paper III).

The obtained results for the datasets used in this thesis illustrates that the proposed OCN algorithm shows better performance in retrieving WQIs than other semi-empirical algorithms such as the band ratio-based algorithm, the ML-based Gaussian Process Regression (GPR), as well as the globally trained Case-2 Regional/Coast Colour (C2RCC) processing chain model C2RCC-networks, and OC-SMART.

The work in this thesis contributes to ongoing research in developing new methods for merging data products from multiple OC missions for increased coverage and the number of optical observations. The developed algorithms are validated in various environmental and aquatic conditions and have the potential to contribute to accurate and consistent retrievals of in-water constituents from high-resolution satellite sensors.

Acknowledgements

There are a number of people I would like to thank, for their kind support and help during this four-year of Ph.D. project.

I want to start by expressing my sincere gratitude to Katalin Blix, who is my main supervisor. I appreciate your guidance, valuable feedback, discussions, and encouragement during my work. I greatly value your advice and your willingness to assist me whenever I needed to talk. I appreciate your encouragement to help me widen my research perspective by attending conferences, workshops, and summer schools. It has been a pleasure to work with you. I am extremely grateful to Atsushi Matsuoka, my co-supervisor, for his invaluable contributions, insightful criticism, time, energy, and thorough review of the articles. Thank you for sharing your knowledge with me and providing me with useful data. Our conversations have been extremely valuable throughout the work. I look forward to our continued collaboration. I owe a lot of gratitude to Camilla Brekke, my co-supervisor, for giving me the opportunity to work on this project and for introducing me to the Earth Observation group, UiT. I am extremely thankful for your guidance, your reviews of my articles, and your continuous support. Special thanks to co-supervisor Marit Reigstad for data collection and discussions on marine biology. I would like to express the highest respect and profound thanks to my co-supervisor and director at CIRFA, Torbjrn Eltoft, for his supervision, support, correction of drafts, providing me with all resources necessary for data collection, and for creating a fantastic learning atmosphere in CIRFA.

I would also like to extend my thanks to Arif Mahmood, co-author of my first paper, for the correction of the draft and the useful discussions on the applications of machine learning in the project. Anthony Doulgeris, Group Leader of the Earth Observation group at UiT, and Malin Johansson should also be thanked for assisting me with my teaching responsibilities and providing server space for data processing. I must thank Saloua Chlaily, Debanshu Ratha, and Cornelius Patrick Quigley for proofreading my manuscripts. Special thanks to Vebjrn Karirasi and Thomas Kramer for helping me with programming at the beginning of my Ph.D. and to Sidrah Hafeez from Hong Kong Polytechnic University for suggestions and fruitful discussions.

I would also like to acknowledge the Nansen Legacy Project for financing this project. Thanks to the IMR and Kronprins Haakon teams for the data collection. Pål Gunnar Ellingsen deserves special thanks for his assistance in mounting the radiance sensors on the R/V Kronprins Haakon and processing the data. I would also like to thank Geir Antonsen and Andrea Schneider for helping me with administrative issues. Additionally, I want to thank all the members of CIRFA and the Earth observation group.

Finally, I would like to express my heartfelt gratitude to my family and friends for their support. I am sincerely thankful to my cousin, Ejaz Yousaf, for guiding me professionally as well as personally. Thank you to my wife Shaista Parveen and kids, Jaffer and Komail, and to my parents and siblings for their love, support, and patience.

Muhammad Asim
Tromsø, January 2023

Contents

List of Figures

List of Tables

List of Abbreviations

AC Atmospheric Correction

ACOLITE Atmospheric Correction for OLI 'lite'

ANNs Artificial Neural Networks

AOD Aerosol Optical Depth

BA Bandpass Adjustment

BRDF Bidirectional Reflectance Distribution Factor

C-PrOPS Compact-Propulsion Option for Profiling Systems

C2RCC Case 2 Regional CoastColour

CDOM Colored Dissolved Organic Matter

Chl-a Chlorophyll-a

CNNS Convolutional Neural Networks

CTD Conductivity-Temperature-Depth

DL Deep Learning

DNN Deep Neural Network

DOC Dissolved Organic Carbon

EM Electromagnetic

EO Earth Observation

ESA European Space Agency

FC Fully Connected

FOV FIELD OF VIEW

GANs Generative Adversarial Networks

GPR Gaussian Process Regression

HAB harmful algal bloom

HPLC high-performance liquid chromatography

ICOR Image correction for atmospheric effects

L8 Landsat 8

LH Line Height

LSR Least Squares Regression

LUT Look Up Table

MERIS Medium Resolution Imaging Spectroradiometer

MIZ Marginal Ice Zone

ML Machine Learning

MLP Multi-Layer Perceptron

MODIS Moderate Resolution Imaging Spectroradiometer

MODTRAN Moderate-Resolution Atmospheric Radiance and Transmittance

MSI Multispectral Instrument

NAP NonAlgal Particles

NDVI Normalized Difference Vegetation Index

NIR Near Infra Red

NNs Neural Networks

NPP Net primary Production

OC Ocean Color

OCN Ocean Color Net

OCSMART Ocean Color-Simultaneous Marine and Aerosol Retrieval Tool

OLCI Ocean and Land Color Instrument

OLI Operational Land Imager

PACE Plankton Aerosol Cloud ocean Ecosystem

POLYMER POLYnomial based approach applied to MERIS data

RF Random Forests

RGB Red, Green, Blue

RMSE Root Mean Squared Error

RMSLE Root Mean Squared Log Error

Rrs Remote Sensing Reflectance

RS Remote Sensing

RVR Relevance Vector Regression

S2 Sentinel 2

S3 Sentinel 3

SeaWiFS Sea Viewing Wide Field-of-view sensor

SNR Signal-to-Noise Ratio

SRF spectral Response Function

SVR Support Vector Regression

TIRS Thermal Infrared Sensor

TOA Top of Atmosphere

TSM Total Suspended Matter

UiT University of Tromsø

UTM Universal Transverse Mercator

WQI Water Quality Indicator

WRS World-Wide Reference System

1 Introduction

This chapter presents the motivation, objectives, proposed methodologies, and outline of the thesis.

1.1 Motivation

The Barents Sea is one of the largest pan-Arctic shelves, covering approximately 10% of the Arctic ocean [1]. It is one of the world's most productive oceans and supports up to 40% of the Arctic's primary production [2]. Besides, it is the home to Norway's richest commercial fisheries [3] and an important region for the exploration of petroleum and mineral resources [3].

In general, the northern Barents Sea is covered with sea ice during winter, while the southern parts remain sea ice-free. This is due to the influx of warm, salty, and nutrient-rich waters from the Atlantic ocean entering through the Norwegian Sea [4]. At the same time, it imports sea ice and freshwater from the Arctic Ocean in the northern Barents Sea [5]. Other freshwater enters primarily from the south, along the Norwegian coast, while the less saline waters from the Baltic Sea enter via the North Sea [6]. Due to its geographic location, the Barents Sea's northern region is characterized by an Arctic-dominated ecosystem, whereas the southern region is known for its subarctic communities due to an influence of Atlantic water [2, 7]. Recently, significant changes in ecosystem function and net primary productivity (NPP) have been observed in

the transitional Barents Sea as a result of ongoing global warming [8, 9]. On average, a decrease in sea ice extent has been seen over time in the Arctic and its surrounding waters [7]. Recently, an increase in phytoplankton seasonal growth has been observed in the northern Barents Sea [9]. The effect of rapidly changing physical and environmental conditions on primary productivity makes it vital to study the ecosystem of the transitional Barents Sea.

As a light-harvesting pigment in phytoplankton, Chlorophyll-a (Chl-a) concentration can be considered a proxy for phytoplankton biomass in the water columns [10]. An adequate amount of biomass is crucial for a healthy and productive aquatic ecosystem. However, excessive concentration of phytoplankton has a negative impact on fisheries, marine animals, the local economy, and public health [11]. Thus, it is crucial to monitor the content of Chl-a. Phytoplankton forms the bases of aquatic food webs [12] and can grow rapidly in a short period of time depending on the availability of solar radiation and nutrients. While Chl-a is a crucial parameter in estimating primary production, an excessive amount of Color Dissolved Organic Matter (CDOM) and Total Suspended Matter (TSM), primarily found in coastal and inland waters, absorbs and/or scatters incoming solar radiation and limits the penetration of photosynthetically available radiation. As a result, CDOM and TSM are important parameters in the study of primary productivity. Chl-a, CDOM, and TSM are considered significant water quality indicators (WQIs) as they provide useful information about the health of an aquatic environment [13, 14].

Due to the dynamic nature of aquatic systems, especially inland and nearshore coastal waters where high spatial and temporal variability in water constituents may exist, understanding their ecosystems requires temporally frequent sampling of these WQIs [15]. Traditional ship-based sampling is time-consuming, expensive, and conducted infrequently. On the other hand, satellite-derived remote sensing reflectance (R_{rs}) can be used to estimate WQIs based on the diagnosed R_{rs} signatures. Satellite remote sensing offers wide spatial coverage, repeated overpasses, and is relatively inexpensive.

Apart from known optical properties of water molecules, the optical properties of open oceanic waters are primarily determined by Chl-a absorption, with two major absorption peaks at 443 and 670nm determining the shape of the R_{rs} in the visible range of EM spectrum. In inland and coastal waters, these spectral features are also modulated by absorption and/or scattering by CDOM and TSM. Estimation of Chl-a is more challenging in the latter case [16] due to absorption by CDOM which absorbs solar radiation more strongly in the blue wavelengths and less in the green range, similar to Chl-a, and then decreases almost exponentially towards the near-infrared (NIR) regions [17]. As a result, waters with high CDOM concentrations alter the R_{rs} spectra, particularly in the blue wavelength, causing an overestimation of Chl-a concentrations. TSM on the

other hand influences the shape of R_{rs} via absorption and scattering, increases turbidity and governs the magnitude of the R_{rs} spectrum in general [18]. High concentrations of TSM may limit the availability of light to the lower water columns, and trap heat in the upper columns, which may cause harmful algal blooms (HABs) [19].

The most widely used algorithms to derive Chl-a from R_{rs} can be divided into two approaches: semi-analytical and empirical [13]. The former approach derives Inherent Optical Properties (IOPs) from R_{rs} followed by an estimation of Chl-a. In the latter method, a combination of R_{rs} at several wavelengths is explored to find some ratio that relates empirically to Chl-a concentrations. Previous studies have reported that the ratio of R_{rs} in the blue-green region (wavelength $\approx$ 443nm and 560nm) of EM spectrum, has a generally strong correlation with Chl-a content in clear waters, however, in inland and coastal waters, this frequently leads to an underestimation/overestimation [14, 20, 21]. An alternative approach to estimating Chl-a content in moderately turbid waters is using the ratio of R_{rs} in the NIR to red (absorption peak of Chl-a) [22, 23]. More details on the Chl-a algorithms using the NIR and red wavelengths can be found in [24]. These methods assume a negligible absorption by CDOM and Non-Algal Particles (NAP) in the red and NIR regions. However, the estimates are also affected by the backscattering by NAP, which affects the red-NIR region of the EM spectrum [13]. Furthermore, these approaches are not recommended for clearer waters where the R_{rs} in the red and NIR regions are not correlated to variations in Chl-a. This is partly due to the low signal-to-noise ratio (SNR) in the red and NIR region for oceanic waters.

In addition to the aforementioned challenges, Ocean Color (OC) remote sensing requires a robust Atmospheric Correction (AC) method for accurate retrieval of WQIs [25]. Although AC schemes for water applications have existed for decades, there is still room for improvement [26]. In general, AC over open oceanic waters provides relatively accurate estimates; however, large uncertainties in the estimation of atmospheric components e.g., aerosol types and concentrations, still exist over inland and coastal waters [27]. These uncertainties are enlarged in the high north due to larger atmospheric path radiance caused by higher solar zenith angles and adjacency of sea ice [28]. In addition, due to a lack of studies on the validation of existing AC methods in the high north, there is uncertainty associated with the validity of these methods. The Barents Sea experiences polar nights in the winter and is often covered by clouds in the summer. This limits the intility of optical remote sensing in the high north.

Observing biological phenomena like algal blooms from space, which can be highly dynamic in time and space, requires the acquisition of OC observations with short time intervals (2–3 days) at a high spatial resolution ($<$ 60m) [29]. The similar band design of Landsat-8 Operational Land Imager (OLI) and

Sentinel-2 Multispectral Instrument (MSI), allows to combine images from these sensors and may provide repeat observations in ~2.9 days at a spatial resolution of 10-60m [29, 30]. It should be noted that such a merging should take into account the differences in the sensor's specificity, including spectral and spatial characteristics, sun-sensor geometries, illumination conditions, differences in instrument calibrations, and different atmospheric states [31]. To address these empirical differences, correction factors between OLI and MSI-data products must be developed [32, 33].

The research presented in this thesis addresses questions related to the limitations of the Chl-a retrieval algorithms, the uncertainties in AC methods, low frequency revisit time for high-resolution satellite data for monitoring dynamic aquatic systems, especially in the high north, and consistent retrieval of downstream science products from multi-sensors (e.g., OLI and MSI). The main objectives of this study are outlined below.

1.2 Research Objectives and Contributions

1.2.1 Main Objectives

This thesis aimed at the accurate retrieval of WQIs from high-resolution satellite sensors, i.e., OLI and MSI, while considering the Barents Sea and global inland and coastal waters as study sites. Because of their low temporal resolution, 16 days for OLI and 5 days for MSI, our second objective was to increase the frequency of OC observations by merging the data products from these sensors. Considering the differences in OLI and MSI band characteristics and acquisition geometry, the third objective was to provide consistent retrieval of WQ products (e.g., Chl-a and CDOM) from OLI and MSI-derived R_{rs} images using a single retrieval algorithm.

In order to achieve the main objectives, the specific tasks are listed below:

- to develop robust ML-based WQ retrieval algorithms using these high-resolution satellite sensors for both high latitude waters, the Barents Sea as well as global and coastal, inland waters.

- to determine which algorithm(s) can deliver more reliable R_{rs} products using high-resolution satellite sensors, OLI and MSI, in the high north (hereinafter the Barents dataset), and global inland and coastal waters (hereinafter the global dataset) under diverse aquatic and environmental conditions.

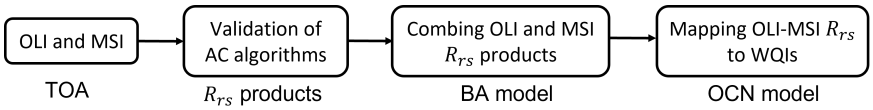

Figure 1.1: The Flow diagram of the proposed methodology.

- to spectrally harmonize R_{rs} products from OLI and MSI for consistent retrieval of aquatic data products, hence increasing the frequency of OC observations.

- to investigate the feasibility of in-water retrieval algorithms in estimating Ch-a and CDOM concentrations from harmonized OLI-MSI R_{rs} data from global waters using the retrieval models.

1.2.2 Proposed Approaches

Most of the OC algorithms (WQI retrieval algorithms) map atmospherically corrected R_{rs} into the concentrations of WQIs. Therefore, robust AC is essential for the estimation of downstream products such as R_{rs} and concentrations of WQIs from remotely sensed data. To achieve the main objectives listed above, we evaluated the performance of state-of-the-art AC algorithms to find the AC algorithm that estimates R_{rs} in agreement with in-situ R_{rs} data (the top-performing AC processor). To increase the frequency of OC observations from OLI and MSI, we proposed a neural network (NN)-based spectral bandpass adjustment (BA) method to harmonize OLI and MSI-derived R_{rs} products estimated via top-performing AC processor. Using the combined OLI and bandpass adjusted MSI-derived Rrs (MSI$^*Rrs$) products, we propose an ML-based model, dubbed Ocean Color Net (OCN), to estimate concentrations of Chl-a and CDOM from combined OLI and MSI images. Fig. 1.1 illustrates the flow diagram of the proposed methodology in this thesis. Below are the approaches proposed in papers I-III to achieve the overall objective of this thesis.

To achieve the first objective, an NN-based WQ retrieval algorithm was proposed for the Barents Sea (Paper I). The proposed OCN is based on a fully connected feed-forward Multi-Layer Perceptron (MLP). We investigated the architecture and capabilities of MLP-based deep artificial neural networks (ANNs) for ocean color monitoring applications in depth. The OCN model proposed in Paper I for the Barents dataset was tuned and validated on a global dataset in Paper III.

To investigate the source of uncertainties in the estimates of Chl-a concentrations in Paper I (mapping of R_{rs} to Chl-a) and due to the lack of in-situ

observations and studies on the validity of present AC methods in the Barents Sea, we collected ship-based above-water R_{rs} measurements using above water radiometers covering a large part of the Barents Sea (Paper II). Considering in-situ R_{rs} as ground truth, we evaluated the performance of state-of-the-art AC processors, Acolite, C2RCC, OC-SMART, ICOR, and Polymer to find the top-performing AC processor for the study region. The performance of these algorithms is validated on global inland and coastal waters (Paper III). The performance evaluation was carried out under diverse atmospheric and aquatic conditions.

To achieve the second objective, we assessed the spectral consistency between near-simultaneous OLI and MSI overpasses with a time difference of less than 30 minutes in terms of top of atmospheric (TOA) reflectance (ρ_t), and R_{rs} estimated via top performing AC processor, over the Barents Sea region. To harmonize OLI-MSI R_{rs} products, an NN-based spectral bandpass adjustment (BA) model was developed to spectrally adjust the MSI radiometry to replicate the spectral bandpasses of OLI for the common bands. The proposed algorithm is validated in different aquatic and environmental conditions covering a wide region of the Barents Sea (Paper II).

To achieve the third objective, we acquired near-simultaneous OLI and MSI TOA ρ_t products over coastal and inland waters globally. This data was corrected for atmospheric effects via the top-performing AC algorithm. The BA model developed in Paper II was used to harmonize OLI and MSI-derived ρ_w ($\pi \times R_{rs}$) products to acquire more match-ups (by combining OLI and BA MSI (MSI$*$ data), and thus better tune the retrieval models to estimate Chl-a and CDOM.

1.2.3 Contributions

The main contributions in this thesis are listed below:

- We collected ship-based above-water radiometric observations covering a wide region of the Barents Sea that had not been explored before.

- We evaluated the performance of five state-of-the-art AC methods against in-situ data using OLI and MSI images acquired over different optical regimes, the Barents dataset, and the Global datset.

- We developed an NN-based retrieval model, the OCN, for estimating WQIs from these high-resolution satellite sensors.

- To increase the frequency of OC observations and hence the number

of training examples for better tuning of the retrieval algorithms, an NN-based BA method is proposed for spectral harmonization of OLI and MSI-derived R_{rs} products.

- Utilizing the global dataset we demonstrated that by merging OLI-MSI derived ρ_w products using the proposed BA approach, all the retrieval algorithms exhibit improved performances in estimating Ch-a and CDOM compared to using OLI and MSI images alone.

1.2.4 Significance of the study

The significance of the study is based on the development of ML models for spectral harmonization of data products from high-resolution satellite sensors and retrieval of Chl-a and CDOM concentrations in different optical regimes, i.e., Arctic, inland, and coastal waters. In particular, to estimate Chl-a with considerably higher accuracy in the Arctic waters. The methods developed in this research are also beneficial for studying primary productivity in the Arctic ocean. The results from this research could potentially help policymakers make new policies and revise regulations regarding Arctic and coastal water quality monitoring. Additionally, this study details the applicability of various AC algorithms in the high north. Furthermore, the BA model developed in this study can be used to merge data products from multiple satellite sensors to increase the temporal frequency of OC observations.

1.3 Thesis Overview

This thesis comprises seven chapters.

Chapter 1 is an introductory chapter, which outlines the importance of water quality monitoring using remotely sensed data and highlights the associated challenges. It includes the objectives, proposed methodologies, and significance of the study.

Chapter 2 provides an overview of OC remote sensing, including optically activate WQIs and different satellite sensors that can be used for WQ monitoring.

Chapter 3 discusses AC methods, WQIs retrieval algorithms, including their significance and limitations, as well as the spectral harmonization of aquatic products derived from multiple satellite sensors.

Chapter 4 introduces ANN's theory relevant to this thesis, and introduces important concepts such as regularization and optimization of the NN model.

Chapter 5 provides brief information about the study regions and the in-situ data collection.

Chapter 6 provides a summary of the publications that contain the research contribution of this thesis.

Chapters 7–9 present the full papers.

Chapter 10 presents the conclusion, the general implications of this study in the Barents Sea, coastal and inland water quality monitoring, and future directions for research.

2

Ocean color remote sensing

OC remote sensing refers to the process of using sensors on satellites, aircraft, and ships, to measure the radiance originating from the water surface at multiple wavelengths. It is an effective tool for estimating near-surface concentrations of WQIs such as Chl-a in the open ocean [20, 34], coastal waters [12, 35], as well as inland waters [36, 37]. Nonetheless, OC remote sensing can be used for a variety of applications, e.g., primary productivity, phytoplankton absorption, and functional types, particle size distribution, climate change, as well as studying ocean biology and biogeochemistry from space, to name a few [38].

OC observations yield information on the amount and distribution of water constituents, which can provide useful information about the environmental state of the water body [12, 39, 40]. This measurement is related to the color of the water in the visible spectrum, which is affected by water constituents. These constituents include water molecules themselves, phytoplankton pigments, NAP, and fraction of dissolved organic carbon (DOC) [41]. Being able to extract these variables efficiently reinforces the ability of researchers to retrieve the quality and state of water bodies more effectively.

2.1 Overview of remote sensing of water quality

When incoming solar radiation, whose spectral properties are known, interacts with water molecules and constituents, two main processes take place: scattering and absorption [13] (see Fig. 2.1). The spectral properties of the solar radiation are altered depending on the scattering and absorption properties of the water body, which includes water molecules themselves as well as organic and inorganic dissolved matter present across the water columns [42]. OC remote sensing refers to the measurement of the variations in the spectral signature of solar radiation after interaction with optically significant water constituents, also called water leaving radiance (L_w). The magnitude and spectral shape of L_w normalized by solar irradiance (E_d) define the color of water, which in turn depends on the type and concentration of optically significant water constituents residing across the water columns. Thus, retrieving optically significant constituents from L_w (or reflectance signal), which is the backscattered light from the water body as a result of sunlight interaction with water molecules and constituents [27], is the goal of OC remote sensing.

Several algorithms have been developed to retrieve the concentration of optically significant WQ constituents from OC data, depending on the characteristics of the L_w signal and the property of interest. These algorithms can be classified into empirical [12, 21, 43, 44] or semi-analytical approaches [45, 46]. However, because of the scattering of light by the atmosphere in the satellite field of view (FOV), the total signal received by a satellite-borne sensor at the top of the atmosphere (TOA) (hereinafter referred to as L_t) contains a relatively small part of ($<$10%) of the L_w [26]. The remaining are the components of radiance from the atmosphere and the air-water interface. Fig. 2.1 shows the total received signal L_t at the TOA after interaction with water constituents and atmosphere. L_w, the useful signal which is used to estimate concentrations of WQIs, is retrieved from the satellite-received signal through a process called AC ([47]).

The goal for space-borne radiometers is to estimate L_w within 5% of the ground truth (true water leaving signal) and to derive biogeochemical variables within an acceptable uncertainty (e.g., Chla $\leq$ 35%) [49]. Hence, a well-calibrated sensor is required to prevent any lingering errors from propagating to the water-leaving signal [50]. This is possible through system vicarious calibrations [51]. Satellite OC sensors have been providing spatially and temporally comprehensive data for large-scale monitoring of oceanic, coastal, and inland waters. Along with various satellite sensors, some studies have used aerial and drone technologies for retrieving optically significant water constituents [52, 52]. However, this thesis limits the literature review to satellite-based remote sensing. The literature review is summarized as follows: i) Earth observation sensors, including their applicability, advantages, and limitations; ii) AC approaches

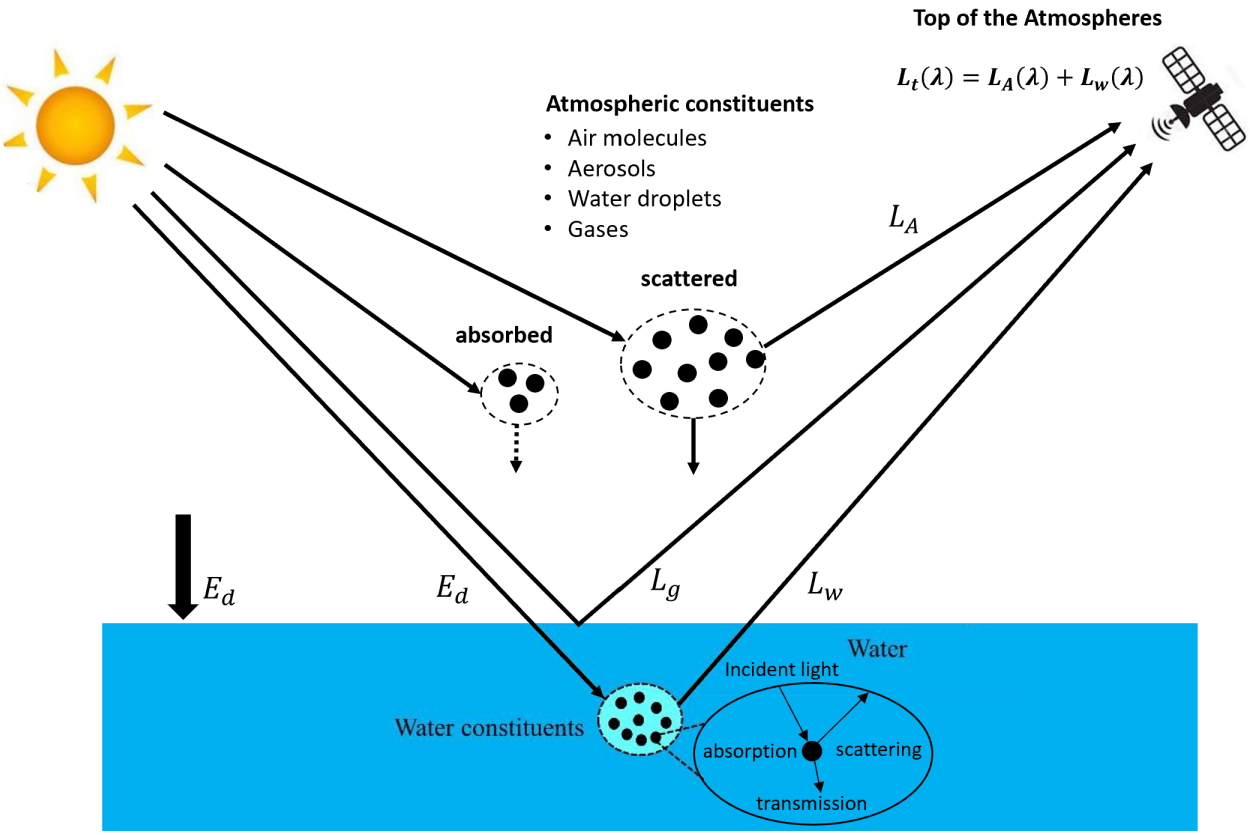

Figure 2.1: Principles of OC remote sensing [33, 48]. Here L_g is the radiance due to sun-glint and L_A represents radiance from atmospheric components.

for estimating L_w from the satellite received signal; iii) properties of optically active WQ constituents, followed by iv) retrieval approaches, and v) spectral harmonization of multi-sensor satellite products.

2.2 Optical satellite sensors

The first satellite sensor to measure OC was the Coastal Zone Color Scanner (CZCS), launched by the National Aeronautics and Space Administration (NASA) on the Nimbus-7 mission launched in 1978 [43]. The CZCS had bands centered at 443, 520, and 550nm to monitor the changes occurring in water-color with alterations in pigment concentration. After the launch, methods to remove atmospheric effects (Rayleigh and aerosol radiance) were refined. It was illustrated that open ocean reflectance could be accurately quantified [43]. With the success of the CZCS, several other missions were approved by different space agencies with additional bands in order to enhance performance and coverage, increase data accessibility, and develop better AC (aerosol estimation) algorithms. These sensors include the Sea Viewing Wide Field-of-view sensor (SeaWiFS) with mission life from 1997–2010, the Moderate Resolution Imaging Spectroradiometer (MODIS) 2002–present, the Geostationary Ocean Color Imager (GOCI) 2010–present, the Visible and Infrared Imager Radiometer Suite (VIIRS) 2012–present, the OLI onboard Landsat-8 2013-present, the Multispectral Imager (MSI) aboard Sentinel-2A 2015-present and Sentinel-2B 2017-present, Ocean and Land Color Imager (OLCI) onboard Sentinel-3A 2016-present and Sentinel-3B 2018-present [53, 54]. Some of the most well-known and widely referred sensors for global ocean color monitoring are shown in Table. 2.1. Using these sensors, various algorithms have been developed for estimating the concentration of WQ indicators from the open ocean to coastal waters depending on their spectral characteristics. In the following subsections, the suitability and limitations of satellite sensors used for OC are discussed.

2.2.1 Applicability

The most widely used operational satellite sensors used for OC monitoring are listed in Table. 2.1. The applicability of these sensors for water monitoring applications primarily depends on their radiometric design which includes, spectral coverage, band selection, spatial resolution and revisit time [51]. For instance, a spatial resolution of 300-1000m, with a higher spectral and temporal resolution, is adequate for open oceanic waters or large coastal areas. A sensor with such specifications can detect small changes in water leaving signals due to their higher number of bands, enabling the monitoring of dynamic

Table 2.1: Ocean Color Sensors.

Sensor	Spectral Bands [nm]	Spatial Resolution [m]	Bands	Revisit Time [days]
SeaWiFS	402-885	4000	8	1
MODIS-Terra	405-14385	250/500/1000	36	1-2
MODIS-AQUA	405-14385	250/500/1000	36	1-2
GOCI	400-865	500	8	1
Landsat-8	441-1384	15/30/100	9	16
Sentinel-2A	442-2202	10/20/60	13	10
Sentinel-2B	442-2202	10/20/60	13	10
Sentinel-3A	300-1200	400-1020	21	2.5
Sentinel-3B	400-1020	300/1200	21	2.5

processes that occur and vary over a short period of time. However, due to their coarse spatial resolution, these sensors are not suitable for studying changes occurring at a smaller spatial scale. For coastal and terrestrial applications, a higher resolution sensor such as OLI and MSI with spatial resolution ≤60m, is required especially for HABs detection and monitoring [51].

2.2.2 Limitations

Remote sensing of water quality by retrieving in-water constituents requires frequent revisits (e.g., daily) at a high spatial resolution (10-60m) [29, 32]. However, most of the existing ocean color satellites with high temporal resolution have coarse spatial resolution such as OLCI, MODIS, GOCI, VIIRS, Second generation global imager (SGLI), and the upcoming PACE Ocean Color Instrument (PACE-OCI). These satellite sensors have a spatial resolution of 250-1000m, which makes them unsuitable for detecting fine features in natural waters [55, 56]. In Contrast, high spatial resolution satellite sensors such as OLI with a spatial resolution of 30m and the MSI with 10-20-60m spatial resolution, have considerable potential for mapping Chl-a images with more spatial-detailed information not feasible with other OC satellites, however, these sensors have low-frequency revisit times of 16 and 5 days [30], not sufficient for near-daily monitoring of water surface [55]. The need for higher temporal resolution data to better monitor water resources is documented in several studies [29, 32, 57].

2.3 Optically Active Water Constituents

The most common optically significant WQIs are Chl-a, TSM, and CDOM [13]. The goal of OC remote sensing is to accurately retrieve the concentrations of these constituents from variations in the spectral shape and magnitude of the OC signal R_{rs}.

2.3.1 Optical properties of Chl-a

Phytoplankton biomass is a valuable indicator of the marine ecosystem's health [58]. A healthy and productive aquatic ecosystem requires an adequate amount of biomass. Depending on the availability of nutrients, the phytoplankton can grow rapidly in a short period of time in the presence of adequate sunlight [59]. The growth is also influenced by anthropogenic activities due to the runoff of nutrients such as nitrate and organic nitrogen, from urban and agricultural practices in water bodies, making estuaries, lakes, and reservoirs highly phytoplankton dominant [60]. The abnormally high growth of algae can reflect the state of eutrophication and has a negative impact on the aquatic ecosystem [11]. Dense algal blooms prevent sunlight from reaching organisms beneath, resulting in a decrease in dissolved oxygen across the water columns and, as a result, the suffocation of marine species living in the water body. [19, 61]. As a photosynthetic active pigment present in all algal species, the concentration of Chl-a is considered as a proxy for total phytoplankton biomass or primary productivity [62], therefore, it is critical to evaluate the exact concentrations of Chl-a.

The spectral shape and the magnitude of the Chl-a are mainly determined by light conditions, availability of nutrients, phytoplankton phenotypes and their concentrations in relation to other optically significant in-water constituents, for instance CDOM and TSM [63]. In oligotrophic to mesotrophic waters, Chl-a shifts watercolor from blue to dark green depending on its concentration. This is due to the strong absorption peak in the blue (around 443nm) and red 665nm regions of the spectrum by Chl-a and other pigments such as carotenoids and phycobiliproteins, compared to weak absorption in the green-yellow region (550-580nm) [64]. Thus, the Chl-a signature is described by the reflectance peak in the green region (560nm) or red edge region (around 680nm), also known as the sun-induced fluorescence peak of Chl-a which is due to photosynthetic processes [65]. In contrast, in eutrophic waters with excessive algal biomass, the fluorescence signal is altered by substantial absorption in the red region (670nm wavelength), and reflectance peaks around 710nm [45, 66, 67]. The 710nm band is found to be significantly correlated with Chl-a in high-biomass waters [68].

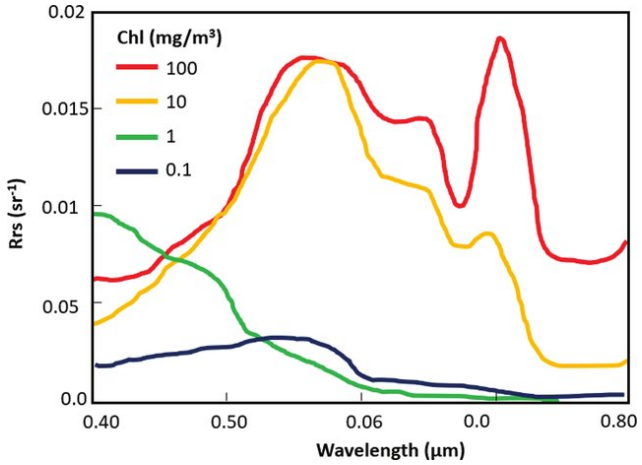

Figure 2.2: Change in the spectral response of water with varying concentrations of Chl-a [69].

In general, the optical properties of oceanic waters are primarily governed by Chl-a and its accessory pigments. CDOM and non-algal particles can all be present in open oceanic waters; however, their concentrations co-vary with phytoplankton concentrations [70, 71]. In inland and coastal waters, also called Case II waters, the color is modulated by the presence of other constituents such as organic and inorganic particles. In highly turbid waters, the variation in concentration of Chl-a has a negligible effect on water reflectance spectra as the optical properties are dominated by CDOM or TSM [68]. In such cases, the changes in CDOM and/or TSM concentrations are interpreted as changes in Chl-a. The optical properties of these aquatic systems are more complex, and Chl-a retrievals are more challenging [39, 72].

2.3.2 Optical properties of CDOM

CDOM is a colored and photo-active component present in natural waters, and is predominantly produced by anthropogenic activities as well as autochthonous and allochthonous causes [73]. It may be considered a proxy for DOC, which is the largest organic carbon pool in terrestrial and aquatic ecosystems [74]. In addition, it plays a significant role in the biogeochemical cycling of carbon in aquatic systems [13] and can be used as an indicator for the sustainability of aquatic systems for human use [73]. CDOM absorbs solar radiations in the ultraviolet (UV) and blue part of the EM spectrum (see Fig. 2.3), and tends to mask the Chl-a absorption peak at $443nm$. An excessive CDOM concentration can restrict light availability in the water column and hence the aquatic biomass [75]. Besides, CDOM absorption protects aquatic ecosystems from exposure to harmful UV solar radiation [76]. It affects the bio-optical properties of surface

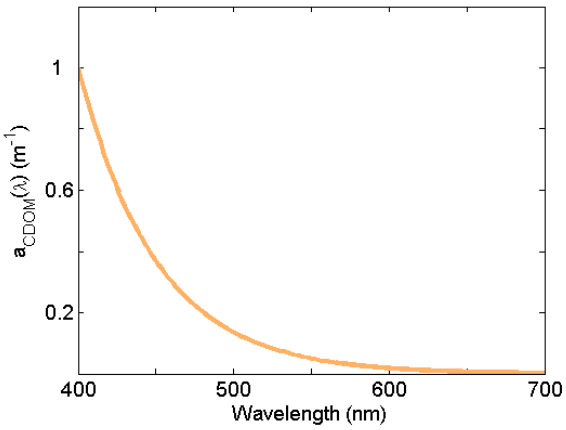

Figure 2.3: Generic CDOM absorption spectrum for mixed composition. [77].

water and is considered a useful indicator of water quality in complex aquatic systems.

High CDOM content can make it challenging to accurately estimate Chl-a and other constituents such as TSM. Due to its optical properties, CDOM concentrations can be estimated by remote sensing. In practice, the absorption coefficient of CDOM at 440nm, i.e., a_{CDOM} (440), is used as a proxy to estimate CDOM content through inversions algorithms [73, 78].

2.3.3 Optical properties of TSM

TSM in general consists of organic matter, such as phytoplankton, and inorganic matter, like clay and suspended particles, which reside in the water columns and influence turbidity. The main sources of TSM in coastal and inland waters are river runoffs, coastal erosion, dredging activities, polluting substances including heavy metals and nutrients, re-suspension events, and tidal currents [13, 79].

TSM absorbs and scatters sun light and governs the overall magnitude of R_{rs} spectrum. The optical properties of TSM depend on the particle size distribution and mineral composition [18]. The reflectance from sediment suspended in water increases with a decrease in particle size. In organic-dominated aquatic systems, the R_{rs} peak shifts from green (550nm) to red (665nm) or NIR region (865nm) of spectra depending on the concentrations of TSM and/ Chl-a and CDOM [80]. In contrast, R_{rs} in waters with an excessive amount of organic suspended solids is governed by the amount of algal biomass and share the pronounced absorption and scattering characteristic peaks as in phytoplankton

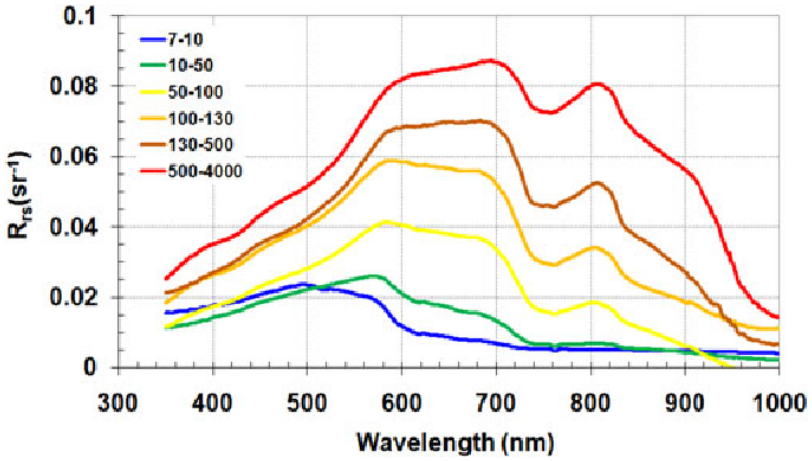

Figure 2.4: Averaged R_{rs} spectra for various TSM concentrations [80].

dominated waters [33, 81]. The variations in spectral shape and magnitude of R_{rs} with the increase in the TSM amount is illustrated in Fig. 2.4.

3 Algorithms

Chapter 2 provided an overview of OC remote sensing, optically significant WQIs as well as different satellite sensors that can be used for WQ monitoring. This chapter discusses AC of satellite images, Chl-a, and CDOM retrieval algorithms, including their significance and limitations, and the spectral harmonization of aquatic products derived from multi-sensors.

3.1 Atmospheric Correction

Ocean color remote sensing requires accurate AC for the retrieval of reliable WQIs such as Chl-a. Errors in AC lead to significant uncertainties in estimates of WQIs [29]. In addition, AC plays a critical role in the consistent retrieval of data products from multi-sensors (e.g., OLI and MSI) [12, 82]. This section briefly describes the theoretical background of AC, followed by a brief introduction to the AC schemes used in this study and the challenges associated with the correction of atmospheric effects.

The satellite received signal at the TOA contains $\leq$ 10% of L_w, and the remaining signal is contributed by different atmospheric factors [16]. The purpose of AC is therefore to remove the contribution of the photons that do not originate from the water column [27]. This includes radiance for sun-glint (the specular reflection of sunlight from the surface of the water), diffuse transmittances due to gases, Rayleigh (light scattering due to

air molecules), and aerosols (radiance due to small particles solid or liquid in suspension form). Other factors that may affect the received signal include cloud-adjacent stray light, large/low solar and viewing angles, and other non-ideal observing conditions such as cloud coverage [12, 53]. Observations under such conditions are considered defective and discarded by using quality flags `https://sentinel.esa.int/web/sentinel/technical-guides/sentinel-3-olci/level-2/quality-and-science-flags-op` described by the European Space Agency (ESA).

The remotely sensed aquatic signal recorded at the TOA reflectance is formulated following the methodology developed in [83].

$$\rho_t = \rho_r(\lambda) + \rho_a(\lambda) + \rho_{ra}(\lambda) + t\rho_w(\lambda) \tag{3.1}$$

where, ρ_t is the total reflectance measured by a satellite sensor at the TOA, ρ_r represents reflectance caused by scattering by air molecules in the atmosphere, also known as Rayleigh scattering in the absence of aerosols, ρ_a is the reflectance from aerosols in the air, ρ_{ra} is the interaction between molecular and aerosol scattering, t is the diffuse transmission, and ρ_w is the water leaving reflectance just above the ocean surface. Note that, for simplicity, reflectance due to sunglint and whitecaps is excluded from Eq. 3.1. Depending on the methodology adopted for AC, some studies have considered $[\rho_r(\lambda)+\rho_a(\lambda)+\rho_{ra}(\lambda)]$ as one unknown parameter, i.e., ρ_{path}, whereas other studies have treated ρ_r and ρ_a separately [27, 84]. Among the unknowns in Eq. 3.1, the most challenging task is to estimate the aerosol contribution. Small errors in the aerosols' size and type, may introduce errors in the retrieved ρ_w signal [27, 83]. Once ρ_w is accurately retrieved, it can be converted into R_{rs} using the methodology outlined in [85].

The AC in the open ocean, free of land and anthropogenic sources, is carried out with reasonable accuracy [86]. However, over inland and coastal waters, significant uncertainties exist in atmospherically corrected satellite products [26], especially in the strongly absorbing waters, the atmospheric path radiance ranges from >60% in sediment-rich waters to >94% in very dark waters [86]. These challenges are further escalated in the Arctic region due to long ray pathways caused by increased solar zenith angles and the scattering of light from neighboring sea ice into the sensor's FOV [87]. Errors in AC lead to significant uncertainties in the satellite-derived data products (Chla, CDOM, TSM) which limit its ability to detect subtle variations in aquatic ecosystems [12].

3.1.1 AC over Coastal and inland water

Several methods have been proposed for AC over open oceans for different satellite missions [86]. These approaches primarily differ in the methodology used in the estimation and removal of aerosols from the satellite-received signal [84, 88, 89]. Algorithms that utilize the black pixel assumption, assuming negligible L_w in the NIR band, and maritime (non- or weakly absorbing) aerosols as the dominant aerosol type, in general, work well over clear oceanic waters [26]. In inland and coastal waters with high concentrations of TSM, the black pixel assumption is often not valid due to non-zero water-leaving radiance in the NIR. AC over inland and coastal waters is made further complicated by other factors, such as i) scattering of light radiance from the neighboring terrestrial terrain that can also contribute to ρ_{path} [90], ii) the presence of aerosols from terrestrial sources, which causes an optically heterogeneous atmosphere and iii) aerosols from both terrestrial and marine sources, have the potential to create spatially variable and mixed conditions that are not always accurately reflected in current aerosol models [27, 91, 92].

Recent AC methods that use SWIR bands for aerosol retrieval have shown improved performance in sediment-dominated waters [26, 56]. However, to retrieve higher-quality downstream data products, further improvement in all the AC methods that are under development is expected over inland, coastal, and Arctic waters.

3.1.2 AC over Arctic water

OC remote sensing in the Polar seas is challenging due to a number of difficulties and intrinsic limitations which include i) the persistence of cloud coverage and fog which limits the use of OC remote sensing, ii) high solar zenith angles, often larger than the maximum (generally 70°) for which AC methods have been developed using radiative transfer modeling, iii) polar nights during the winter season, iv) the adjacency effect of the sea ice, which tends to increase ρ_t at shorter wavelength and of sub-pixel ice contamination, which increases overall spectra, and v) optical complexity of seawater due to high concentrations of CDOM and sub-surface chlorophyll maximum [87, 93].

The necessity of a precise AC method and the difficulties and intrinsic limitations of validating AC algorithms in the Polar seas are discussed in [94, 95].

3.1.3 AC algorithms

Several AC algorithms have been proposed to remove the atmospheric effects, however, the most widely used in oceanography are the Case-2 Regional Coast Color (C2RCC) processor [96], Ocean Color-Simultaneous Marine and Aerosol Retrieval Tool (OC-SMART) [97], Polymer from HYGEOS [98], Sen2Cor [99], Atmospheric Correction for OLI 'lite' (Acolite) [100,101], ICOR [102] and l2gen from NASA [50]. Excluding Polymer, these processors are broadly divided into two categories, i.e., the two-step and ML-based methods [27]. In the two-step methods, images are corrected for Rayleigh and gaseous absorption followed by the aerosol contribution. The main difference between the two-step approaches is the methodology adopted for removing the aerosol contribution. The two ML approaches, C2RCC and OC-SMART, are based on multi-layer NNs. These networks are trained on large synthetic datasets generated using in-water and atmospheric radiative transfer models. The ML methods do not depend explicitly on the evaluation of aerosol information [97].

In the present study, we have compared the performance of five publicly available state-of-the-art AC processors. Polymer v4.13 [98], Acolite python version 20211124.0 [101,103], C2RCC v1.0 [96], ICOR validated in [27] and OC-SMART [97].

The C2RCC processor is built upon previous AC algorithms, Case2Regional and CoastColour, and is based on the per-pixel ANN method. The network is composed of six hidden layers with 77 neurons each and a sigmoid activation function [96]. The C2RCC processor is assessed from the Sentinel Application Platform (SNAP) v6.0 processing toolbox provided by the European Space Agency (ESA) and run in its default settings except for salinity and temperature values.

Polymer is a polynomial-based AC algorithm that uses a polynomial function to decouple the reflected signal associated with the water body from atmospheric and sun glint contributions. This scheme uses a spectral matching method to simultaneously estimate both atmospheric and water components. After correcting for Rayleigh scattering, it decomposes the received signal into a water reflectance spectrum and an atmospheric reflectance spectrum. The Polymer scheme works well in areas affected by sun-glint.

The Acolite scheme is developed for processing high-spatial-resolution sensors such as Landsat-8 OLI and Sentinel-2 MSI [100]. Currently, it has two aerosol correction methods suitable for clear, mixed clear, and turbid waters, which are applicable to most OC sensors. In this work, we have used the recently developed dark spectrum fitting (DSF) scheme of Acolite [101,103]. The DSF method is exclusively an image based approach that corrects for the gas and

air-water interface reflectance followed by estimation of atmospheric path reflectance (ρ_{path}). The (ρ_{path}) is estimated within a targeted (sub)scene following two assumptions. i) the ρ_{path} is homogeneous over a scene or sub-scene, and ii) the scene contains pixels where reflectance is zero for at least one of the bands. Based on these two assumptions, the ρ_{path} is then estimated from those dark targets within the (sub)scene. These dark targets are chosen based on the lowest values of ρ_t across all bands. To account for the variations in the atmospheric effects over the scene, the satellite image is divided into several tiles with a size of $6km \times 6km$. Based on the assumption that (ρ_{path}) is constant over the tile, the (ρ_w) is estimated from each tile after removing the spatially constant (ρ_{path}). Finally, a linear interpolation is used for smoothing the parameters retrieved from different tiles [25, 103].

OC-SMART is an empirical scheme that is built upon multilayer NNs. It estimates R_{rs} and aerosol optical depth (thickness) (AOD) after correction for Rayleigh contributions. This scheme can be applied from fresh waters to highly turbid waters [25, 97]. However, the targeted area must have similar atmospheric and aquatic properties to those included in the training data [97].

Image correction for atmospheric effects (iCOR) is an image-based AC scheme that is primarily developed to process images collected over coastal, inland or transitional waters. The method uses the Moderate-Resolution Atmospheric Radiance and Transmittance Model-5 (MODTRAN5) to remove contributions from the atmosphere. This scheme divides the image into macro-pixels of $15 \times$ 15km and in each tile and exploits the spectral variation within a subset [102]. In the first retrieval step, it searches for the lowest radiance value within the tile for each spectral band. Based on the selected value, the lowest radiance, it estimates the corresponding path radiance from the approximated dark target spectrum using the pre-calculated MODTRAN5 look-up table (LUT). The path radiance closest to the dark spectrum is selected as the tile's upper AOT boundary. In the second step, the initial estimated AOT value is improved through a multi-parameter end-member inversion technique. To retrieve the surface reflectance, it selects five pixels with high spectral contrast depending on the values of the Normalized Difference Vegetation Index (NDVI) from TOA reflectance. These pixels are then represented by a linear combination of three spectra: two vegetation spectra and one soil spectra [102].

In this study, the performances of these AC processors are evaluated on inland, coastal and Arctic waters from open oceanic to inland and coastal waters.

3.2 Water constituents retrieval approaches

Estimating biogeochemical products such as Chl-a from OC measurements, multi-spectral R_{rs}, is by definition an inversion problem, where the function f^{-1} predicts the concentrations of these products using R_{rs} as an input, i.e., WQI=$f^{-1}(R_{rs})$ [12]. The widely used Chl-a retrieval algorithms may be divided into two categories: empirical and semi-analytical approaches respectively [70].

The empirical approaches use simple or multiple regressions between Chl-a and the ratio of R_{rs} at different wavelengths [104–107]. These algorithms do not require a full understanding of the relationship between R_{rs} and Chl-a; however, they generally perform well on waters with similar characteristics. Thus, their applicability is limited and may result in significant errors if the optical properties of water are different from those used in the algorithm's development. The main advantages of these algorithms are their simplicity and computational efficiency, which can be used to retrieve Chl-a content from larger datasets of satellite images [45].

The semi-analytic approaches derive the IOPs from R_{rs} followed by an estimation of Chl-a concentrations [45, 46, 108]. These algorithms are based on solutions to the radiative transfer equation and can be applied to different water types [108]. The retrieval accuracy is often superior to empirical methods; however, the performance of these algorithms rely on accurate spectral models for absorption coefficients for each constituent present in water (e.g., pigments, CDOM, suspended sediments) [45]. Furthermore, the optimization procedure is time-consuming.

The below subsection covers empirical approaches, which include band-ratio algorithms and ML-based algorithms.

3.2.1 Empirical Models

Empirical approaches use the estimates of phytoplankton absorption peaks in the blue and red regions of the EM spectrum [109, 110]. These approaches typically rely on R_{rs} band combinations in the blue-green or in the red and NIR portions of the spectrum.

Chl-a in open oceanic waters can be estimated using the ratio of the blue to the green band [110]. This approach assumes that the shape and magnitude of R_{rs} in the blue and green portions of the spectrum are primarily governed by Chl-a. In addition, these algorithms make the assumption that the influence of other organic and inorganic substances on R_{rs} is minimal or highly correlated

with the concentration of Chl-a [70]. Previous studies have shown that the blue-green ratio is sensitive to Chl-a concentrations in clear waters. However, in inland and coastal waters, where the R_{rs} spectrum is modulated by the presence of other optically active water constituents, causes an under/overestimation of Chl-a content [12, 40]. More recently, the OC algorithm which statistically relates the blue-green band ratio of $R_{rs}(\lambda)$ spectrum to Chl-a concentrations through a polynomial expression (hereafter OCx) is fine-tuned according to the spectral configuration of various satellite sensors such as SeaWiFS, MERIS, OLI [43].

Several other empirical formulations are also developed, which include the band ratio of *Rrs* in the red and NIR regions [105–107], the Line Height (LH) method [111], and hybrid methods [112].

The red-NIR band ratio methods assume negligible absorption by CDOM and NAP in the red and NIR region [68,106]. These algorithms are used to retrieve Chl-a concentrations in turbid and coastal waters using the ratio of the NIR band (which is associated with Chl-a fluorescence), to the red band (associated with Chl-a absorption). The fluorescence peak is usually related to sufficient phytoplankton biomass [106]. This approach has shown promising results in biomass retrieval in phytoplankton-dominant mesotrophic waters. However, the red-edge methods are not intended for use in waters with low Chl-a, where the reflectance in the red and NIR regions is not significant [113]. Some studies have reported improved performance using green-to-red band ratios [107, 114].

The LH approach uses Chl-a fluorescence LH to determine its concentration [111]. These methods typically utilize three bands, usually red or red-NIR band(s) to compute distinctive peaks in the R_{rs} spectrum that is associated with Chl-a [65, 66, 115]. Gower et al. reported a strong correlation of the height of the radiance peak at 685nm with the amount of Chl-a in the range from 1 to 20 mg/m^3 [116]. This approach was modified for different sensors, including SeaWiFS [117]. LH methods have shown good performance in the open ocean; however, their performance degrades in optically complex waters due to the presence of TSM and CDOM, which dominate the optical properties of these waters [117].

Hybrid methods combine two band-ratio algorithms i.e., blue-green and red-NIR bands depending on the optical complexity of water. These methods are based upon red or NIR bands, LH and band ratios [118]. These algorithms offer the ability to select appropriate algorithms depending on the water-type to ensure an optimal retrieval of Chl-a over vast biomass ranges. For example, switching between the green-blue ratio algorithm, which retrieves low Chl-a, and the red-NIR algorithm, which retrieves high Chl-a, is based on the 708 and

665nm reflectance ratio. However, these algorithms require regional tuning depending on the optical properties of water. Therefore, the performance of these algorithms degrades in other waters, especially coastal and complicated waters. In addition, the performance of these algorithms is also dependent on the spectral bands of the sensor. For instance, due to the limited number of spectral bands of OLI, the band ratio methods are not ideal for estimating Chl-a in highly turbid waters using data from this sensor [62].

3.2.2 Machine learning models

Recently, with the increasing popularity of ML techniques in remote sensing, several studies have used ML-based models for the retrieval of WQIs [21,39,44]. The most widely explored empirical methods based on ML include ANNs [119], Support Vector Regression (SVR) [120], Relevance Vector Regression (RVR) [121], Random Forests (RF) [122] and Gaussian Process Regression (GPR) [123]. A review on ocean color monitoring using these algorithms is given in recent studies [39,124,125].

Several studies have reported superior performance of ML methods in estimating WQIs from a variety of water conditions, ranging from open oceanic to turbid waters. For example, Pahvalan et al. demonstrated that the Mixture Density Networks (MDN) model outperformed band ratio-based algorithms and other empirical approaches for different water types using remotely sensed data from Landsat-8 OLI, Sentinel-2 MSI, Sentinel-3 OLCI [12]. The NNs developed for optically complicated water types have overcome some of the issues encountered with the band ratio and semi-analytical approaches when evaluated over large Chl-a ranges [12,13,126].

3.2.3 Thesis Approach: Deep Neural Networks

ANNs have previously been used in various applications, such as computer vision and medical image processing [127–129] as well as remote sensing of WQIs [12, 39, 130]; however, to the best of our knowledge, limited studies have been conducted to explore the efficiency of ANNs in the domain of OC monitoring in the high north.

3.3 Spectral Harmonization

Continuous fine-scale monitoring of WQ from space requires the acquisition of OC imagery with short time intervals (2-3 days) at a high spatial resolution

(<60m). However, the majority of the current Earth observation satellites with high temporal resolution have a coarse spatial resolution of ≥300-1000m, making them unsuitable for detecting fine features in natural waters, especially in small-sized lakes, rivers, and inland waters. On the other hand, satellite sensors with high spatial resolution, like the OLI on Landsat-8 and the MSI on Sentinel-2A/2B, have a considerably better potential to detect and characterize the spatial structures on the water surface relative to low-resolution satellite sensors. However, the low revisit frequency of OLI and MSI, 16 and 5 days, respectively, make them individually insufficient for nearly daily monitoring of the ocean surface [55]. In addition, the presence of clouds, shadows, and atmospheric effects limits ocean color observations; thus, the actual revisit time is sometimes longer than 16 and 5 days respectively. The infrequent temporal sampling can limit their applicability in applications that require near-daily observations [57].

The similar band designs of the OLI and MSI sensors allow combining their imagery at a spatial resolution of 10-60m which may provide a global median average return period of ~2.9 days. Considering cloud coverage, such small return intervals are necessary to capture the dynamics of nearshore coastal and inland seas [29].

3.3.1 Bandpass Adjustment

Although Landsat-8 OLI and Sentinel-2 MSI have the same band design and characteristics, they still have certain differences. These sensors have a different spatial resolution, spectral bandwidth, FOV, and spectral response function (SRF) [32, 131]. The differences in OLI-MSI data products induced by different spatial resolutions and FOV can be reduced by minimizing the bidirectional reflectance distribution factors (BRDF) [132]; however, the differences introduced by the SRF and the spectral bandwidth still pose a challenge for creating seamless OLI-MSI data products. The aforementioned differences cause inconsistencies in OLI-MSI R_{rs} and hence downstream data products such as Chl-a maps [31]. These inconsistencies may be further amplified by varying illumination, different acquisition geometries, as well as atmospheric and aquatic conditions due to the time-gap between the sensors' overpasses.

To harmonize OLI and MSI-derived data products into a single data set, correction factors must be introduced to mitigate the spectral discrepancies in their respective R_{rs} products [30].

3.3.1.1 Linear Bandpass Adjustment

To account for the disparities in the SRFs of MSI and OLI, most studies have used fixed per-band regression coefficients, generated using linear regression or least squares regression models, to bandpass adjust (BA) MSI radiometry to match the spectral bands of Landsat-8 OLI [32, 55, 131, 133, 134]. The linear transformation methods can reduce the reflectance differences to only some degree [135]. Some recent studies have presented non-linear transformation models, which are shown to perform well [82, 135].

3.3.1.2 Proposed Bandpass Adjustment

The proposed spectral BA method transforms the MSI-derived R_{rs} products to that of OLI. Since the R_{rs} products are given as an input to the BA model (see Fig. 3.1), the AC is a crucial step before the spectral harmonization of their products. To ensure realistic R_{rs} estimates from satellite images, we first compared the atmospherically corrected R_{rs} with in-situ observations using state-of-the-art AC processors. The AC algorithm which provides R_{rs} values in agreement with in-situ R_{rs} observations was then used to estimate R_{rs} products from near-simultaneous OLI and MSI images from the study region. Instead of using a linear adjustment to the MSI-derived R_{rs} products, we propose an ML-based BA model for spectral alignment of OLI and MSI-derived R_{rs} products. The flow chart of the proposed spectral harmonization method is shown in Fig. 3.1.

3.4 Summary of proposed NN models

In this thesis, we explored the efficiency of a fully connected MLP for two different applications of OC remote sensing: bandpass adjustment of MSI R_{rs} products (MSI$^*R_{rs}$) to combine OLI-MSI data products (Paper II and III) and the retrieval of WQIs (Paper I and III), as shown in Fig. 3.2. These applications differ in terms of input and output data, the number of input features, and the number of training examples. Therefore, the proposed models for these two applications are different in terms of architecture and the optimization of hyperparameters.

To estimate any measurable function between the input and output vectors, the choice of an appropriate set of connecting weights, the network's depth, the number of neurons in each hidden layer, the activation function, learning rates, the batch size, and regularization all play a critical role [44, 137]. In the current work, the architecture of MLP is explored for spectral harmonization of

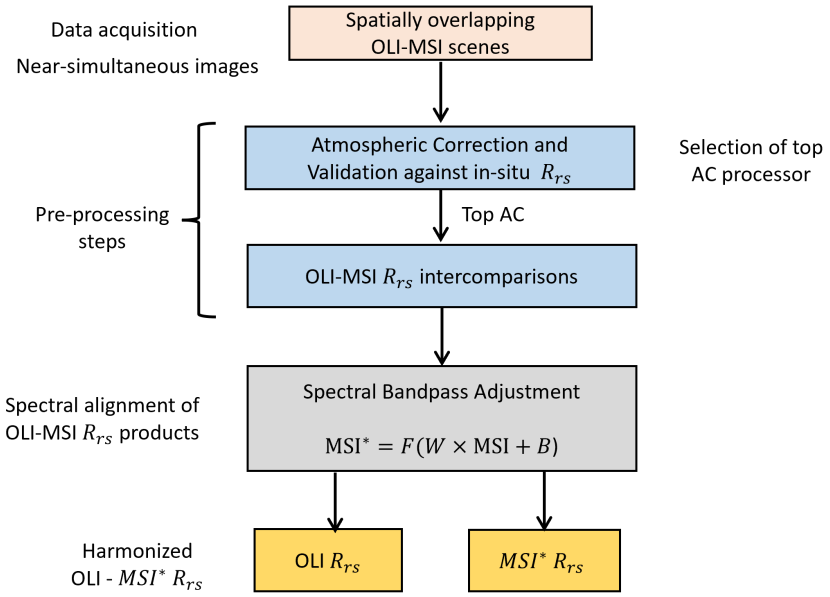

Figure 3.1: Flow chart of the proposed spectral harmonization approach [136]. W and B represents weights and biases of the BA model.

data products from multi-mission satellite sensors and retrieval of WQIs from open oceanic, coastal, and inland waters. The NN-based models are developed in TensorFlow in a Python environment. The following chapter is dedicated to basic ANN concepts.

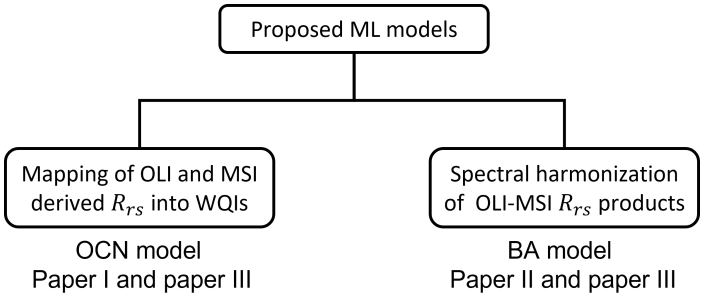

Figure 3.2: The NN-based models proposed in this thesis, the OCN and the BA model.

4

Artificial Neural Networks

The previous chapter provided an overview of state-of-the-art OC algorithms used for the retrieval of WQIs and spectral harmonization of multi-sensor data products, including their applicability and limitations. This chapter introduces ANN's theory, which forms the foundation of this thesis. In addition, it introduces important concepts such as the regularization and optimization of NN models.

4.1 Multilayer perceptrons

MLPs are a feed-forward NNs that are fully connected (FC). They form the foundation of deep learning algorithms. Formally, an MLP is a function F, that maps input data x to the output $y = F(x)$. Basically, the MLP learns the value of a parameter θ for mapping the input x to the output $\hat{y} = F(x;\theta)$. The parameter θ is adjusted to minimize the loss function L that quantifies the disagreement between the ground truth (y) and the estimated output ($\hat{y}$) [128, 137].

Mathematically, an MLP with one hidden layer can approximate the mapping of any continuous non-linear function [138]. NN learning algorithms that are built upon NNs with more than one layer between input and output are called deep neural networks (DNNs) [139]. In DNNs, in contrast to shallow learning, the majority of the model's parameters are learned from the outputs

of the preceding layers rather than directly from the input features of the training samples [139]. In the design of a NN, performance and computational complexity of the model play a crucial role [137, 139].

4.1.1 Architecture

The MLP is composed of a number of interconnected processing elements called nodes. In an MLP, the data flow in the forward direction, i.e., from the input layer to the output layer, and is trained using a back-propagation algorithm using forward and backward processes based on Eqs. 4.1-4.4. The input layer passes the input vector to the network, where each input value is weighted depending on its relative importance prior to entering the hidden layer [140]. The hidden layer receives the weighted input value from the input layer. It contains a varying number of neurons. The outputs of the neurons in the hidden layer are based on the linear sum of their inputs times their weights and biases. An activation function is then applied to the weighted sum of the outputs of each hidden layer. The activation of a neuron and its output are given by Eqs. (4.1) and (4.2).

$$a_i^l(x) = b_i^l + \sum_j^n w_{i,j}^l x_j \tag{4.1}$$

where $a_i^l(x)$ represents the total weighted sum of input x_j and weights $w_{i,j}^l$ of neuron i in layer l, including the bias term b_i^l. The neural network has parameters $(W, b) = (W^1, b^1, W^2, b^2)$, where $W_{i,j}^l$ denote the weights associated with the connection between neuron j in layer $l-1$ and neuron i in the layer l.

$$y_i^l(x) = \tanh(a_i^l(x)) \tag{4.2}$$

here $\tanh(\cdot)$ is an activation function. Depending on the type, the activation function maps each neuron's output between 0 and 1 or -1 and 1. It introduces a non-linearity into the output of a neuron, and that causes each neuron to either fire or not. Similarly, the output of the neurons in the hidden layer is then given as an input to the next hidden layer, which does a similar linear summation followed by a nonlinear activation function, or to the output layer to get the results. The output layer in our case performs regression; therefore, we keep it as a linear function.

4.1.2 Optimization

The optimization algorithm minimizes the loss function, which is the difference between the expected values (y_i) and the predicted values ($\widehat{y_i}$). The most commonly used loss function in regression is the root mean square error (RMSE). However, in this thesis, we used the root mean square log error (RMSLE) along with l_2 norm on the weights and the biases.

$$L = \sqrt{\frac{1}{N}\sum_{i=1}^{N}(\log_{10}(y_i) - \log_{10}(\widehat{y_i}))^2} + \lambda_1 \ell_2(W, b), \tag{4.3}$$

where N is the total number of training examples, and λ_1 is a hyperparameter that assigns relative importance to the second term in Eq. 4.3. Here $\log(\cdot)$ denotes the logarithmic function. The back-propagation algorithm typically employs the mini-batch gradient descent method to compute the gradients (g_t) of the cost function with respect to the network's weights and biases. The mini-batch gradient descent algorithm finds the model weights and coefficients that minimize the loss over a mini-batch while training, i.e. the hyper-parameters of the network are updated using n training samples (x_n, y_n), instead of a single or the complete training set [44]. The cost function at each time step t, is minimized as follows.

$$w_{t,n} = w_{t-1,n} - \eta g_{t,n}, \tag{4.4}$$

where $g_{t,n} = \nabla_w L$, and ∇_w is the gradient of the loss function L defined by Eq. 4.3. The loss function is differentiable with respect to weights. The parameter η is the learning rate, which represents the amount of change that is induced in the weights during each training iteration.

4.1.3 Regularization

The NN model may overfit the data and lose its ability to generalize if the network's capacity is sufficiently huge in comparison to the dataset. As a result, regularizing the model is frequently used to address over-fitting. The most commonly used regularization techniques are discussed in this section. A thorough overview of different regularization methods used in deep learning is provided in [137].

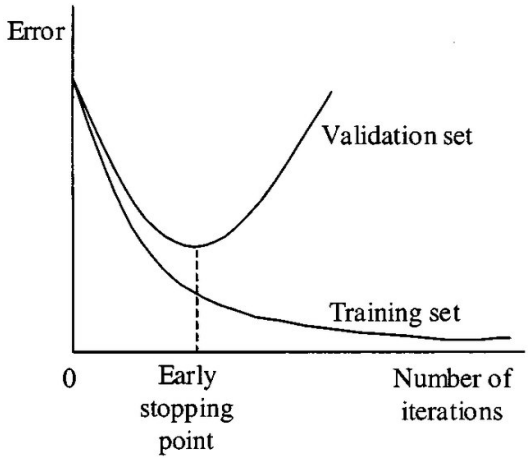

Figure 4.1: Early stopping based on cross-validation [141].

4.1.3.1 Early Stopping

Early stopping is a regularization technique used to stop the model's training before over-fitting occurs without compromising the model's accuracy. The most commonly used approach is to use a validation set strategy. In this approach, the change in training and validation errors is monitored as a function of the number of epochs. When the training error no longer changes with the increasing number of echoes and the validation error starts increasing (see Fig. 4.1), the model training is stopped. Beyond this point, the model will start to overfit.

4.1.3.2 Dropout

Dropout is a regularization technique that simulates the concurrent training of multiple sub-networks with shared weights [142]. During training, some fraction of the layers are temporarily removed along with all their incoming and outgoing connections during the forward pass, and weight updates are not applied to the neurons in the backward pass, as shown in Fig. 4.2. The fraction of neurons that are ignored is known as the dropout rate. This technique aids in reducing interdependent learning among neurons, thereby reducing model overfitting.

4.1.3.3 Data Augmentation

Data augmentation is a straightforward regularization method that artificially expands the amount of data by producing modified copies of the training

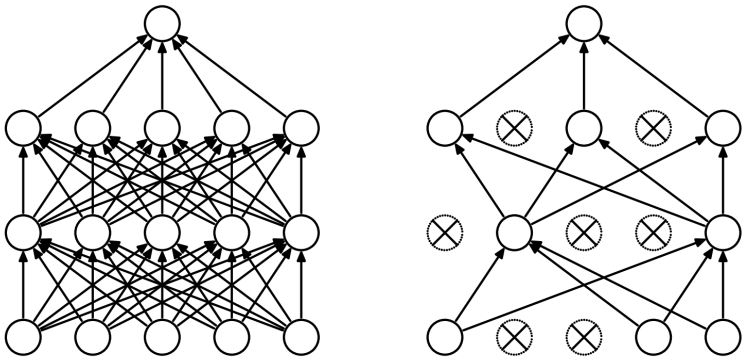

(a) Standard Neural Net (b) After applying dropout.

Figure 4.2: (a) A standard NN with 2 hidden layers, (b) After applying dropout to the original network [142].

examples [137]. Depending on the type of data, different transformation techniques can be applied to introduce slight variations in the original data [128]. This makes ML models more robust against variations in the test data. Data augmentation techniques can be grouped into two main categories: DL approaches and image manipulation methods [143]. The most commonly used methods in DL-based approaches are generative adversarial networks (GAN) and neural style transfer [144]. Image manipulation approaches include geometric transformations (such as Scaling, rotation, translation, and flipping) and color-space transformations (such as changing contrast and saturation, blurring, or adding a different color to an image), which are frequently used in computer vision [143].

4.1.3.4 Batch Normalization

The distribution of input data to the later layers continuously change as a result of updates to the parameters being learned during the training of the network. Such a change in the data distribution after each iteration causes early saturation of the nonlinear activation function. The batch-normalization (BN) is an adaptive normalization technique that is applied to the activations of each layer in the network to standardize the data to a layer for each mini-batch. This technique reduces the internal covariance shift between layers by controlling the mean and variance of the input distributions. In addition, it also stabilizes and speeds up the learning process [145]. For an m-dimensional input-batch $x = x_{i...m}$, the BN is performed as follows:

$$\widehat{x_i} = \frac{x_i - E[x_i]}{\sqrt{var[x_i]}}, \tag{4.5}$$

where $\hat{x_i}$ is the normalized input data, $E(x_i)$ and $var(x_i)$ are the mean the variance of the mini-batch samples. The normalized data is then scaled and shifted:

$$y_i = \alpha\widehat{x_i} + \beta, \tag{4.6}$$

here α and β represent the scaling and shifting parameters learned during the training of model.

4.2 Convolutional Neural Networks

Convolutional neural networks (CNNs) are multilayer trainable architectures that are built upon the same principle as MLPs. However, unlike MLPs, which take flattened vectors as input, the CNNs process data that have a grid-like pattern, such as an image [128]. As opposed to FC layers connecting all input and output activations, a CNN consists of a series of convolutional layers where the input data is filtered by small-sized learnable kernels that share weights across the image space [128, 137]. A CNN's architecture typically consists of a series of convolutional layers followed by pooling and fully connected layers.

5

Data Acquisition

The need for monitoring global aquatic systems as well as the rapid progress in oceanographic measurement capabilities have resulted in an enormous amount of ever-increasing remotely sensed data. The acquired data is becoming accessible with high temporal and spatial resolution. A large number of space-borne sensors have been continuously monitoring and collecting information on OC variables. As more data becomes available, it becomes more important to validate remotely sensed data and develop robust and novel OC models and algorithms. Lack of ground truth information on in-water constituents or radiometric data such as R_{rs}, can lead to uncertainties and misinterpretations of satellite-derived data. This is a major challenge for the OC community. Therefore, in-situ data collection is a prerequisite and provides unique opportunities to understand the optical signatures of WQ variables in different optical regimes.

This chapter describes the in-situ data collected and used in this study. The data is collected from i) the Barents Sea and ii) coastal, inland, and open waters around the globe.

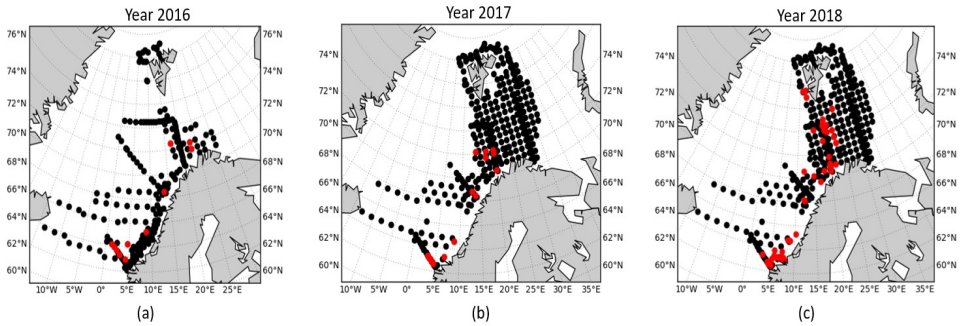

Figure 5.1: Geographic locations of Chl-a observations (black dots) and match-ups (red color) with satellite overpasses from year a) 2016, b) 2017 and c) 2018.

5.1 The Barents Sea

5.1.0.1 Chlorophyll-a

The Conductivity-Temperature-Depth (CTD) fluorescence of Chl-a was sampled between the years 2016 to 2018 as part of the Norwegian Institute of Marine Research's (IMR) Ecosystem Program. The Chl-a CTD data were gathered from a vast area in the Barents Sea and covered a wide range of various aquatic and environmental conditions. The measurements were made at various discrete depth intervals up to 100m in addition to surface measurements. The geographic locations of the in-situ data are presented in Fig. 5.1.

The Chl-a samples were collected at various CTD stations; 232 in 2016, 405 in 2017, and 424 in 2018, respectively. The Chl-a concentrations range from 0.014 to 10.81 mg/m^3. Although in-situ measurements were taken all year-round, this study only used data from April to October. The remaining months are dark or have extremely high solar zenith angles ($> 75°$) unsuitable for ocean color remote monitoring.

The Chl-a dataset represented in this chapter was used in Paper I.

5.1.0.2 Above water Radiometric data

The in-situ radiometric observations were compiled from multiple field campaigns in the year 2021 aboard the Norwegian ice-going research vessel Kronprins Haakon. The in-situ data were collected autonomously when the ship was at sea; however, to avoid higher solar zenith angles ($> 70°$), measurements from April to September were only used in this study. The spatial locations

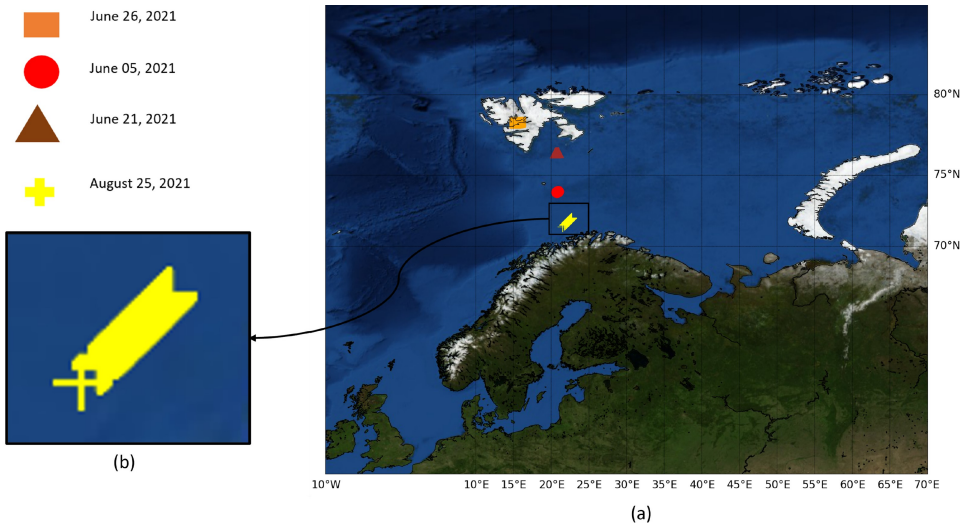

Figure 5.2: Geographic location of (a) the filtered in-situ radiometric data near-coincident with S-2A/B MSI overpasses, represented by different legends. b) closeup showing a matching transect [136]).

of near coincident Sentinel-2 MSI overpasses with in-situ data are shown in Fig. 5.2. The in-situ radiometric data were collected using TRIOS hyper-spectral radiometric sensors (see Fig. 5.3) in a spectral range from 320 to 950nm at ~3nm resolution and an integration time of 30 seconds. During each campaign over the Barents Sea, in addition to the predefined sampling stations where the Boat was stationary for field measurements, in-situ observations were collected along the intersect, as shown in Fig. 5.2 (b). However, for clarity, only Sentinel-2 cloud-free images with a time gap of ±3 hours with the in-situ observations for the period April-September in the year 2021, are shown in Fig. 5.2.

5.1.0.3 In-situ data processing

The radiometric quantity utilized in Paper II is the remote sensing reflectance, $R_{rs}=\rho_w/\pi$ which assumes an isotropic upwelling radiance field [146], and is defined as:

$$R_{rs}(\theta,\phi) = \frac{L_w(0^+)(\theta,\phi) - \rho_{sky} * L_{sky}(0^+)(\theta,\phi)}{E_d(0^+)} - \epsilon \tag{5.1}$$

where $L_w(0^+)$ (Watt m^{-2} nm^{-1} sr^{-1}), $L_{sky}(0^+)$ (Watt m^{-2} nm^{-1} sr^{-1}) and $E_d(0^+)$ (W m^{-2} nm^{-1}) are water leaving radiance, Sky radiance, and down-welling solar irradiance measured just above the water surface, respectively.

The terms (θ,ϕ) are the zenith and azimuth angles for the viewing direction, respectively. Here ρ_{sky} refers to the fraction of L_{sky} that is reflected specularly on the water surface and determined using the method developed in [147].

$$\rho_{sky} = 0.0256 + 0.00039W + 0.000034W^2 \quad \text{for } \frac{L_{sky}(0^+)}{E_d(0^+)} < 0.05 \tag{5.2}$$

$$\rho_{sky} = 0.0256 \quad \text{for } \frac{L_{sky}(0^+)}{E_d(0^+)} \geq 0.05 \tag{5.3}$$

where W represents the wind speed extracted from the ship log data. The L_{sky} and L_w make a zenith angle of 40^0 and 140^0 with the vertical [147]. The term ϵ corrects for the residual sky glint and is computed using the method developed in [148]. The developed algorithm in [148] assumes zero water-leaving reflectance at two suitably chosen near-infrared (NIR) wavelengths (720nm and 780nm). The choice of wavelength to estimate ϵ is made intuitively to cover distinct parts of the NIR spectrum that are not affected by the absorption of pure water, atmospheric oxygen or Color dissolved organic carbon (CDOM). ϵ is defined as:

$$\epsilon = \frac{\alpha_{1,2}\rho_w^m(780nm) - \rho_w^m(720nm)}{\alpha_{1,2} - 1} \tag{5.4}$$

where ρ_w ($R_{rs} \times \pi$) is the true water leaving reflectance and $\rho_w^m = \rho_w + \epsilon$ deonates the measured water leaving reflectance. The term $\alpha_{1,2} = 2.35$ is taken from the tabulated similarity spectrum [147]. This procedure minimizes the presence of features in R_{rs} that are affected by the air-water interface and removes spectra that do not converge on a solution. Thus, it is suitable to process large amounts of ship-based observations.

The processed in-situ R_{rs} spectra were then filtered to remove the remaining erroneous or suspicious observations using the criteria defined in [26,147] with minor modifications.

The in-situ radiometric dataset covers a broad range of environmental and aquatic conditions from open oceanic to coastal and inland waters. Some examples of in-situ R_{rs} are shown in Fig. 5.4.

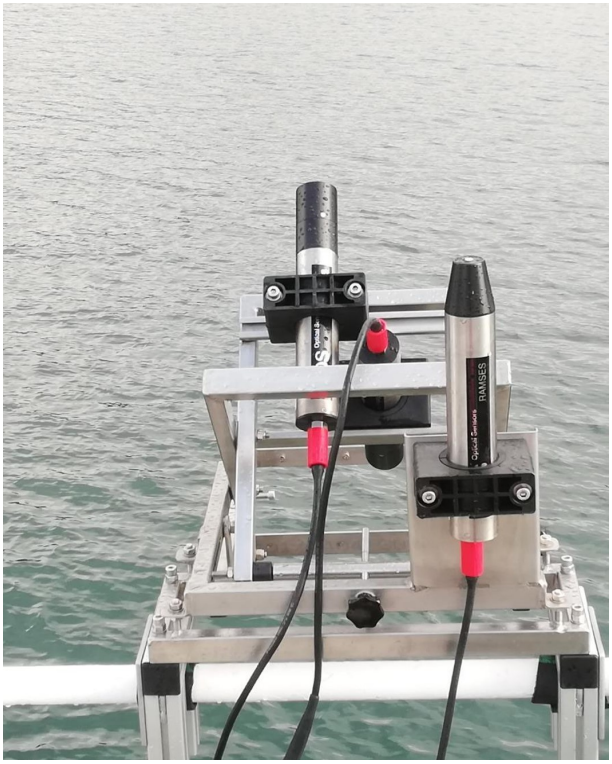

Figure 5.3: TRIOS Ramses Hyperspectral sensors mounted on Norwegian ice-going research vessel Kronprins Haakon.

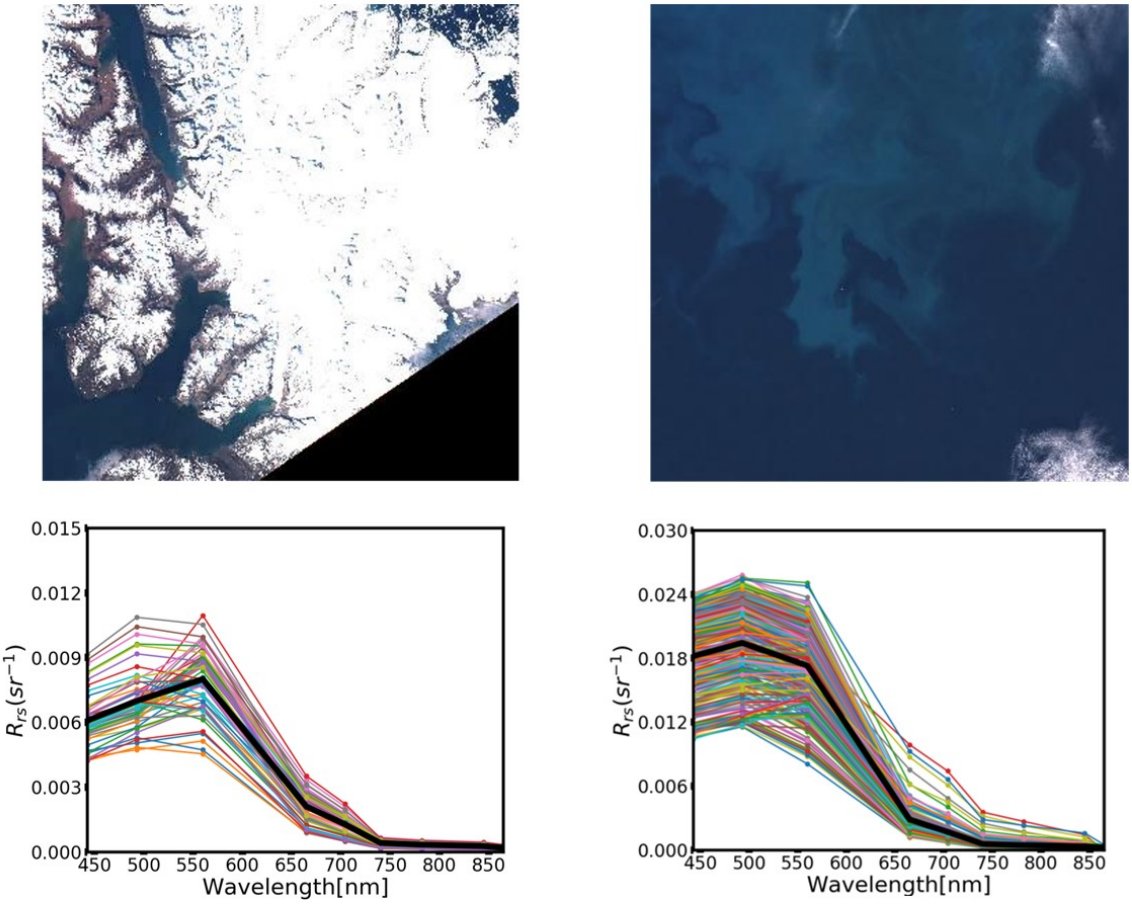

Figure 5.4: Examples of concurrent in-situ R_{rs} observations and Sentinel-2 A/B overpasses over the Barents Sea region, (a) inland waters, (b) Algal bloom in the open oceanic waters. Top-row: RGB satellite images, bottom-row: corresponding R_{rs} spectra.

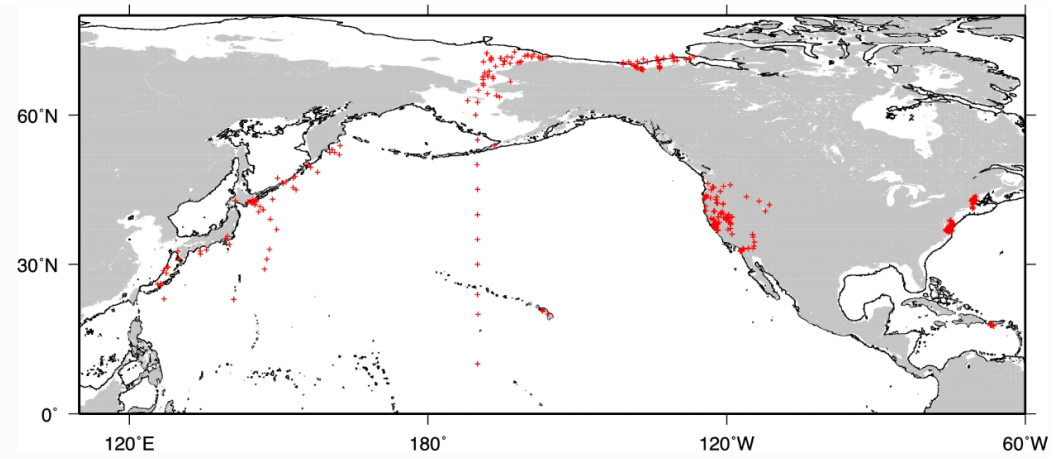

Figure 5.5: Sampling stations covering environments from oceanic to inland waters [14].

5.2 Global waters

5.2.1 Radiometric data

The in-situ radiometric observations were acquired from different aquatic systems, from freshwater to highly turbid and absorbing waters, as demonstrated by the frequency distributions illustrated in Fig. 5.6. The data were assembled in different field campaigns in the years 2011 to 2017 (see Fig. 5.5). The measurement protocols and quality control procedures are detailed in [149]. Briefly, the optical data were acquired systematically using a compact optical profiling system (C-OPS). In inland waters, a significant part of the optical data, including all profiles, was obtained using the Compact-Propulsion Option for Profiling Systems (C-PrOPS) accessory combined with the C-OPS hydrobaric buoyancy system [14,150]. During in-situ profiling, $L_u(z,\lambda)$ and $E_d(z,\lambda)$, where z and λ present depth and wavelength, were simultaneously measured at 19 wavebands between 320 and 875nm. More details are listed in [14].

The radiometric quantity considered in Paper III is ρ_w and is defined as:

$$\rho_w(z,\lambda) = \pi \times \frac{L_u(z,\lambda)}{E_d(z,\lambda)} = \pi \times R_{rs} \tag{5.5}$$

5.2.2 Chlorophyll-a and CDOM

In addition to the radiometric data, Chl-a (mg m^3) and the CDOM absorption coefficient ($a_{cdom}(\lambda)$, m^{-1}) were also obtained simultaneously. The Chl-a data

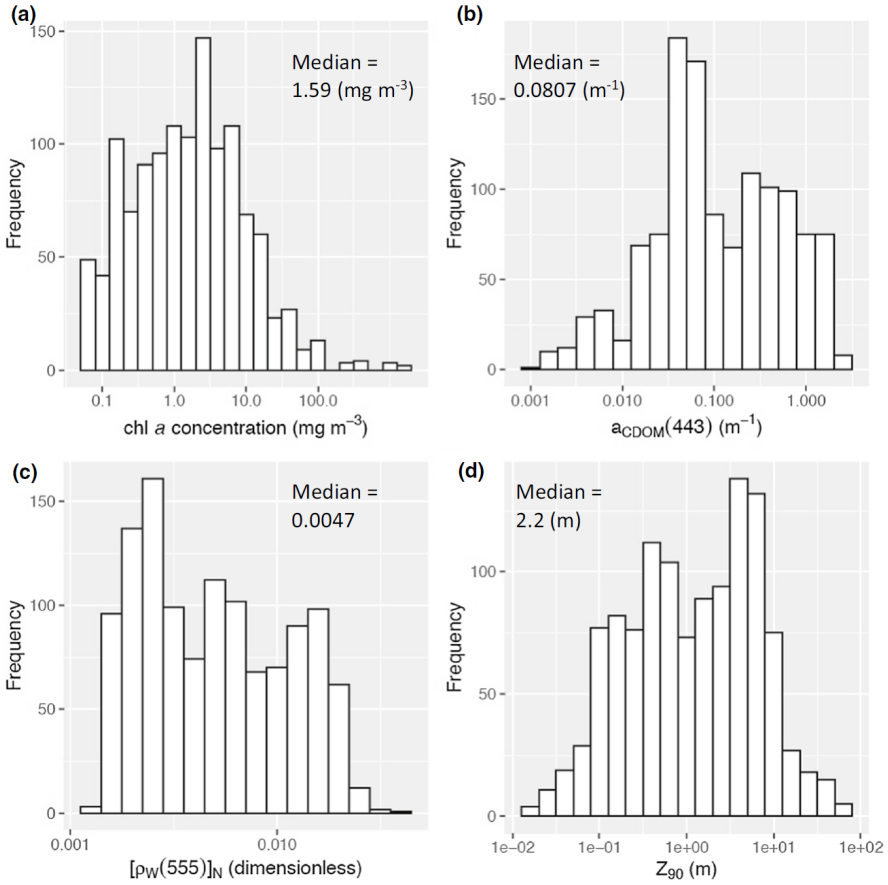

Figure 5.6: Frequency distribution of in-situ (a) concentration of Chl-a, (b) light absorption coefficient of CDOM at 443nm, (c) bidirectionally corrected water reflectance at 555nm, and (d) first optical depth (z_{90}). [14].

were obtained using the high-performance liquid chromatography (HPLC) method, following SeaHARRE protocols [151]. The $a_{cdom}(440)$ measurements were estimated with a spectrophotometer or UltraPathliquid waveguide [149]. The global dataset represented in this chapter was used in Paper III.

5.3 Remote Sensing Data Collection

In this thesis, S2-A/B MSI and L8 OLI imagery are used. Table. 5.1 provides details on their band characteristics.

Briefly, MSI Sentinel-2A and Sentinel-2B are identical polar-orbiting satellites, launched on June 23, 2015, and March 7, 2017, respectively, as part of the

Table 5.1: Sentinel-2A/B MSI and Landsat-8 OLI spectral bands and spatial characteristics [32, 131, 153–156].

	Landsat-8		**Sentinel-2A/B**	
Bands	**Wavelength [nm]**	**Spatial resolution [m]**	**Wavelength [nm]**	**Spatial resolution [m]**
Coastal aerosol	435–451	30	433–453	60
Blue	452–512	30	458–523	10
Green	525–600	30	543–578	10
Red	636–673	10	650–679	10
Red edge			698–793	20
			733–748	20
			773–793	20
NIR	851–879	30	785–900	10
			855–875	20
SWIR	1566–1651	30	1565–1655	20
SWIR	2107–2294	30	2100–2280	20

European Space Agency's (ESA) Copernicus program. The two twin satellites, with a 20.6° FOV, have a swath of 290km each and are placed in the same sun-synchronous orbit, 180° apart from each other [97]. The MSI onboard Sentinel-2A/2B provides a 10-day revisit time at the equator with 5 days each. It provides 13 spectral bands with a spatial resolution from 10 to 60m from visible to NIR to short wave near infrared (SWIR) as shown in Table. 5.1. Sentinel-2 MSI data are level-1C, calibrated TOA reflectance (ρ_t), and level-2C, surface reflectance (R_{rs}). The level-1C data are corrected for viewing geometry and are framed into tiles or granules sensing 109.8km by 109.8km of Earth's surface, geo-corrected in the Universal Transverse Mercator (UTM) projection [26, 152].

The Landsat-8 satellite carries the OLI and Thermal Infrared Sensor (TIRS) and was launched in February 2013 in a sun-synchronous polar orbit. Landsat-8 OLI has a 16-day repeat cycle and senses a 185-km-wide swath with a 15° FOV. As shown in Table. 5.1, OLI detects the Earth's surface at nine reflective wavelength bands. The data are provided in the Worldwide Reference System (WRS-2) path (ground track parallel) and row (latitude parallel) coordinate in 185×185km images [131].

Sentine-2 MSI data is used in Papers I, II and III while Landsat-8 OLI data is used in papers I and II. Note that both these sensors are operational.

6

Overview of Publications

6.1 Paper Summaries

6.1.1 Paper I

M. Asim, C. Brekke, A. Mahmood, T. Eltoft, and M. Reigstad, "**Improving chlorophyll-a estimation from sentinel-2 (MSI) in the barents sea using machine learning**," IEEE Journal of Selected Topics in Applied Earth Observations and Remote Sensing, 2021.

Several studies have been conducted on studying the primary production and Chl-a in the Barents Sea. Most of them are solely based on in-situ observations. Some studies have integrated in-situ data with satellite-based observations. However, the Chl-a retrieval methods are either based on semi-empirical or semi-analytical approaches and validated on either low spatial resolution satellite sensors or limited to validation on a few images. The main objective of Paper I was to develop a robust ML-based algorithm to accurately retrieve Chl-a from the Barents Sea using observations from a high-resolution satellite sensor, Sentinel-2 MSI.

To do this, we propose to match depth-integrated Chl-a concentrations with C2RCC retrieved R_{rs} products. To better tune the regression models, a new spatial window-based match-up dataset creation method was proposed to increase the number of match-ups. We demonstrated that the proposed match-up creation scheme has improved the performance of the Chl-a retrieval algorithms. In

addition to that, a NN based model was proposed, the OCN, that outperformed existing ML-based techniques including the Gaussian Process Regression (GPR), the regionally tuned empirical techniques, including the Ocean Color (OC_3) algorithm, and the spectral band ratios, as well as the globally trained C2RCC processing chain model C2RCC-nets.

It was manifested that the proposed spatial window and depth-integrated match-up creation techniques improved the performance of the proposed OCN and the other retrieval algorithms compared to the conventional match-up selection approach. Our results indicate that the proposed approach produces realistic Chl-a products in the study region by accurately capturing the fine details and abrupt changes in Chl-a distribution.

Author's contribution
The methodology was developed in collaboration with Camilla Brekke, Torbjorn Eltoft, and Arif Mahmood. I prepared the dataset, performed the analysis and implementations, and wrote the manuscript. Marit Reigstad contributed to data collection and reviewed the manuscript.

6.1.2 Paper II

M. Asim, A. Matsuoka, P. G. Ellingsen, C. Brekke, T. Eltoft, and K. Blix, "A new spectral harmonization algorithm for landsat-8 and sentinel-2 remote sensing reflectance products using machine learning: a case study for the barents sea (european arctic)," IEEE Transactions on Geoscience and Remote Sensing, 2022.

Water quality monitoring from space requires the acquisition of ocean color imagery with short time intervals (2-3 days) at a moderate spatial resolution ($< 60m$). OC remote sensing of the Barents Sea waters is associated with several challenges. During the summer months, it is frequently covered by clouds and experiences polar nights in the winter season, which limits the availability of cloud-free imagery. Furthermore, there are uncertainties associated with the existing AC methods due to the longer ray pathways caused by higher solar zenith angles and the proximity of sea ice.

In this study, an ML-based model was proposed to combine satellite observations from multi-satellite missions to increase the frequency of monitoring the dynamics of sensitive high-latitude aquatic systems. To maximize the availability of ocean color observations for regular monitoring of the Barents Sea waters, this study investigates the merging of MSI and OLI observations by addressing two key aspects: i) performance evaluation of standard AC algorithms to estimate realistic R_{rs} values over the study region. ii) an ML-based

band adjustment (BA) method is developed to reduce OLI-MSI derived R_{rs} products.

To achieve our objective, i.e., the spectral harmonization of OLI-MSI R_{rs} products, we first compared the R_{rs} retrieved via three state-of-the-art AC models, i.e., C2RCC, Acolite (DSF), and Polymer, against in-situ R_{rs} measurements. Our analysis demonstrates that Acolite is the top performer. Following that, the Acolite scheme was then selected to estimate R_{rs} products from near-simultaneous OLI and MSI images limiting the difference to <30 minutes. To reduce the differences in OLI-MSI R_{rs} products, a new ML-based spectral BA method was developed to spectrally adjust MSI radiometry to replicate the spectral bandpasses of OLI for the common bands on both sensors.

Results indicate that the proposed BA model can accurately reconstruct the spectral properties of OLI from MSI-derived R_{rs} products, demonstrating how MSI observations can be used to supplement OLI-derived Rrs products.

Author's contribution
The methodology was developed in collaboration with Katalin Blix, Atsushi Matsuoka, Torbjorn Eltoft, and Camilla Brekke. I prepared the dataset, performed the analysis and implementations, and wrote the manuscript. Pal Gunnar Ellingsen contributed to data collection and review of the article.

6.1.3 Paper III

M. Asim, A. Matsuoka, S. Hafeez, T. Eltoft, and K. Blix, "**Spectral harmonization of Landsat-8 and Sentinel-2 remote sensing reflectance products for mapping Chlorophyll-a in coastal, lakes and inland waters** (in submission).

The integration of data products from Sentinel-2 MSI and Landsat-8 OLI can improve the temporal resolution of time series, increase match-ups with in-situ observations, and provide a possibility to monitor the dynamics of sensitive aquatic systems.

In Paper II, a spectral harmonization method was developed to merge OLI and MSI images in terms of R_{rs} products for the Barents Sea region. In Paper III, we used the proposed method developed in Paper II to combine OLI-MSI R_rs products over global waters in order to increase the number of match-ups with in-situ observations and thus better tune the WQ retrieval algorithms. The main objective of Paper III was the accurate and consistent retrieval of Chl-a and CDOM from combined OLI and MSI images.

The proposed methodology combines the OLI and MSI data into a single dataset using a three-step approach: i) performance evaluation of AC methods against in-situ observations; ii) the top performing AC scheme was selected to estimate ρ_w products from near-simultaneous OLI and MSI images. The BA method developed in Paper II was then used to bandpass adjust MSI-ρ_w products (MSI$^*\rho_w$) to harmonize OLI-MSI images and iii) the weights and bias terms optimized during the conversion of MSI-derived ρ_w to that of OLI-derived ρ_w are applied to the MSI-ρ_w products. The OCN model was then tuned to retrieve Chl-a and CDOM from the combined OLI and MSI* dataset.

Our analysis demonstrates that OC-SMART showed consistent performance over different water types with MAPD <30% across the visible bands. The OLI-MSI ρ_w products retrieved from OC-SMART are estimated to range from 13 to 3% in the common visible bands. After applying the proposed BA model, the spectral difference in their respective ρ_w products were found in the range from 3 to <8%. Our results indicate that, using combined OLI and MSI* data, considerable improvements in Chl-a and CDOM estimation were observed in all methods compared to using OLI match-ups alone.

Author's contribution
The methodology was developed in collaboration with Katalin Blix, Sidrah Hafeez, Atsushi Matsuoka, and Torbjorn Eltoft. I processed the in-situ data, performed the analysis and implementations, and wrote the manuscript.

6.2 Other Publications and Contributions

1. **M. Asim**, S. Hafeez, A. Matsuoka, M. S. Wong, S. Abbas, T. Eltoft, K. Blix, "Atmospheric Correction of Landsat 8 Operational Land Imager (OLI), Sentinel-2 MultiSpectral Imager (MSI) over Asian, European and U.S Inland and Coastal waters", submitted to IGARRS, 2023.

2. S. Hafeez, **M. Asim**, M. S. Wong, and S. Abbas, "Atmospheric Correction of the Landsat 8 Operational Land Imager (OLI), Sentinel-2 MultiSpectral Imager (MSI) and Sen-tinel-3 Ocean and Land Colour Instrument (OLCI) over Low to High Turbid Coastal Waters of Hong Kong," in submission to Frontiers in Remote Sensing.

3. S. Hafeez, M. S. Wong, S. Abbas, and **M. Asim**, "Evaluating landsat-8 and sentinel-2 data consistency for high spatiotemporal inland and coastal water quality monitoring," Remote Sensing, vol. 14, no. 13, p. 3155, 2022.

4. **M. Asim**, C. Brekke, T. Eltoft and K. Blix, "Preliminary analysis of com-

bined Sentinel-2 and Landsat-8 remote sensing reflectance products for improved monitoring of Chlorophyll-a over the Barents Sea", Ocean from Space, Venice, 2022 (poster presentation).

5. **M. Asim**, K. Blix, P. Ellingsen, C. Brekke, T. Eltoft, "Evaluation of spectral consistency between Landsat-8 (OLI) and Sentinel-2 (MSI) remote sensing reflectance product over the Barents Sea", 2021 Center for Integrated Remote Sensing and Forecasting for Operations (CIRFA) annual conference, Sommarøy, 2021 (poster presentation)

6. **M. Asim**, C. Brekke, T. Eltoft and K. Blix, "Optical Remote Sensing and Machine Learning for Water Quality Parameter Retrieval in the Barents Sea", 2021 Frontiers, Tromsø, 2021 (poster presentation).

7. **M. Asim**, C. Brekke, A. Mahmood, T. Eltoft, and M. Reigstad, "Ocean color net (ocn) for the barents sea," in IGARSS 2020-2020 IEEE International Geoscience and Remote Sensing Symposium. IEEE, 2020, pp. 5881–5884.

8. **M. Asim**, P. Ellingsen, C. Brekke, T. Eltoft, "Assessment of Atmospheric Correction Algorithms for Sentinel-2 Over Balsfjord", 2020 Center for Integrated Remote Sensing and Forecasting for Operations (CIRFA) annual conference, Sommarøy, 2020 (poster presentation)

/7

Paper I: Improving Chlorophyll-A Estimation From Sentinel-2 (MSI) in the Barents Sea Using Machine Learning

Improving Chlorophyll-A Estimation From Sentinel-2 (MSI) in the Barents Sea Using Machine Learning

Muhammad Asim, Camilla Brekke, *Member, IEEE*, Arif Mahmood, Torbjørn Eltoft, *Member, IEEE*, and Marit Reigstad

***Abstract*—This article addresses methodologies for remote sensing of ocean Chlorophyll-a (Chl-a), with emphasis on the Barents Sea. We aim at improving the monitoring capacity by integrating *in situ* Chl-a observations and optical remote sensing to locally train machine learning (ML) models. For this purpose, *in situ* measurements of Chl-a ranging from 0.014–10.81 mg/m^3, collected for the years 2016–2018, were used to train and validate models. To accurately estimate Chl-a, we propose to use additional information on pigment content within the productive column by matching the depth-integrated Chl-a concentrations with the satellite data. Using the optical images captured by the multispectral imager instrument on Sentinel-2 and the *in situ* measurements, a new spatial window-based match-up dataset creation method is proposed to increase the number of match-ups and hence improve the training of the ML models. The match-ups are then filtered to eliminate erroneous samples based on the spectral distribution of the remotely sensed reflectance. In addition, we design and implement a neural network model dubbed as the ocean color net (OCN), that has performed better than existing ML-based techniques, including the Gaussian process Regression (GPR), regionally tuned empirical techniques, including the ocean color (OC3) algorithm and the spectral band ratios, as well as the globally trained Case-2 regional/coast colour (C2RCC) processing chain model C2RCC-networks. The proposed OCN model achieved reduced mean absolute error compared to the GPR by 5.2%, C2RCC by 51.7%, OC3 by 22.6%, and spectral band ratios by 29%. Moreover, the proposed spatial window and depth-integrated match-up creation techniques improved the performance of the proposed OCN by 57%, GPR by 41.9%, OC3 by 5.3%, and spectral band ratio method by 24% in terms of RMSE compared to the conventional match-up selection approach.**

***Index Terms*—Barents sea, Chlorophyll-a (Chl-a) monitoring, ocean color (OC).**

Manuscript received October 8, 2020; revised January 16, 2021 and March 9, 2021; accepted April 7, 2021. Date of publication April 22, 2021; date of current version June 8, 2021. The work was supported in part by the Nansen Legacy Project, RCN under Project 276730 and in part by "Centre for Integrated Remote Sensing and Forecasting for Arctic Operations" (CIRFA), RCN under Project 237906. *(Corresponding author: Muhammad Asim.)*

Muhammad Asim, Camilla Brekke, and Torbjørn Eltoft are with the Department of Physics and Technology UiT, Arctic University of Norway (UiT), 9019 Tromsø, Norway (e-mail: muhammad.asim@uit.no; camilla.brekke@uit.no; torbjorn.eltoft@uit.no).

Arif Mahmood is with the Department of Computer Science, Information Technology University of the Punjab, Lahore 5400, Pakistan (e-mail: arif.mahmood@itu.edu.pk).

Marit Reigstad is with the Department of Arctic and Marine Biology UiT, Arctic University of Norway, 9019 Tromsø, Norway (e-mail: marit.reigstad@uit.no).

Digital Object Identifier 10.1109/JSTARS.2021.3074975

I. Introduction

THE Barents sea is a large Arctic shelf that covers about 10% of the Arctic Ocean [1]. The northern part of the Barents Sea is seasonally ice-covered while the southern part is sea-ice-free due to the inflow of salty, warm, and nutrient-rich waters from the Atlantic Ocean through the Nordic Seas [2]. Almost 40% of the total Arctic primary production occurs in the Barents Sea and hosts Norway's richest commercial fisheries [3]. However, the Barents Sea is experiencing significant changes due to the result of global warming. The increased inflow of Atlantic water has caused up to a 50% reduction in sea-ice covered region in the last decade [4]. Due to sea-ice loss and weaker stratification of the water column, the sea under the melting ice in the Barents Sea is exposed to prolonged exposure of sunlight during summer and fall, which has increased the production and seasonal growth of phytoplankton [5], [6]. The effect of altered physical conditions in different seasons on the primary productivity is therefore crucial to investigate the ecosystem of the lately changing Barents Sea. It is within this context, the current study is aimed at developing new methods that can more accurately track phytoplankton biomass variability in the Barents Sea.

Phytoplankton are recognized as valuable indicators of marine ecosystem health, quality of water, and are sensitive to climate changes [7]. As a light-harvesting pigment in phytoplankton, Chlorophyll-a (Chl-a) is regarded as a proxy for biomass in the water column [8]. Phytoplankton form the bases of aquatic food webs and can grow rapidly in a short period depending on the availability of nutrients, sunlight, nitrogen, or phosphorus concentration [6], [9]. An excessive concentration of phytoplankton harms the fishery, local economy, marine animals, and public health [10], therefore, making it critical to carefully evaluate the exact concentration of Chl-a.

Several studies have been conducted on modeling the net primary production and Chl-a content in the Barents Sea, though, many are solely based on *in situ* measurements [6], [11]–[15]. Several methods integrating *in situ* with satellite-based observations have also been proposed [1], [16]–[23]. These studies on Chl-a retrieval are either based on empirical or semianalytical approaches and confined to relatively small spatial and temporal scales. Some of the existing methods are applied to in situ remote sensing reflectance (R_{rs}) data and validated on either

low spatial resolution satellite sensors or limited to validation on a few images [23]. For example, Le *et al.* [1] used a 3-D sea-ice plankton ecosystem model to study primary production in the northern Barents Sea for only summer months. Engelsen *et al.* proposed an empirical method to estimate Chl-a content across the water columns using sea-viewing wide field-of-view sensor (SeaWiFS) data confined to the early bloom season [17]. Kogeler *et al.* used an empirical model based on blue/green ratio to estimate Chl-a using only 35 images acquired from CZCS sensor [18]. Dalpadado *et al.* divided the Barents Sea region into 15 polygons and computed correlation between the mean of *in situ* Chl-a samples and all valid Chl-a pixels from SeaWiFS and MODIS Aqua, within a polygon [6]. More recently, a bio-optical model was developed from a set of *in situ* observations of Chl-a and inherit optical properties (IOP's) collected only in the bloom season. Due to cloud cover and longer time-gaps, the estimated R_{rs} spectra derived from IOP's were validated with an eight-day average MODIS-A observation [23]. Thus, most of the existing methods are not validated independently on high-resolution satellite data such as Sentinel-2 multi spectral instrument (MSI) covering a wide area of Barents Sea. Considering the importance of a long-term monitoring of water quality, the need to develop a reliable algorithm to accurately estimate Chl-a in the transitional Barents Sea is needed.

Recently, with the increasing popularity of ML in the field of remote sensing, several ML-based methods have been proven effective in retrieving Chl-a from water bodies. However, for the Barents Sea, to the best of our knowledge, no thorough study has been reported on Chl-a estimation using ML techniques integrated with remotely sensing data.

The most widely explored ML methods include artificial neural networks (ANNs) [24], support vector regression (SVR) [25], relevance vector regression (RVR) [26], random forests (RF) [27], Gaussian process regression (GPR) [28], [29], and mixture density networks (MDN) [8]. The ANNs due to their ability to learn highly, nonlinear relationships have attracted many researchers [24], [30]–[32]. However, in most of these existing studies, built-in software ANN modules have been utilized; therefore, the architecture of ANNs has not been well explored despite their potential effectiveness in estimating nonlinear functions. The current study explores the architecture and ability of MLP-based deep ANNs in detail to accurately map water leaving R_{rs} to Chl-a concentrations for the Barents Sea, which is a novel application area.

In most of the existing studies [8], [24], [30], researchers have associated surface or near-surface Chl-a concentration ($[\text{Chl-a}]_{\text{surf}}$) at some discrete depths with the water leaving R_{rs}. This approach restricts Chl-a estimation to the upper layer of the water column while the solar radiation is not restricted only to the near-surface. Depending on the IOP's of the water body, scattering and absorption, radiation can penetrate deeper, and a satellite will capture the integrated effect across the water column. Moreover, in the biogeochemical applications such as primary production estimation or investigating the vertical distribution of algal species, the near-surface Chl-a content estimated by ocean color (OC) sensors is insufficient to track the algal biomass in the entire depth range, where algae can live and grow [33]. Therefore, in the current work, we propose to integrate Chl-a across water columns depending on the light penetration depth (Z_{pd}) in order to accurately estimate the primary production.

In some of the previous studies, a median or mean R_{rs} value over a spatial window has been associated with the *in situ* Chl-a samples [34]–[36]. Warren *et al.* resampled all the spectral bands to a common spatial resolution and used the central pixel in the window [37]. In contrast to the existing approaches, we propose to use all valid pixels in a spatial window without taking mean or median of the R_{rs} values. Our approach increases the match-up dataset size and improves the overall performance of the proposed model. Besides, it also improves the performance of existing empirical and ML methods in estimating Chl-a in open ocean waters such as the Barents Sea. Matching each *in situ* measurement of Chl-a to all valid pixels in a window results in estimating multiple values of Chl-a. The median over these estimated values is then computed, which is a more robust estimate of Chl-a. In addition, we also propose a filtering criterion based on the spectral distribution of R_{rs}. After applying the recommended atmospheric correction (AC) quality flags [37], [38], the match-ups are further processed to remove the nonphysical and unrealistic measurements in-terms of spectral distribution and amplitude that arise due to the time-gap or uncertainty in the AC algorithm. The systematic system diagram illustrating the main components of the proposed methodology is given in Fig. 1. The major contributions of the present study are as follows.

1) In the current work, we analyze various techniques for match-up selection and Chl-a retrieval from the Barents sea.
2) To account for the uncertainty in the remotely sensed data, we also propose a match-up dataset filtering method based on the concentration of Chl-a and spectral distribution of R_{rs}.
3) We propose to retrieve depth-integrated Chl-a to track the phytoplankton bloom appearing down the water column for a more accurate estimation of the biomass.
4) By combining the proposed data augmentation technique with the depth-integrated-average Chl-a, we formulate a novel Chl-a estimation framework that enhances the performance of the proposed as well as compared methods.
5) To improve the Chl-a estimation accuracy in the sub-Arctic waters, we propose a neural network-based algorithm dubbed as OCN.
6) The proposed match-up dataset creation, data augmentation, and depth integration techniques have improved the Chl-a retrieval performance of all the methods considered in this study. The proposed OCN model has outperformed all the compared methods.

The remaining of the article is organized as follows. Section II presents related work, whereas Section III is devoted to material and satellite data acquisition. The match-up selection and ML methodologies are presented in Section IV and V, and the experimental results are discussed in Section VI. Finally, Section VII concludes the article.

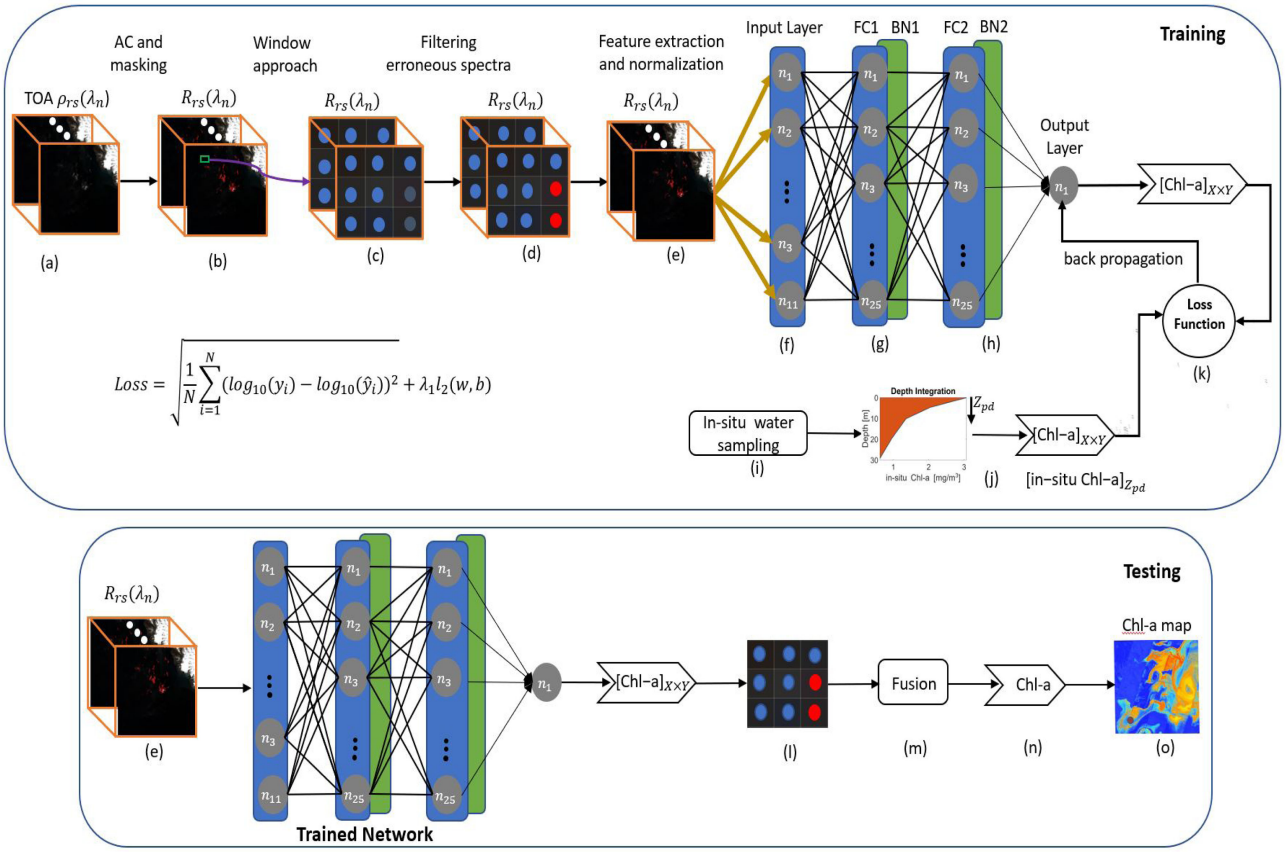

Fig. 1. Proposed OCN framework for estimating Chl-a. (a) Input top-of-atmospheric reflectance (ρ_{rs}) (Section III-B). (b) (ρ_{rs}) is corrected for atmospheric effects to extract surface R_{rs} (Section IV-A). (c) Window over R_{rs} pixels centered around the *in situ* location (Section IV-C). (d) Filtering block to get valid R_{rs} pixels (Section IV-B). (e) Features extraction block over the valid R_{rs} pixels (Section V-A). (f) Input layer of the FC neural network. (g) First fully connected block consisting of an FC and batch normalization (BN) layers (Section V-A2). (h) Second FC block with FC and BN layers. (i) *In situ* Chl-a sampling (Section III-A). (j) *In situ* depth integration block (Section IV-D). (k) Network loss computation (3). (l) Output of the network over the window on the test dataset. (m) Information fusion block (Section IV-C). (n) Output of the proposed framework, Chl-a. (o) Chl-a maps.

II. Related Work

OC remote sensing is a practical and powerful tool in the monitoring of aquatic environments and providing estimates of near surface concentration of water quality parameters such as Chl-a in open ocean [39], [40], coastal waters [41], as well as inland waters [42]. Existing Chl-a retrieval algorithms may be divided into two categories, analytical approaches and empirical methods [7]. Most analytic approaches consist of two steps, derivation of the IOPs that determine the color of water, followed by estimation of Chl-a content. In the empirical approaches, Chl-a concentration is estimated directly from R_{rs}, also known as the inversion approach. The empirical methods rely on the estimates of phytoplankton absorption peaks within the blue and red portions of the spectrum [43], [44].

Chl-a in the open ocean waters has been estimated using the ratio of blue to green bands, which assumes that the shape and magnitude of R_{rs} spectrum between blue and green bands is primarily driven by the concentration of Chl-a with minimum effect from other organic and inorganic substances [7]. Previous studies have shown that the blue-to-green ratio has a strong correlation with Chl-a in clear waters. The polynomial coefficients in the ocean color (OC) algorithm [45], where the blue-to-green ratio of $R_{rs}(\lambda)$ statistically relates to Chl-a through a polynomial expression, have been tuned according to the spectral configuration of various satellite sensors. More recently, 65 polynomial expressions were developed for 25 satellites utilizing 2720 pairs of coincident Chl-a and corresponding R_{rs} [45]. The R_{rs} spectrum in coastal and inland waters is affected by the presence of other constituents, which often leads to an overestimation of Chl-a [8], [46]. Therefore, several other empirical formulations have also been proposed, including the red-edge ratio methods [47]–[49], the line height (LH) method [50], hybrid methods [51], and ML-based methods [24], [30]–[32].

Level-2 products from Sentinel-2 MSI, ocean and land color imager (OCLI) onboard Sentinel-3, and AC processors such as Acolite, C2RCC, and Seadas estimate Chl-a using band ratios, semianalytical methods, or ML methods such as NNs, which are trained globally on a large amount of simulated data. Efficient retrieval of Chl-a across all water types using a single method is quite challenging. Smith *et al.* suggested that an algorithm should be locally trained to learn the nonlinearity of the functional dependence between the reflected water leaving radiance and Chl-a concentrations [52]. More recently, ML-based

TABLE I
DESCRIPTIVE STATISTICS OF *IN SITU* CHL-A CONCENTRATIONS AT VARYING DEPTHS DURING YEARS 2016–2018 IN THE BARENTS SEA

Months	**0 ≤ Depth < 0.5m**			**0.5 m ≤ Depth < 12.5m**			**12.5m ≤ Depth ≤ 25m**		
	min	max	mean ± std	min	max	mean ± std	min	max	mean ± std
Year 2016									
April	0.191	6.699	1.587 ± 1.562	0.151	7.465	1.836 ± 1.806	0.142	6.912	1.676 ± 1.515
May	0.102	3.261	0.609 ± 0.52	0.118	3.647	0.735 ± 0.686	0.175	4.795	0.673 ± 0.717
July	0.360	0.990	0.602 ± 0.249	0.308	1.038	0.646 ± 0.261	0.501	1.519	1.011 ± 0.374
September	0.191	2.221	1.101 ± 0.463	0.182	2.403	0.968 ± 0.486	0.263	2.32	0.909 ± 0.443
October	0.723	2.887	1.438 ± 0.859	0.184	1.116	0.758 ± 0.359	0.408	0.59	0.499 ± 0.091
Over All	0.102	6.699	1.099 ± 1.174	0.118	7.465	1.26 ± 1.335	0.142	6.912	1.359 ± 1.328
Year 2017									
April	0.886	2.774	1.492 ± 0.722	0.737	2.959	1.649 ± 0.736	0.568	2.816	1.416 ± 0.792
May	0.102	6.641	2.008 ± 1.625	0.119	6.622	2.047 ± 1.48	0.215	5.400	1.286 ± 1.261
June	0.190	4.248	1.015 ± 0.808	0.182	5.053	1.117 ± 0.829	0.163	3.941	1.183 ± 0.845
August	0.373	3.708	1.536 ± 0.718	0.227	3.855	1.343 ± 0.767	0.204	8.962	1.541 ± 1.121
September	0.052	5.428	0.989 ± 0.863	0.071	4.165	1.141 ± 0.654	0.046	3.368	1.051 ± 0.597
October	0.604	2.327	1.202 ± 0.408	0.536	2.389	1.199 ± 0.427	0.542	2.372	1.127 ± 0.412
Over All	0.052	6.641	1.346 ± 1.082	0.071	6.622	1.293 ± 0.873	0.046	8.962	1.215 ± 0.852
Year 2018									
April	0.288	9.601	3.311 ± 2.006	0.255	10.81	3.793 ± 2.374	0.174	9.498	2.759 ± 1.999
May	0.234	4.497	1.306 ± 0.801	0.285	5.006	1.513 ± 0.994	0.243	4.849	1.439 ± 1.147
June	0.381	2.988	1.624 ± 0.642	0.566	3.142	1.678 ± 0.586	0.260	2.798	1.338 ± 0.667
August	0.253	3.623	1.192 ± 0.767	0.262	3.695	1.23 ± 0.782	0.391	2.505	1.128 ± 0.656
September	0.014	4.350	0.801 ± 0.513	0.141	4.589	0.833 ± 0.516	0.152	4.656	0.781 ± 0.519
October	0.318	1.248	0.722 ± 0.281	0.313	1.286	0.723 ± 0.282	0.268	1.168	0.669 ± 0.244
Over All	0.014	9.601	1.404 ± 1.247	0.141	10.810	1.569 ± 1.513	0.152	9.498	1.318 ± 1.268

The *in situ* data are collected as part of the ecosystem monitoring program, IMR

methods trained locally on the area under observation have attracted researchers due to the improved performance [27], [29], [32], [53].

Most of the abovementioned methods associate *in situ* measurements with satellite observation of 3×3 [34], [35], [54] or 5×5 pixels window [36], centered around the *in situ* location. A mean or median of cloud-free and valid pixels is computed to extract a single value of R_{rs} for each *in situ* sample. Pu *et al.* utilized convolutional neural network (CNNs) to model the relationship between Landsat-8 images and *in situ* water-quality levels by considering a spatial window of 1 km^2 (7×7 pixels) at each monitoring station [55]. Pyo *et al.* [56] also developed a CNN-based regression model to estimate Chl-a concentrations using hyperspectral images acquired from an airborne sensor. They used a window of 8 × 8 pixels for extracting the nonlinear spatial features of the algal pigment.

These regression models based on CNN require a large amount of cloud-free dataset with minimum time-difference between the *in situ* and remote sensing data. To address this issue Pyo *et al.* [56] used airborne hyperspectral imagery to train the CNN, which is much more costly than using freely available satellite image data. Moreover, these approaches are based on a fixed window size, which may include invalid pixels depending on the observation conditions. In contrast, in the current work, we propose an NN-based on multi layer perceptron (MLP), with the flexibility to remove invalid pixels from each window, that can work efficiently for smaller datasets.

III. DATASET ACQUISITION

In this section, we discuss the collection of *in situ* Chl-a data and the overlapping satellite observations.

A. In Situ *Observations*

The Barents Sea is one of the most productive oceanic areas in the world, and it has an average depth of 230 m with a total area of 1.5 million km^2 [6]. A sampling of conductivity-temperature-depth (CTD) fluorescence of Chl-a were carried out in the years 2016–2018, as part of the Ecosystem Program of the Institute of Marine Research (IMR), Norway. The Chl-a CTD data were collected from a vast region in the Barents Sea, covering various oceanographic conditions. In addition to the samples from the surface, Chl-a measurements were also collected at different discrete depth intervals up to 100 m. Data were collected from various CTD stations; 232 in year 2006, 405 in year 2017, and 424 in the year 2018, respectively. The Chl-a concentration varies from 0.014 to 10.81 mg/m^3. The *in situ* measurements were collected throughout the year; however, measurements from April to October are used in this study. The remaining months remain dark with insufficient and extremely low solar elevations, making remote sensing unsuitable for OC monitoring. The monthly and yearly variation in Chl-a content across water columns is shown in Table I. The spatial locations of *in situ* data are shown in Fig. 2(a)–(c).

B. Satellite Image Data Acquisition

Sentinel 2 A/2B on-board MSI from the European Space Agency (ESA) with a swath of 290 km each, are in the same orbit and 180° apart from each other. The revisit time of Sentinel-2 A/2B is 10 days (of each satellite) at the equator, meaning that the twin satellites revisit the same area every five days, with a wide field of view, covering land and coastal areas [57], [58]. In order to reacquire a cloud-free image of a specific area, it may take significantly more time, depending on the weather conditions. Note that a cloud cover is much more persistent in

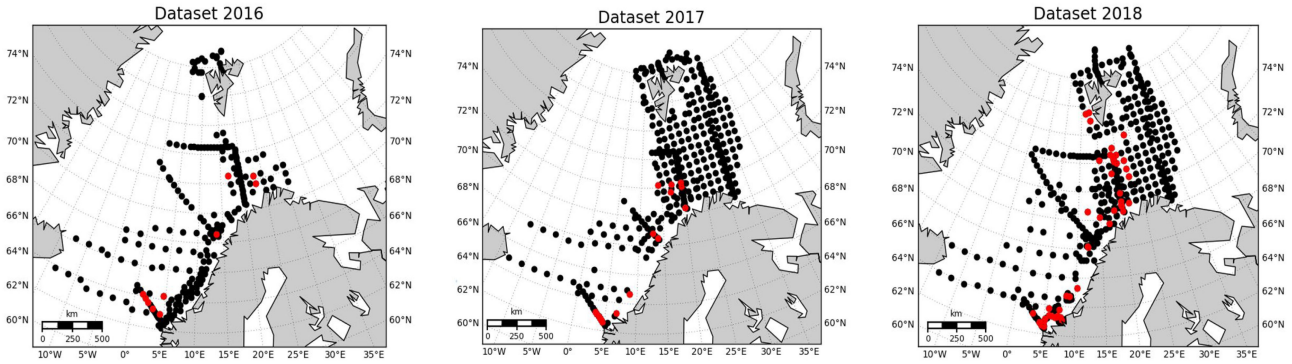

Fig. 2. Study region and locations of *in situ* observations of Chl-a (black dots) and match-ups (red color) from year (a) 2016, (b) 2017, and (c) 2018.

TABLE II
SENTINEL-2 SPECTRAL BANDS WITH SNR AT THE REFERENCE RADIANCE L_REF

Bands	Central Wavelength [nm]	Bandwith [nm]	Spatial Resolution [m]	L_{ref} [W m^{-2} sr^{-1} μm^{-1}]	SNR at L_{ref}
1	443	21	60	129	129
2	493	66	10	128	152
3	560	36	10	128	168
4	665	31	10	108	142
5	704	16	20	74.5	117
6	740	15	20	68	89
7	783	20	20	67	105
8	832	106	10	103	174
8a	864	20	20	52.5	72
9	945	20	60	9	114
10	1375	30	60	6	50
11	1610	92	20	4	100
12	2190	180	20	1.5	100

the high-Latitude areas such as the Barents Sea. The Sentinel-2 A/2B mission provides the reflected solar spectral radiances in 13 spectral bands in the visible, infrared, and short-wave infrared part of the electromagnetic spectrum. As shown in Table II, among the 13 spectral bands, the four bands centered at 493 nm (blue), 560 nm (green), 665 nm (red), and 842 nm (NIR) have a spatial resolution of 10 m. These four bands are suitable for the retrieval of biogeochemical products and IOP's of the water column. The six bands centered at 705, 740, 783, 864 nm, [covering the visible and near infrared (VNIR) region] 1610, and 2190 nm [covering short wave infra-red (SWIR) region] have a spatial resolution of 20 m. These six bands are suitable for applications such as snow, ice, and cloud masking. The remaining three bands centered at 443, 945, and 1375 nm, have a spatial resolution of 60 m and suitable for AC and cloud screening. These bands are also used for aerosols retrieval, water vapor correction, and cirrus detection [59].

Sentinel-2 acquire spectral observations from $-56°$ to $84°$ latitude [59], therefore, suitable for OC monitoring in the Barents Sea. Sentinel-2 A/2B Level1-C (L_1 C) data, colocated in space and with a time gap within ± 1 d of the *in situ* observations for the period 2016–2018 (April–October) having a cloud coverage of $\leq 30\%$, is acquired from.[1] The L_1 C product provides geocoded top-of-atmospheric (TOA) reflectance, with associated cloud, land/water mask, and quality flags. To ensure cloud-free pixels in a window of 3×3 pixels, centered at the *in situ* observation location, the Sentinel-2 L_1 C built-in cloud mask was applied in the sentinel application platform (SNAP) v6.0 processing toolbox, prior to applying AC. The cloud mask enables to identify both cirrus and dense clouds. The dense clouds have a high reflectance in the blue wavelength (493 nm). If the reflectance in the blue band is greater than a threshold, that pixel is identified as covered by dense clouds, also known as opaque clouds [60]. Cirrus clouds are thin and semitransparent and usually formed approximately at 6–7-km above the Earth's surface. The high-atmospheric absorption in band-10 (1375 nm) makes the detection of cirrus clouds possible.

A time window of ± 1 d between *in situ* and satellite measurements was used to find match-ups. For comparison, Warren *et al.* [37] allowed a window of $\pm$ 1 d for inland waters, Kuhn *et al.* [61] allowed a time window of $\leq \pm 1$ day for three different rivers while Le *et al.* [49] and Pan *et al.* [62] allowed a window of ± 24 h and ± 8–32 h, respectively, for coastal waters to obtain a sufficient number of valid match-up pairs for algorithmic validation. More recently, a larger time-window of $\pm$ 2 days was used by Liu *et al.* [46] for 36 different water bodies, including coastal waters, inland lakes, reservoirs, and rivers in the United States and China. If the pixels of interest in the acquired scene corresponding to the *in situ* location are identified as invalid or defective, then the next scene within the specified time window is analyzed. If none of these masks or quality flags are true, the pixel is considered water and processed through the AC

[1]Online. [Available]: https://scihub.copernicus.eu/dhus

algorithm. If the pixels of interest are found cloudy or defective in all available scenes, then that *in situ* observation is discarded.

IV. Matchup Selection Methodologies

In this section we present different proposed match-up selection methodologies. Before using the proposed matchup selection, AC is applied to convert the TOA signal to above water R_{rs}.

A. Atmospheric Correction (AC) Algorithm

AC is a crucial step in OC monitoring algorithms. The retrieved signal by satellite sensors contain $< 10\%$ of water leaving radiances, the remaining is the contribution from atmosphere [63]. The water leaving radiance is then converted to R_{rs}, the ratio of water-leaving radiance to the total downwelling irradiance measured just above the water surface, which carries information about the water-column and can be used to derive OC products such as Chl-a concentration [54].

Prior to applying AC, Sentinel-2 L-1 C data were resampled to a spatial resolution of 60m [37]. This spatial resolution is selected to improve the signal-to-noise ratio and enable the application of AC. The resampled TOA reflectances R_{rs} were then atmospherically corrected into the water-leaving R_{rs} (sr $^{-1}$) using the C2RCC AC processor. The choice of C2RCC is motivated due to its good performances in [37] and [38]. The C2RCC processor is based on the ANN method, where the ANNs are trained on a large database of simulated water-leaving reflectances and related TOA radiances. The trained ANN is then used to perform the inversion of TOA radiances to water-leaving radiance. Moreover, it also generates Chl-a maps and estimates the IOP's of the water body. The C2RCC is a modified form of previous Case2Regional and CoastColour AC algorithms. In this study, compared to the other AC processors such as Acolite and Sen2Cor, it has better preserved the spectral shape in both bloom and nonbloom Barents Sea waters in the blue, green, and NIR bands. The C2RCC processor is provided in the SNAP processing toolbox from ESA. In addition to calibrated TOA reflectances, the C2RCC requires salinity, ozone, air pressure, and temperature as input parameters. The average temperature and salinity were set to 8° C and 34.5 PSU following Climate Explorer.[2] The remaining parameters were set to default values [37].

Any pixel corresponding to the *in situ* measurements that passed the recommended quality flags [37] is considered a potentially valid pixel and selected for further processing. The quality flags used in the current study include Cloud_risk, Rtosa_OOS, Rhow_OOS, and VALID_PE. The Cloud_risk flag indicates cloudy conditions, and any pixel affected by clouds was excluded. The Rtosa_OOS flag is true when the input spectrum to the C2RCC-net algorithm is out of the training range; therefore, the inversion of TOA R_{rs} to surface R_{rs} is most likely to be incorrect. The Rhow_OOS flag is true when the input spectrum to the IOP neural net is not within the training range of the neural net. The inversion is likely to be wrong in this case as well. The VALID_PE is the operator's valid pixel expression, which is true for valid pixels and false otherwise [38].

[2]Online. [Available]: https://climexp.knmi.nl/

B. Proposed One-to-One Match-Up Selection

The *in situ* measurements of Chl-a are matched with the corresponding R_{rs} pixels using a baseline setting of one-to-one matching. In this matching scheme, each *in situ* measurement is matched to the nearest pixel in the satellite image [37]. The baseline scheme is then extended to one-to-window matching, where each *in situ* measurement is matched to all the valid pixels in a window of size 3×3, centered at the *in situ* location. The valid pixels correspond to the water leaving R_{rs} that pass the quality flags as well as the filtering criterion defined below. The one-to-window matching can also be considered as a data augmentation technique and it has resulted in improved performance of the proposed as well as the compared algorithms.

Since the satellite data have already been resampled from 10 and 20 to 60-m resolution, instead of associating the *in situ* samples with a mean or median of a window of 3×3 pixels [34], [38], each Chl-a measurement was matched to the spatially closest pixel [37]. Only water pixels that passed the aforementioned quality flags were included in the match-up dataset.

The time window between the *in situ* and satellite data significantly affects the size and quality of the match-up dataset. Allowing a longer time gap produces more match-ups but risk the reliability of the system due to the dynamic nature of water body especially in the coastal waters [37]. Considering the ocean dynamics and the larger training data requirement of ML algorithms to learn the mapping between R_{rs} and Chl-a concentrations, we have proposed a new match-up selection criterion based on the spectral distribution of R_{rs}. After applying the quality flags, potentially valid pixels are processed to remove the nonphysical and unrealistic measurements in-terms of spectral distribution and amplitude that arise due to the time-gap between the *in situ* and satellite data or errors in the AC algorithm. The filtering operation is performed using the shape characteristics of the spectral distribution. By carefully analyzing the samples, i.e., the *in situ* Chl-a and the corresponding R_{rs} spectra, when the time-gap between the *in situ* observations and satellite images is small, we observe that the R_{rs} spectra corresponds to the same spectral distribution as reported in previous studies [34], [64]. The data samples not following the spectral ratio criterion are outliers and therefore removed from the match-up dataset

$$\begin{cases} \text{If Chl-a } < 1 \text{ mg/m}^3 \text{ then } \frac{R_{rs}(\lambda_{560nm})}{R_{rs}(\lambda_{492nm})} < 1 \\ \text{If Chl-a } \geq 1 \text{ mg/m}^3 \text{ then } \frac{R_{rs}(\lambda_{560nm})}{R_{rs}(\lambda_{492nm})} \geq 1. \end{cases}$$

Increasing Chl-a generally result in higher reflectance across the green and NIR region of the spectrum [7], [44], [45]. CDOM, on the other hand, tends to reduce the reflectance, especially below 500 nm [37]. By carefully observing the match-ups, with an increase in the time-gap (within ±1 day), in some cases, we observe high reflectance at 492 nm instead at 560 nm despite high Chl-a concentration, which we consider as outliers. It should be

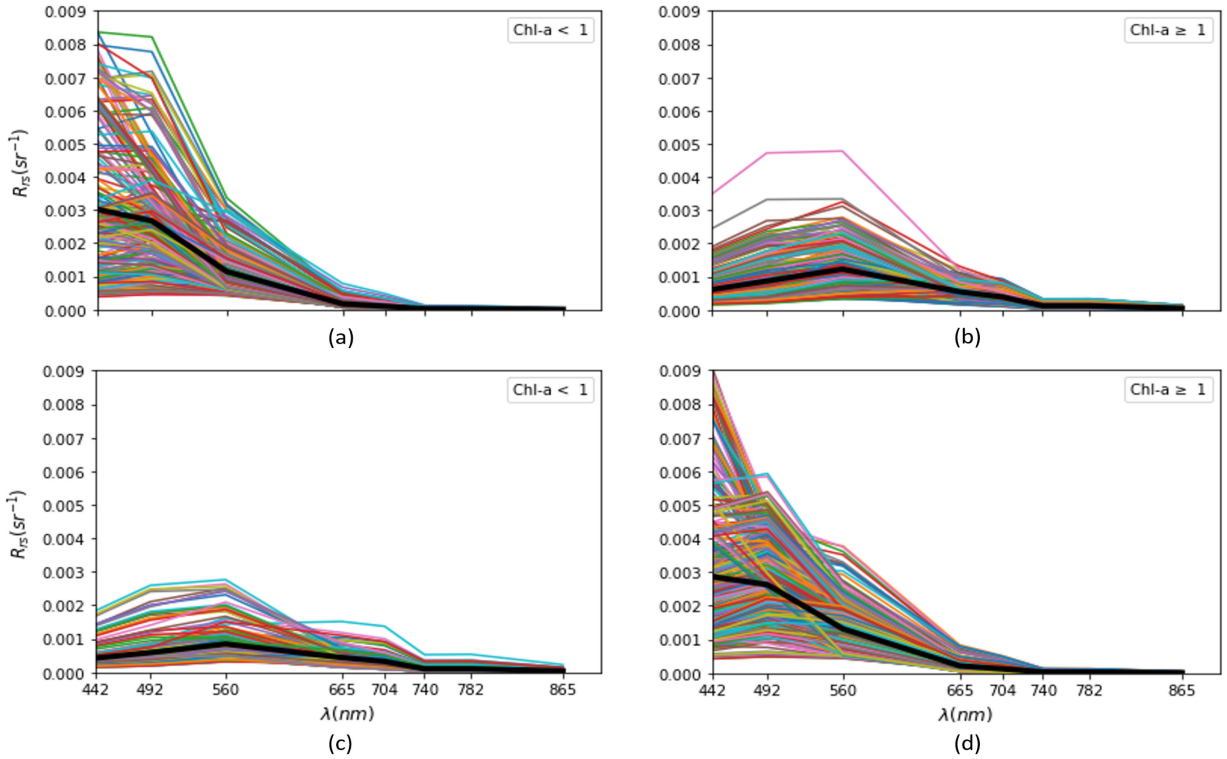

Fig. 3. Match-up R_{rs} spectra of Chl-a concentrations after filtering when (a) Chl-a <1 and (b) Chl-a ≥ 1. Erroneous R_{rs} spectra when (c) Chl-a <1 and (d) Chl-a ≥ 1. The black curves represent mean concentration of Chl-a. The time-gap between *in situ* and satellite data is $\leq \pm 1$ day.

TABLE III
OCN MODEL PARAMETERS FOR CHL-A RETRIEVAL

Parameters	**Value/Selection**	**Description**
Layers	4	input-layer, 2 hidden-layers, output-layer
Number of Neurons	11,25, 25,1	input-layer, 2 hidden-layers, output-layer
Weight Initialization	Xavier	
Activation Function	tanh	
Learning Process	mini-batch gradient descent	
Loss Function	RMSLE	
Regularization	Batch-Normalization and L2-norm	
Optimizer	Adam	initial learning rate=0.0075
Batch-size	32	

noted that these abnormal R_{rs} spectra are not due to CDOM; otherwise, the R_{rs} spectra, irrespective of Chl-a concentration, would have shown low reflectance in the blue wavelength mainly below 500 nm. The observed spectral behavior for Chl-a ≤ 1.0 and Chl-a >1.0 are quite different as shown in Fig. 3(a) and (b). In Fig. 3(c), it can be seen that the erroneous R_{rs} spectra (peaks in the green wavelength) for low concentrations of Chl-a has almost the same order of magnitude as the R_{rs} spectra that are physically correct and included in the match-ups [Fig. 3(b)]. We also observe that the green or NIR to red band ratios showed no significant relationship with Chl-a concentrations in match-ups or outliers. Moreover, R_{rs} in the NIR band is low compared to the green band and do not show significant variations. This means that the R_{rs} spectra are not effected by suspended solid matter. These erroneous R_{rs} spectra may have aroused due to the time difference between the *in situ* and satellite data or uncertainties in the AC algorithm. We experimentally observe that if these abnormal measurements are not removed from the training data, all the methods show degraded performance, as shown in Fig. 4 and Table V (Case iv). The proposed match-up selection technique makes the remaining set of observations consistent with the spectral behavior of Chl-a, as reported in the previous studies [7], [34]. It allows to use a larger time window to increase the match-up dataset while reducing the adverse effect caused by the temporal mismatch between the *in situ* and the satellite data and errors in the AC algorithm [37].

C. Proposed One-to-Window Match-Up Selection

Instead of associating the *in situ* samples with a single nearest pixel in the satellite image, we consider associating it with all potentially valid R_{rs} that pass the quality flags in a window of 3×3 pixels, centered at the *in situ* location. Within the window, if a pixel is identified as invalid, then the mean of the remaining

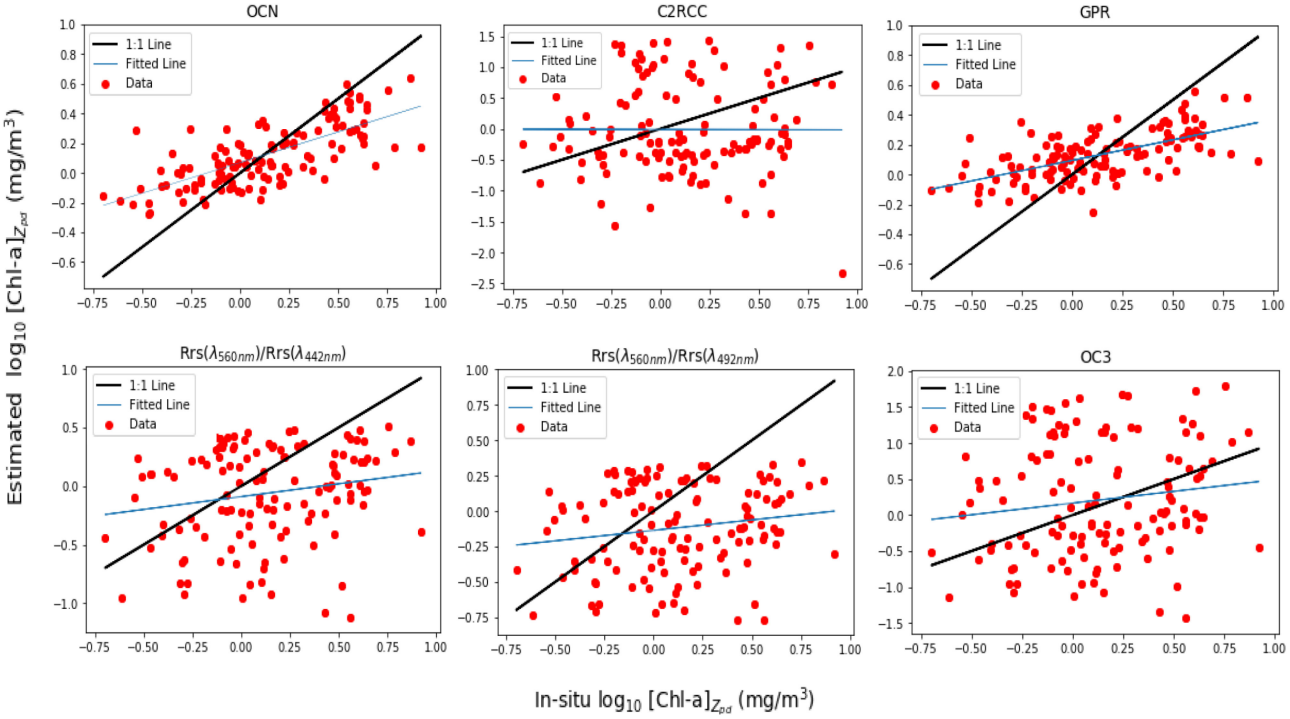

Fig. 4. Performance evaluation of $[\text{Chl-a}]_{Zpd}$ retrievals using OCN, C2RCC-net, GPR, band ratios, and OC3 algorithms using one-to-window approach without applying filtering operation. The total number of test samples are 109. The overall and range-specific performances are included in Table V (Case iv), respectively.

water leaving R_{rs} that pass the quality flags, is used as a replacement of that pixel. Also, if more than one pixels fail to pass the quality flags then one of them is replaced by the mean of valid pixels but the remaining pixels are removed from the window to avoid leakage of data during the training of ML methods. After that, the filtering operation discussed in the last section is applied to remove the erroneous spectra. In the remaining text, the term valid pixels means the R_{rs} pixels that have passed the quality flags and the proposed filtering operation discussed in Sections IV-A and IV-B. The terms invalid and erroneous are considered as the same.

Matching *in situ* Chl-a to all valid pixels in a window of 3×3 pixels increases the training and validation samples and improves the learning performance of ML methods. During testing, estimating Chl-a over a window may predict different values depending on the variability in R_{rs} values. To obtain final Chl-a value corresponding to the *in situ* measurement, fusion is performed by computing median over the predicted values. Thus our approach results in an increase in the number of match-ups and have shown improved performance of all the compared algorithms.

D. Proposed Depth-Integrated Match-Up Creation

In the previous sections, the one-to-one and one-to-window match-up datasets were created using the surface Chl-a *in situ* concentrations. The Chl-a profiles indicate that in most cases, the water samples collected at certain depths have higher concentrations of Chl-a than the surface, as illustrated in Fig. 5. Therefore, in this section, we extend both the one-to-one and one-to-window match-ups to one-to-one-depth-integrated and one-to-window-depth-integrated match-ups selection techniques. Meaning that the depth-integrated-weighted-averaged Chl-a concentration is first matched to a single pixel and then to a window of 3×3 pixels as described in the previous sections. These match-ups were made by computing depth-integrated-weighted-averaged Chl-a concentrations which turned out to be more accurate than the surface Chl-a values in estimating phytoplankton biomass.

To compute the depth-integrated-weighted-averaged-Chl-a from the Chl-a concentrations measured at discrete depths z, we have followed the approach developed in Uitz *et al.* [33] which is based on the work [65]. Let $[\text{Chl-a}]_{Zpd}$ be the Chl-a concentrations presumably seen by a satellite. It may be computed over the first optical depth Z_{pd} also known as penetration depth, as follows:

$$[\text{Chl-a}]_{Zpd} = \frac{\int_0^{Z_{pd}} C(z) exp(-2k_d z) dz}{\int_0^{Z_{pd}} exp(-2k_d z) dz} \tag{1}$$

where $C(z)$ represents Chl-a concentrations collected at discrete depths, $\exp(-2k_d z)$ is an exponentially decreasing function which assigns higher weight to the surface Chl-a and lower weights to the samples collected at increasing depths. The attenuation coefficient of the down-welling solar irradiance is given by $k_d = 4.6/Z_{eu}$, where Z_{eu} is the euphotic-depth which may be computed for the open oceans [65]

$$Z_{eu} = 568.2[C_{\text{tot}}]^{-0.746} \tag{2}$$

where $C_{\text{tot}} = \int_0^z C(z)dz$. We observed that, the penetration depth Z_{pd} varies from 2.5–17 m with a mean of 7±2.5 m in the bloom season (April–May), as shown in Fig. 5. In the remaining months which are less productive (June–October), Z_{pd} varies from 4–22 m with a mean 9±3.14 m. As illustrated in Fig. 5(a),

TABLE IV
PERFORMANCE COMPARISON OF THE PROPOSED OCN ALGORITHM WITH EXISTING STATE-OF-THE-ART METHODS IN THREE DIFFERENT MATCH-UPS, EACH ESTIMATING SURFACE CHL-A $[\text{CHL-A}]_{\text{SURF}}$ AND DEPTH-INTEGRATED CHL-A $[\text{CHL-A}]_{Zpd}$

Method	MSE	RMSE	Slope	R^2	MSLE	RMSLE	MAE	Bias
One-to-one Match-ups								
[Chl-a]$_{surf}$								
Proposed OCN	2.361	1.536	**0.779**	**0.579**	**0.070**	**0.266**	**1.654**	1.044
GPR	2.296	1.515	0.712	0.500	0.083	0.289	1.703	1.045
$OC3_{LT}$	**1.903**	**1.379**	0.740	0.534	0.078	0.279	1.680	**1.013**
$R_{rs}(\lambda_{560nm})/R_{rs}(\lambda_{442nm})$	2.026	1.423	0.760	0.380	0.105	0.324	1.808	1.382
$R_{rs}(\lambda_{560nm})/R_{rs}(\lambda_{492nm})$	2.860	1.691	0.775	0.364	0.106	0.326	1.842	1.581
OC3	37.534	6.126	0.768	-0.760	0.297	0.545	2.667	0.884
C2RCC	42.823	6.544	0.662	-0.870	0.315	0.561	2.618	1.169
[Chl-a]$_{Zpd}$								
Proposed OCN	**1.424**	**1.193**	**0.810**	**0.650**	**0.055**	**0.236**	**1.541**	**0.995**
GPR	2.115	1.454	0.750	0.560	0.071	0.266	1.660	1.049
$OC3_{LT}$	1.738	1.318	0.750	0.553	0.072	0.268	1.649	1.019
$R_{rs}(\lambda_{560nm})/R_{rs}(\lambda_{442nm})$	1.944	1.394	0.752	0.321	0.109	0.331	1.840	1.432
$R_{rs}(\lambda_{560nm})/R_{rs}(\lambda_{492nm})$	2.785	1.669	0.773	0.317	0.110	0.332	1.871	1.632
OC3	36.686	6.056	0.767	-0.860	0.301	0.548	2.694	0.930
C2RCC	41.974	6.478	0.657	-1.027	0.328	0.572	2.700	1.252
One-to-window Match-ups								
[Chl-a]$_{surf}$								
Proposed OCN	**0.680**	**0.824**	**0.915**	**0.833**	**0.025**	**0.159**	**1.293**	0.947
GPR	0.842	0.917	0.898	0.800	0.029	0.172	1.367	0.981
$OC3_{LT}$	1.587	1.259	0.757	0.569	0.065	0.256	1.643	0.942
$R_{rs}(\lambda_{560nm})/R_{rs}(\lambda_{442nm})$	1.709	1.307	0.705	0.421	0.087	0.296	1.772	1.122
$R_{rs}(\lambda_{560nm})/R_{rs}(\lambda_{492nm})$	2.287	1.512	0.706	0.390	0.092	0.304	1.761	1.344
OC3	35.044	5.919	0.710	-0.844	0.280	0.529	2.644	0.645
C2RCC	36.930	6.077	0.562	-0.908	0.290	0.538	2.625	**1.000**
[Chl-a]$_{Zpd}$								
Proposed OCN	**0.420**	**0.650**	**0.936**	**0.880**	**0.018**	**0.134**	**1.275**	0.967
GPR	0.770	0.880	0.903	0.820	0.026	0.163	1.341	**0.990**
$OC3_{LT}$	1.558	1.248	0.748	0.557	0.064	0.254	1.641	0.957
$R_{rs}(\lambda_{560nm})/R_{rs}(\lambda_{442nm})$	2.259	1.503	0.697	0.333	0.096	0.310	1.791	1.406
$R_{rs}(\lambda_{560nm})/R_{rs}(\lambda_{492nm})$	1.664	1.290	0.695	0.368	0.091	0.302	1.800	1.175
OC3	32.620	5.711	0.700	-0.908	0.276	0.526	2.629	0.680
C2RCC	35.616	5.968	0.552	-0.990	0.290	0.538	2.637	1.045
One-to-median Match-ups								
[Chl-a]$_{surf}$								
Proposed OCN	**1.832**	**1.353**	**0.765**	**0.578**	**0.070**	**0.265**	**1.670**	1.020
GPR	2.218	1.489	0.721	0.511	0.081	0.286	1.709	1.095
$OC3_{LT}$	2.142	1.463	0.738	0.543	0.076	0.276	1.698	**1.014**
$R_{rs}(\lambda_{560nm})/R_{rs}(\lambda_{442nm})$	1.952	1.397	0.744	0.454	0.091	0.302	1.783	1.192
$R_{rs}(\lambda_{560nm})/R_{rs}(\lambda_{492nm})$	2.633	1.622	0.745	0.423	0.096	0.310	1.788	1.407
OC3	44.707	6.686	0.744	-0.871	0.313	0.559	2.832	0.687
C2RCC	46.526	6.821	0.590	-0.920	0.322	0.567	2.820	0.887
[Chl-a]$_{Zpd}$								
Proposed OCN	**1.582**	**1.258**	**0.790**	**0.626**	**0.058**	**0.242**	**1.592**	0.975
GPR	1.728	1.314	0.746	0.556	0.069	0.264	1.653	1.018
$OC3_{LT}$	1.919	1.386	0.735	0.538	0.073	0.270	1.689	**0.993**
$R_{rs}(\lambda_{560nm})/R_{rs}(\lambda_{442nm})$	1.836	1.355	0.730	0.392	0.095	0.309	1.815	1.233
$R_{rs}(\lambda_{560nm})/R_{rs}(\lambda_{492nm})$	2.499	1.580	0.733	0.372	0.098	0.314	1.804	1.446
OC3	42.637	6.520	0.733	-1.000	0.316	0.562	2.880	0.726
C2RCC	44.303	6.656	0.587	-1.010	0.316	0.563	2.809	0.916

The best results are shown in bold.

the maxima of Chl-a occurs in the upper column (1–12 m) in the bloom season and lies within the penetration depth. The Chl-a concentration deceases in the remaining months, however, the mean pigment profile almost show a similar trend, as depicted in Fig. 5(b). Due to the deceased concentrations of Chl-a the mean penetration depth also shows an increment of 2 m, compared to the bloom season.

To create depth-integrated Chl-a concentration match-ups, we first compute $[\text{Chl-a}]_{Z_{pd}}$ using (1). In order to filter out the outliers and uncertainties in the remotely sensed data we have proposed conditions based on the Chl-a spectral distributions in Section III(d). Previously we have used surface Chl-a ($[\text{Chl-a}]_{\text{surf}}$) in these filters, while now we use the depth-integrated averaged Chl-a, denoted by $[\text{Chl-a}]_{Zpd}$. Following the match-up selection and the filtering process, 78 matched pairs are finally selected for the one-to-one scheme and 514 match-ups for one-to-window settings, which are then used to develop Chl-a concentration retrieval algorithms.

TABLE V
PERFORMANCE COMPARISON BETWEEN THE OCN, GPR, OC3, AND SPECTRAL BAND RATIO METHODS IN RETRIEVING $[\text{CHL-A}]_{Zpd}$ IN ONE-TO-WINDOW CONFIGURATION USING FOUR DIFFERENT FILTERING CASES (I-IV) AS DEFINED IN SECTION VI-B

Method	MSE	RMSE	Slope	R^2	MSLE	RMSLE	MAE	Bias
Case i								
OCN	**0.424**	**0.651**	**0.916**	**0.840**	**0.023**	**0.150**	**1.309**	0.958
GPR	0.490	0.700	0.901	0.807	0.026	0.163	1.352	**0.988**
$OC3_{LT}$	1.352	1.163	0.734	0.532	0.068	0.259	1.655	0.938
$R_{rs}(\lambda_{560nm})/R_{rs}(\lambda_{442nm})$	1.556	1.247	0.677	0.209	0.110	0.332	1.861	1.351
$R_{rs}(\lambda_{560nm})/R_{rs}(\lambda_{492nm})$	1.351	1.483	0.687	0.197	0.112	0.335	1.888	1.562
OC3	25.923	5.091	0.692	-0.969	0.275	0.524	2.577	0.901
C2RCC	24.16	4.914	0.590	-0.850	0.258	0.508	2.517	1.306
Case ii								
OCN	**0.414**	**0.643**	**0.911**	**0.828**	**0.022**	**0.150**	**1.294**	0.962
GPR	0.473	0.687	0.887	0.783	0.0286	0.169	1.366	**1.009**
$OC3_{LT}$	1.115	1.056	0.706	0.490	0.068	0.262	1.657	0.931
$R_{rs}(\lambda_{560nm})/R_{rs}(\lambda_{442nm})$	1.536	1.239	0.620	-0.115	0.147	0.383	2.022	1.547
$R_{rs}(\lambda_{560nm})/R_{rs}(\lambda_{492nm})$	2.162	1.470	0.636	-0.059	0.139	0.373	2.055	1.738
OC3	21.999	4.689	0.645	-1.361	0.311	0.557	2.683	1.163
C2RCC	20.880	4.569	0.577	-1.044	0.269	0.519	2.601	1.589
Case iii								
OCN	0.680	**0.824**	**0.915**	**0.833**	**0.025**	**0.159**	**1.293**	0.947
GPR	**0.667**	0.817	0.874	0.752	0.030	0.174	1.388	**1.013**
$OC3_{LT}$	1.365	1.169	0.653	0.421	0.073	0.269	1.705	0.948
$R_{rs}(\lambda_{560nm})/R_{rs}(\lambda_{442nm})$	1.524	1.234	0.592	-0.158	0.143	0.378	2.017	1.436
$R_{rs}(\lambda_{560nm})/R_{rs}(\lambda_{492nm})$	2.040	1.428	0.600	-0.069	0.132	0.363	1.998	1.636
OC3	28.222	5.312	0.604	-1.849	0.351	0.593	2.921	0.991
C2RCC	30.000	5.477	0.515	-1.516	0.310	0.557	2.817	1.336
Case iv								
OCN	**1.365**	**1.161**	**0.722**	**0.511**	**0.060**	**0.246**	**1.537**	**1.006**
GPR	1.636	1.279	0.669	0.422	0.071	0.267	1.644	1.016
$OC3_{LT}$	2.414	1.554	0.238	0.055	0.121	0.348	1.949	0.984
$R_{rs}(\lambda_{560nm})/R_{rs}(\lambda_{442nm})$	2.965	1.722	0.188	-1.200	0.272	0.522	2.685	1.549
$R_{rs}(\lambda_{560nm})/R_{rs}(\lambda_{492nm})$	3.171	1.780	0.172	-0.920	0.238	0.488	2.567	1.758
OC3	36.261	6.022	0.141	-4.261	0.653	0.808	4.527	1.054
C2RCC	44.942	6.703	0.003	4.430	0.674	0.821	4.734	1.379

The best results are shown in bold.

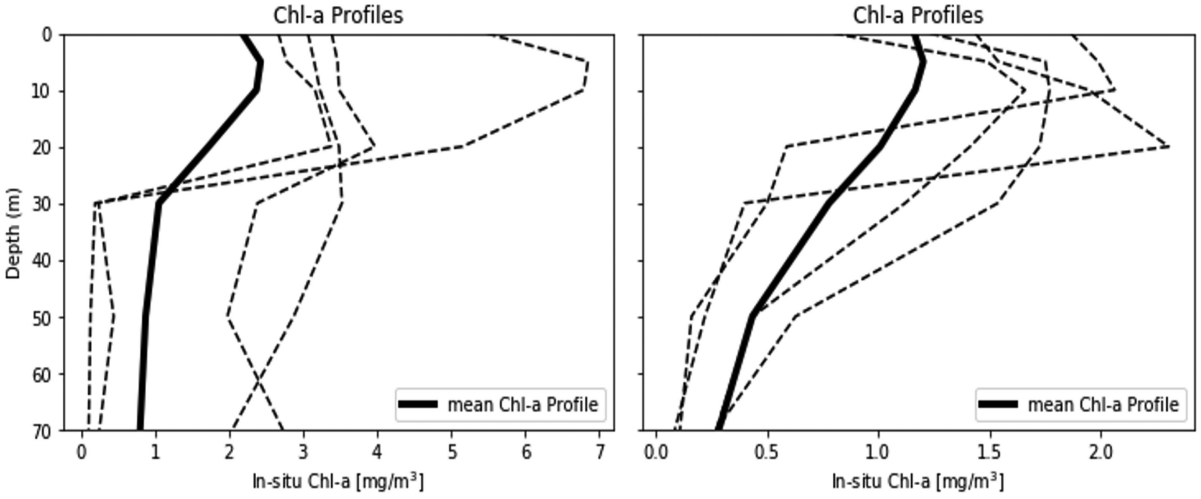

Fig. 5. Chl-a profiles plotted as function of geometrical depth for the year 2016–2018 in the Barents Sea (a) April–May (bloom season) and (b) June–October. The dotted lines represent some examples of Chl-a vertical distribution while the thick black lines represent the averaged Chl-a profiles over the complete dataset.

V. PROPOSED MACHINE LEARNING METHODOLOGY

ANNs have been proven to be efficient tools in studying nonlinear dynamic systems in various fields, including remote sensing, medicine, environmental studies, machine vision, and surveillance [66], [67]. ANNs have previously been used for Chl-a estimation [30]–[32]; however, to the best of our knowledge, no thorough study has been conducted to explore the efficiency of ANNs, in the domain of O monitoring in the Barents sea and Norwegian Coastal areas. This may be partially due to the unavailability of match-up datasets for the given area of observation and uncertainties associated with the remotely sensed data. In the current work, the architecture of fully connected

feed-forward MLP is explored for OC monitoring (Table III). It is applied to different types of match-up datasets discussed in the last section and compared with the existing state-of-the-art Chl-a retrieval techniques. In the following subsections, we explain the proposed OCN and its training process using the match-up datasets proposed in the last section.

A. Chlorophyll Estimation Using OCN

The proposed OCN model is trained using 10 input features utilizing the eight bands centered at 443, 492, 560, 665, 704, 740, 782, 865 nm, and the two ratios of green (560 nm) to blue bands (443 and 492 nm) due to their high sensitivity for changes in Chl-a concentrations. Each input R_{rs} feature is normalized between 0.00 and 1.00 before input to the OCN. The Chl-a content in mg/m^3) is converted into log-scale before using it as target values, as proposed in the previous studies [8], [37]. It follows a normal or near-normal distribution and reduces skewness in the data. There are a number of hyperparameters to tune in this network, including the number of hidden layers, loss function, activation function, learning rates, and regularization. These choices must be carefully opted to get a more accurate output of the model. In this study, different designs of ANN with various weight initialization techniques, number of hidden layers, varying number of neurons in each hidden layer, different activation functions, regularization techniques, optimization algorithms with varying learning rate and batch-size were implemented, and the one with two hidden layers having 25 neurons each and tanh activation function is found to be the best performer based on the validation loss. We experimentally observed that the network with higher number of hidden layers and neurons is effected by overfitting. After the activation function, the batch normalization was applied after each hidden layer for regularization [68]. The output of OCN is a single value of Chl-a, which is fed into the loss function. The optimization process minimizes the difference between the estimated and the *in situ* Chl-a concentrations using the backpropagation algorithm. The loss function is based on the root mean square log error (RMSLE) along with ℓ_2 norm on the weights and the biases, w and b

$$L = \sqrt{\frac{1}{N}\sum_{i=1}^{N}(\log_{10}(y_i) - \log_{10}(\widehat{y_i}))^2 + \lambda_1 \ell_2(W, b)} \quad (3)$$

where $\widehat{y_i}$ is the predicted and y_i is the corresponding ground-truth value, N is the total number of samples, and λ_1 is a hyperparameter used to assign relative importance to the second term.

1) Optimization Process: The backpropagation algorithm uses a minibatch gradient descent method to compute the gradients (g_t) of the cost function w.r.t. to the weights w and biases b of the network. This algorithm aims to find model weights and coefficients that minimize the loss over a minibatch during training. The training parameters are updated using n training examples (x_n, y_n) instead of a single example or whole training dataset. At each time step t the cost function is minimized as follows:

$$w_{t,n} = w_{t-1,n} - \eta g_{t,n} \quad (4)$$

where $g_{t,n} = \nabla_w L, \nabla_w$ is the gradient of the loss function L defined by (3) which is differentiable w.r.t. weights. The parameter η is the learning rate which represents the amount of change induced in the weights during each minibatch iteration. In the current work, Adam optimizer is used for faster convergence of the model. The batch size is fixed to 64 samples in all experiments. The initial learning rate η_0 was set 0.0075 which decreases by 2% after every 100 epochs. These two hyperparameters are tuned based on the training and validation error during the training process. In our model, the weights and biases were initialized using the Xavier method [69]. An improvement in the convergence rate and accuracy of the model was observed by initializing network weights using the Xavier method.

2) Batch Normalization: Updates in the parameters being learned in the preceding layers cause a continuous change in the distribution of inputs to the later layers, which then need to readjust according to the changed distribution, slowing down the convergence of the network. In order to avoid the internal covariance shift, batch-normalization has been applied. This is achieved by controlling the mean and variance of the input distributions. This technique reduces the internal covariance shift between layers, stabilizes, and speeds up the learning process [68]. The Chl-a performance estimation improved by $>5\%$ after the implementation of batch-normalization. For an n-dimensional input-batch $x = x_{i...n}$, the batch normalized is performed as follows:

$$\widehat{x_i} = \frac{x_i - E[x_i]}{\sqrt{\text{var}[x_i]}} \quad (5)$$

where x_i is a particular input to the layer, $\hat{x_i}$ represents the normalized input, $E(x_i)$ is the batch mean, and var(x_i) is the variance of the batch. The output of the layer is then scaled and shifted

$$y_i = \alpha \widehat{x_i} + \beta \quad (6)$$

where α and β are scaling and shifting parameters which are learned during the training.

B. Experimental Setup

To evaluate the proposed OCN and the other ML methods, the match-ups are randomly split into 90% training and 10% testing samples. Experiments are repeated with tenfold cross-validation. The training data in each split are further divided into training and validation (90% and 10%) splits for the one-to-one configuration and (70% and 30%) for one-to-window match-up configuration due to higher number of match-ups. Using the training data only, the proposed OCN model is trained for 5000 epochs. In order to properly tune the hyperparameters and avoid overfitting, the OCN model with weights and bias terms having minimum validation loss during the training iterations is utilized to estimate Chl-a on unseen test data. The OCN model is developed in tensor flow.

The GPR is implemented in Python using Scikit-learn Machine Learning Toolkit [70] and is trained using the same training splits. Radial basis function (RBF) is used with GPR since

it performs better than the linear kernel. The kernel hyperparameters are optimized on the validation split by maximizing the log-marginal-likelihood (LML) using the limited memory Broyden–Fletcher–Goldfarb–Shanno algorithm. As the LML may have multiple local minima, the optimizer is randomly initialized 10 times, and the best performer is selected. The noise level in the targets which is a value added to the diagonal of the kernel matrix during fitting is also fine-tuned. The RMSLE is computed N times during each cross-validation step and based on it, $alpha$ is selected for the test split. A significant improvement in the GPR model is observed after fine-tuning $alpha$ compared to the default values.

In this work, two versions of the OC3 algorithm are compared, a globally trained version and a locally trained version, $OC3_{LT}$. The $OC3_{LT}$ is trained by combining training and validation splits, as explained in Appendix A.

C. Performance Indicators

To compare the performance of different methods, a number of linear and log-transformed metrics are used. These metrics include the RMSLE, MSLE, MSE, mean absolute log error (MAE) computed in log-space, bias, and coefficient of determination, R^2. The metrics computed in log-space provide a better assessment of the algorithmic performance as the log-transformed data follows a normal or near-normal distribution. In addition to the above metrics, we have also included linear regression slopes to facilitate comparison between different methods

$$\text{RMSE} = \sqrt{\frac{1}{N_t}\sum_{i=1}^{N_t}((y_i) - (\widehat{y_i}))^2} \tag{7}$$

$$\text{RMSLE} = \sqrt{\frac{1}{N_t}\sum_{i=1}^{N_t}(\log_{10}(y_i) - \log_{10}(\widehat{y_i}))^2} \tag{8}$$

$$\text{MSE} = \frac{1}{N_t}\sum_{i=1}^{N_t}((y_i) - (\widehat{y_i}))^2 \tag{9}$$

$$\text{MSLE} = \frac{1}{N_t}\sum_{i=1}^{N_t}(\log_{10}(y_i) - \log_{10}(\widehat{y_i}))^2 \tag{10}$$

$$\text{Bias} = 10^{\frac{1}{N_t}\sum_{i=1}^{N_t}(\log_{10}(y_i) - \log_{10}(\widehat{y_i}))} \tag{11}$$

$$\text{MAE} = 10^{\frac{1}{N_t}\sum_{i=1}^{N_t}|\log_{10}(y_i) - \log_{10}(\widehat{y_i})|} \tag{12}$$

$$R^2 = 1 - \frac{\sqrt{\sum_{i=1}^{N_t}(\log_{10}(y_i) - \log_{10}(\widehat{y_i}))^2}}{\sqrt{\sum_{i=1}^{N_t}(\log_{10}(y_i) - \log_{10}(\bar{y_i}))^2}} \tag{13}$$

where $\widehat{y_i}$ is the predicted and y_i is the corresponding ground-truth Chl-a concentration, N_t is the number of test samples, and $\bar{y}_i = \frac{1}{N}\sum_{i=1}^{N} y_i$ is the mean Chl-a value in the test dataset. A bias of 1.5 implies that Chl-a estimations are, on average, 50% larger than the actual measurements [71].

VI. Results and Discussion

The performance statistics on Chl-a estimation are computed for three different configurations each including surface chlorophyll, $[\text{Chl-a}]_{\text{surf}}$, and depth-integrated chlorophyll, $[\text{Chl-a}]_{Zpd}$, estimation. These three configurations include one-to-one match-ups, one-to-window match-ups, and one-to-median match-ups. The median R_{rs} value for each band is computed by taking median over all the valid pixels in a 3×3 window [8], [34], [38].

A. Performance Evaluation

In most of these experiments, the proposed OCN has consistently shown best performance over all indicators compared to the band ratio, the modified OC3 [45], $OC3_{LT}$, and the other ML methods as illustrated in Table IV.

For the estimation of $[\text{Chl-a}]_{\text{surf}}$ in one-to-one configuration, $OC3_{LT}$ has achieved minimum MSE and RMSE (Table IV). However, the remaining performance indicators, which are in log scale, indicate that OCN performs better than GPR, $OC3_{LT}$, and band ratio methods. Also, in estimating $[\text{Chl-a}]_{Zpd}$, MSE and RMSE show that the $OC3_{LT}$ algorithm is the second best performer; however, the remaining indicators do not show favorable results for $OC3_{LT}$. In the one-to-window configuration, the locally trained ML methods, OCN and GPR, are top performers in estimating both $[\text{Chl-a}]_{\text{surf}}$ and $[\text{Chl-a}]_{Zpd}$, due to the increased number of match-ups.

The scatter-plots in Figs. 6 and B.1–B.5 (Appendix B), further indicate that the globally trained OC3 and C2RCC-net lead to significant overestimation. It should be noted that in these methods Chl-a estimation exceeds 25 mg/m^3 while the *in situ* Chl-a does not exceed 10.81 mg/m^3. In contrast, the band ratio algorithms have shown underestimation. The ML-based models, OCN and GPR, and the locally trained $OC3_{LT}$, are the leading performers in all the configurations. Though, OCN has outperformed GPR and $OC3_{LT}$ by significant margin. Furthermore, the slope between the *in situ* Chl-a and predicted Chl-a in log-scale indicates that the relationship is close to unity (>90) compared with the other empirical and ML-based methods. In our experiments, the proposed OCN has achieved the best fit across the entire range of Chl-a concentration. The other performance indicators as listed in Table IV also show the same trend .

It should be noted that the performance of most of the compared methods has improved by the proposed depth integration, compared to the surface Chl-a estimations. For the case of one-to-one match-ups using OCN, the R^2 value increased from 0.579 to 0.65, while MSE decreased from 2.36 to 1.42. For GPR, the R^2 value increased from 0.50 to 0.56, while MSE decreased from 2.296 to 2.115. A similar trend can be observed in most of the compared methods that demonstrates the significance of using the depth integration approach. Also, we observed that OCN's performance improvement is more significant than the other compared methods because of its capability to learn the nonlinear mapping of R_{rs} into $[\text{Chl-a}]_{Zpd}$.

Significant enhancement can also be observed in most of the compared methods by using the proposed one-to-window

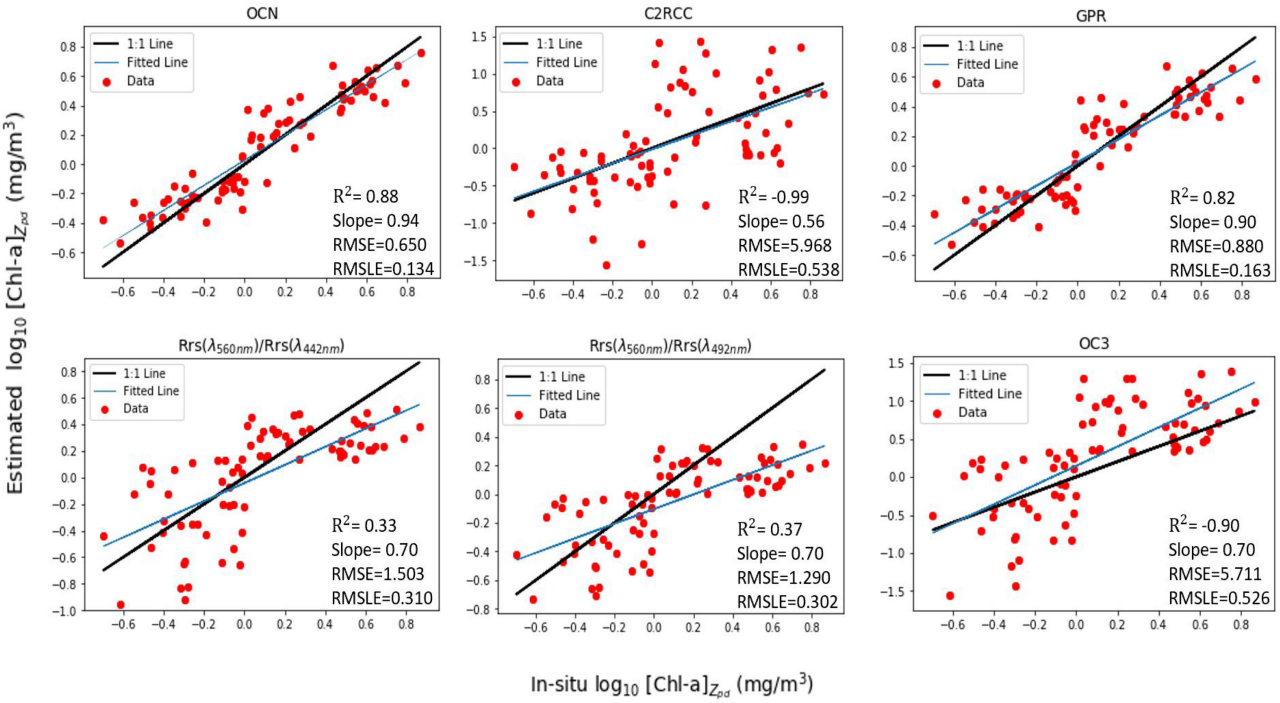

Fig. 6. Performance evaluation of $[\text{Chl-a}]_{Zpd}$ retrievals by the one-to-window approach using the OCN, C2RCC-net, GPR, band ratios, and OC3 algorithms. The total number of test samples are 78.

match-ups configuration. A comparison of one-to-one matchup with one-to-window match-up depicts a decrease in MSLE of OCN from 0.070 to 0.025 for $[\text{Chl-a}]_{\text{surf}}$. In case of $OC3_{LT}$, MSLE decreased from 0.078 to 0.065. A similar trend can be observed in most of the other compared methods because the window approach has leveraged from more data compared to the one-to-one configuration. The one-to-window approach also compensates for the location estimation errors between the *in situ* measurements and the satellite data. It may also handle the Chl-a transport due to the time gap between the *in situ* measurements and the satellite data to some extent.

The combination of depth integration approach with one-to-window configuration yields the benefits of both approaches. In this case, all the compared methods have achieved their best performance compared to the previous experiments as reported in Table IV. In this configuration, OCN's performance with $R^2 = 0.88$, MAE $< 28\%$, and MSLE $= 0.018$, which is not only better than its performance in previous configurations but also better than all of the compared methods. The nearest competitor GPR has obtained R^2 and MSLE of 0.82 and 0.026. These results demonstrate that not only the depth integration and the window-based estimation have individually improved Chl-a estimation but also their combination yields a more significant performance boost to all the compared methods. Thus one may conclude that the proposed improvements are generic and would help enhance the Chl-a estimation methods.

We have also included an additional configuration in our experiments: One-to-median match-ups, which has been previously used in [8], [34], and [38]. We observe that the performance in this configuration is similar to the one-to-one configuration. Compared to the one-to-window configuration, the one-to-median results are lower both in case of $[\text{Chl-a}]_{\text{surf}}$ and $[\text{Chl-a}]_{Zpd}$. These experiments demonstrate that our proposed window approach is better than the previously used match-up approaches due to the higher number of training and validation samples. In case if there is adequate training data, the proposed one-to-window approach is still expected to perform better than one-to-one configuration in open ocean waters, however, it needs to be analyzed on different water types. In the current study we have observed that the erroneous R_{rs} spectra with in a window of 3×3 pixels are due to higher time-gaps between the *in situ* and satellite data and ambiguities in the R_{rs} product in the blue and green bands caused by uncertainties in the AC [37]. However, in highly dynamic inland and coastal waters, where large temporal and spatial variability in Chl-a concentrations may exist [45], the window approach is recommended with modified filtering criterion, for example [36], so that the realistic R_{rs} spectra are not filtered.

B. Analyzing the Filtering Criterion

To further explore the filtering criterion discussed in Section IV-B, we have changed the ratio threshold and computed the performance indicators for the comparison between the compared methods. We experimentally observe that in many cases when Chl-a content is <1 mg/m^3, the R_{rs} spectrum peaks at the blue wavelength ant it tends to shift toward the green region of spectrum for Chl-a concentration 1 mg/m^3. However, in some cases peak of R_{rs} spectra may vary from this observation when Chl-a ranges from 1–1.5 mg/m^3. Therefore, in Table V, we have made a comparison between different methods by varying the

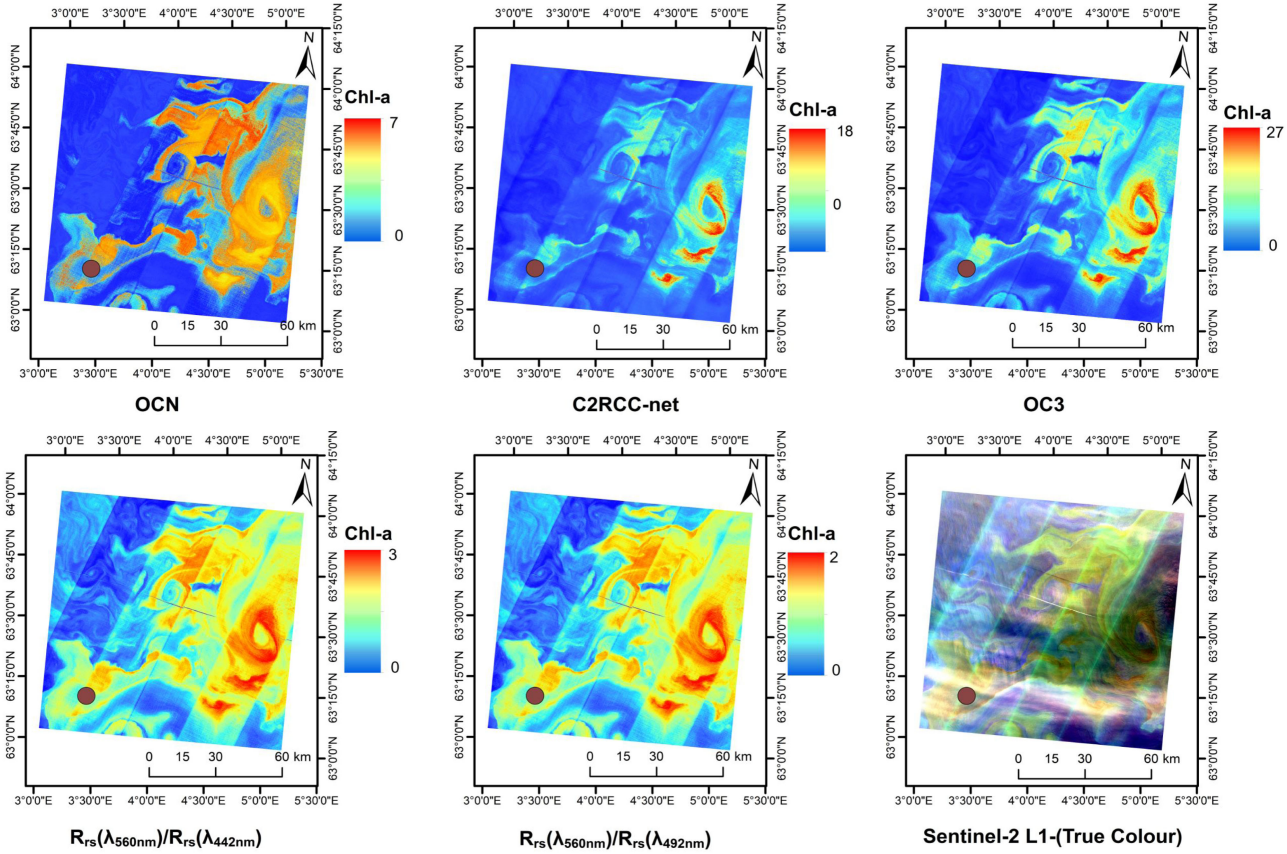

Fig. 7. MSI-derived Chl-a products estimated using OCN, C2RCC-net, OC3, Ratio-1 and Ratio-2 algorithms for near-coincident overpasses of Sentinel-2 A on May 5th, 2017.The marked location (circle) represents *in situ* measurement of Chl-a, and reported as as 4.27 mg/m^3).

threshold in Section IV-B. The four different cases are shown below:

Case i

$$\begin{cases} \text{If Chl-a } < 1.25 \text{ mg/m}^3 \text{ then } \frac{R_{rs}(\lambda_{560nm})}{R_{rs}(\lambda_{492nm})} < 1.25 \\ \text{If Chl-a } \geq 1.25 \text{ mg/m}^3 \text{ then } \frac{R_{rs}(\lambda_{560nm})}{R_{rs}(\lambda_{492nm})} \geq 1.25 \end{cases}$$

Case ii

$$\begin{cases} \text{If Chl-a } < 1.5 \text{ mg/m}^3 \text{ then } \frac{R_{rs}(\lambda_{560nm})}{R_{rs}(\lambda_{492nm})} < 1.5 \\ \text{If Chl-a } \geq 1.5 \text{ mg/m}^3 \text{ then } \frac{R_{rs}(\lambda_{560nm})}{R_{rs}(\lambda_{492nm})} \geq 1.5 \end{cases}$$

Case iii

$$\begin{cases} \text{If Chl-a } < 1.5 \text{ mg/m}^3 \text{ then } \frac{R_{rs}(\lambda_{560nm})}{R_{rs}(\lambda_{492nm})} < 1.5 \\ \text{If Chl-a } \geq 1 \text{ mg/m}^3 \text{ then } \frac{R_{rs}(\lambda_{560nm})}{R_{rs}(\lambda_{492nm})} \geq 1 \end{cases}$$

Case iv

$$\{ \text{ No Filtering .}$$

As evidenced by Table V, the performance of all the methods, including OCN, degrades after changing the filtering threshold; however, OCN degrades more gracefully compared to other methods and maintains its top position. It may be noted that in Case iv, without filtering, the performance of all methods have observed maximum degradation, for example, R^2 reduces from 0.88 to 0.51 in OCN. In Case i –Case iii, the size of match-ups increases by varying the threshold; however, a gradual decrease has been seen in the performance of all compared methods. For OCN, the MSLE and RMSE increased from 0.018 and 0.134 (Table IV) to 0.023 and 0.150 in Case i (Table V). Most performance indicators show almost the same results in Case i and Case ii. However, an increment of 38% and 18% is seen in the RMSLE and MSLE in Case iiiwhich indicate degraded performance in this experiment. These experiments confirm the effectiveness of the proposed threshold of 1.00 in the filtering criterion in Section IV-B.

C. Spatial Maps

To confirm the reliability of the OCN model, the proposed approach is demonstrated for producing Chl-a maps in the Barents Sea. The Sentinel-2 A TOA R_{rs} images were compensated for atmospheric effects using C2RCC-net. For demonstration purposes, visual intercomparisons of Chl-a maps produced by OCN are done with the maps retrieved via C2RCC-net, band ratio methods, and OC3.

Fig. 7 illustrates MSI-derived Chl-a products in the bloom season on May 5th, 2017 generated from the nearest available cloud-free observation made by Sentinel-2 A to the *in situ* measurement. All the algorithms have captured the spatial variability of Chl-a, however, they provide different Chl-a retrievals. For example, OCN produces Chl-a products ranging from 0.3 to 7 mg/m^3, whereas, C2RCC-net and OC3 have overestimated Chl-a, and the band-ratio algorithms estimation does not exceed 3 mg/m^3. The *in situ* measurement at the marked location has reported Chl-a $=$ 4.27 mg/m^3. Amongst

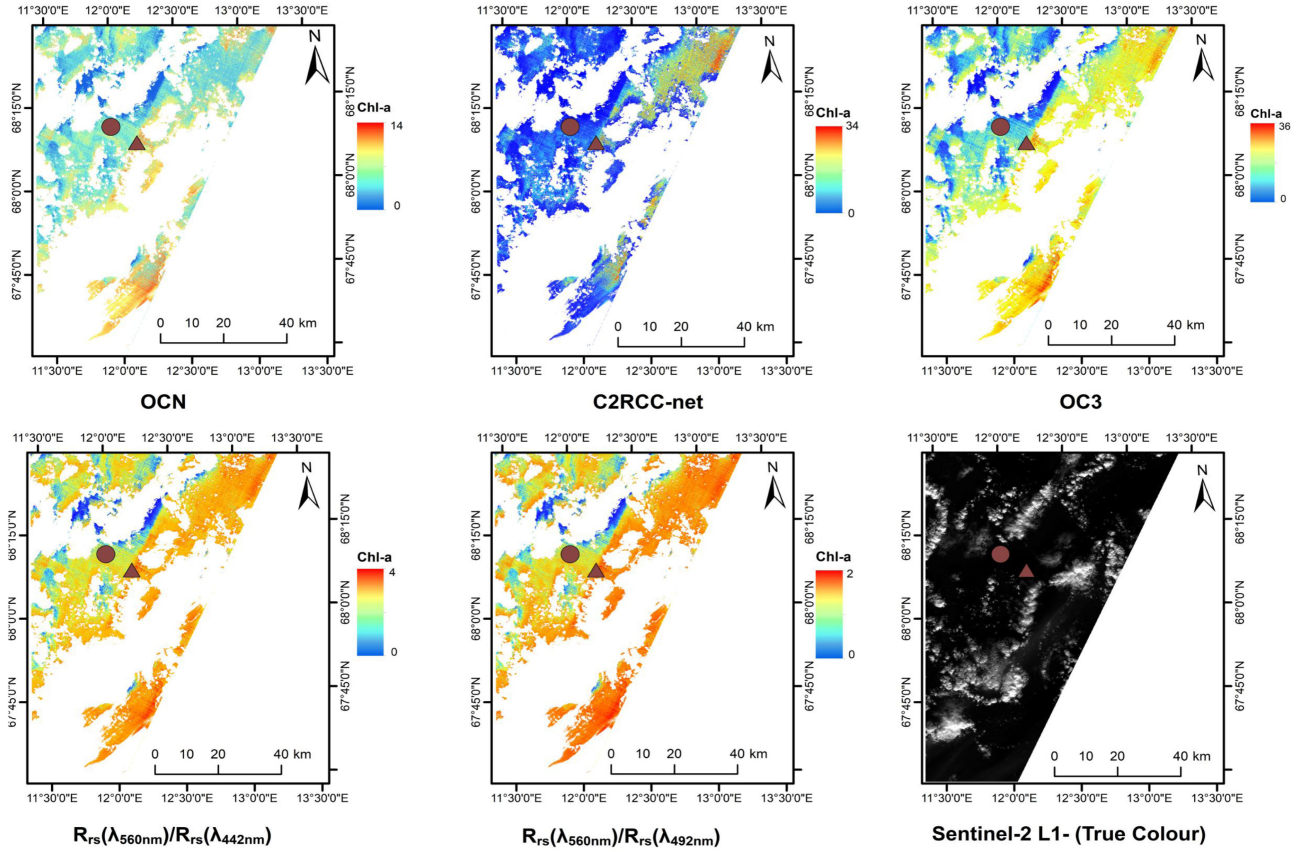

Fig. 8. MSI-derived Chl-a products estimated using OCN, C2RCC-net, OC3, Ratio-1 and Ratio-2 algorithms for near-coincident overpasses of Sentinel-2B on April 5th, 2018. The marked locations (circle and triangle) represents *in situ* measurements reported as 4.9 and 6.14 mg/m^3). The pixels with no-data and flagged as Cloudy are represented by white color. The TOA MSI image was processed to R_{rs} using C2RCC-net.

the mentioned algorithms, OCN estimates are closest to the *in situ* concentration reported as 3.48 mg/m^3 followed by OC3, where estimated Chl-a $=$ 3.02 mg/m^3. The band ratio-1 and ratio-2 algorithms retrieval is underestimated and indicated by 1.62 and 1.15 mg/m^3. The C2RCC-net also underestimates by 400% and reports 1.02 mg/m^3.

Besides, we examine the performance of the proposed OCN on another Sentinel-2B observation generated on April 5th, 2018, in the bloom season, as shown in Fig. 8. From the OCN map, it can be inferred that the proposed model has accurately captured the fine details and abrupt changes in Chl-a distribution. It can be seen that the OCN model successfully produces Chl-a products ranging from 1 to 14 mg/m^3. The estimated Chl-a content by C2RCC-net and OC3 exceeds 30 mg/m^3, which is significantly above the *in situ* observations, indicating overestimation of Chl-a concentrations. The two band-ratio algorithms underestimate the Chl-a concentrations, where the maximum estimated Chl-a is $<$5 mg/m^3. The Chl-a product produced by the OCN model within the Chl-a $\leq$ 14 mg/m^3) range and shows a better correlation with the *in situ* Chl-a concentration. For example, the *in situ* observations of Chl-a reported as 4.9 and 6.14 mg/m^3 at the marked locations, are closely estimated by OCN, i.e., 4.74 and 4.89 mg/m^3 and OC3, i.e., 4.72 and 7.57 mg/m^3, respectively. The OCN and OC3 estimates are quite close to each other, however, OCN predictions are slightly better. While these are underestimated by C2RCC-net and band-ratio algorithms. The C2RCC-net predicts 1.41 and 5.64 and the band-ratio algorithms estimates are quite close to each other. The ratio-1 estimates 1.64 and 1.97 and the ratio-2 estimates 1.31 and 1.53 mg/m^3. These experiments demonstrate that the OCN model has generated reliable Chl-a products.

D. Limitations of the Proposed Approach

The performance of an ML-based model depends on the representativeness of the training dataset. The proposed OCN model is regionally tuned for the Barents Sea. Compared to other Chl-a datasets collected in lakes, inland, and coastal waters [8], [72] covering different water types, the current dataset is limited to Chl-a measurements from the Barents Sea and some region of the Norwegian Sea. Like other ML algorithms, the accuracy of OCN depends on the distribution and uncertainties in the field data. In addition, considering the revisit time of Sentinel-2 MSI and cloud coverage in the high north, our current match-up dataset does not contain adequate training samples from the coastal areas of Svalbard region. However, the training dataset may be extended by using the Landsat-8 and Sentinel-2 MSI virtual constellation product which can achieve improved coverage with reduced revisit time [73].

The proposed one-to-window match-up approach has significantly improved the estimation of OCN, however, if the variation of R_{rs} within a window is large, it may adversely effect the learning and the estimation process. To handle this issue, we have restrained the window size to 3×3 pixels in our experiments.

The proposed match-up criterion is based on the C2RCC derived R_{rs}. The performance of the proposed algorithm in estimating Chl-a is effected by the uncertainties in the AC process [8]. Although we experimentally proved that the proposed filtering and window approaches have improved the performance of OCN and the compared algorithms in open ocean waters, the uncertainties shown in Table IV indicate the need for further improvement in OCN estimation performance. This may be achieved by extending the dataset and simultaneously estimating other in-water parameters such as total suspended matter (TSM) and color dissolved organic matter (CDOM). Learning simultaneous mapping of R_{rs} to these quantities will improve Chl-a estimation and will further straighten the proposed filtering approach.

VII. Conclusion and Future Work

This work aims at improving the estimation of phytoplankton biomass using optical remote sensing integrated with ML techniques over the lately changing Barents Sea. *In situ* Chl-a measurements were collected from the year 2016 to 2018 over a wide area of the Barents Sea and Norwegian Coast. Different match-up dataset creation methods are proposed that exploit the pigment content information at surface as well as within the productive column. Surface and depth-integrated Chl-a concentrations are matched with the nearest pixel/window in the satellite image. A filtering criterion based on R_{rs} spectral distribution is also proposed that allows a larger time-gap between *in situ* and satellite observations and removes outliers.

A NN dubbed as OCN is applied to the inverse problem of estimating Chl-a from R_{rs} extracted from C2RCC-net for Sentinel-2 (MSI) observations. Using the coincident *in situ* and R_{rs} observations, the proposed OCN model is trained, validated, and compared against state-of-the-art approaches, including locally trained GPR and $OC3_{LT}$, globally trained C2RCC, and the empirical methods OC3 and spectral band ratios. Our experiments demonstrate that the proposed OCN is a promising Chl-a retrieval method, and it has performed favorably compared to the existing state-of-the-art methods. The blue and green bands are found more sensitive compared to the red and NIR bands for predicting Chl-a in the Barents Sea. The proposed match-up dataset creation algorithm is generic and it has significantly improved the performance of the OCN and other compared techniques. The R-score and R^2 between *in situ* measurements and the estimated Chl-a using the proposed OCN are highest while the MSE and RMSE are the lowest among the compared methods. Moreover, the proposed OCN model exhibits the best performance in different match-ups configurations.

The obtained results demonstrate the potential of the proposed approach in producing reliable Chl-a products. As evidenced through the spatial maps, the proposed OCN produces more realistic Chl-a map products by accurately capturing the fine details and abrupt changes in Chl-a distribution. Future directions include validation and expansion of OCN on R_{rs} products by various AC algorithms from different satellites as well as collection of *in situ* Chl-a data, including the *in situ* R_{rs} from the northern Barents Sea in the marginal ice zone. Moreover, the *in situ* Chl-a dataset will also be extended through collaboration with IMR, Norway. The OCN implementation will also be extended to simultaneously estimate other various in-water parameters of interest, such as TSM and CDOM.

Contribution

Muhammad Asim: Conceptualization, methodology, experimental work, software, validation of results, and writing of original draft.

Camilla Brekke: Guidance, review of main methodology, designing, reviewing, and editing of the manuscript.

Arif Mahmood: Experimental setup, writing, and editing of the manuscript.

Torbjørn Eltoft: Review of approach, design, and editing of the article.

Marit Reigstad: Provided ideas/guidance, review, and editing.

Appendix A

The $OC3_{LT}$ Chl-a retrieval algorithm [45] is given by (A.1). The value of x is configured with respect to the MSI sensor

$$x = log_{10}[(max[R_{rs}(443), R_{rs}(493)]) * R_{rs}(560)^{-1}]$$
$$y = a_0 + a_1 x + a_2 x^2 + a_3 x^3 + a_4 x^4$$
$$OC3_{LT} = 10^y. \tag{A.1}$$

The values of coefficients of the polynomial expression are computed by minimization of sum of Least Error Squares for each split (k-fold) using the training data only

$$Y = Xa$$
$$a = (X^T X)^{-1} X^T Y.$$

The globally trained OC3 Chl-a retrieval algorithm [45] is given by (A.1). The coefficients are adopted from the previous study [8]

$$y = 0.3308 - 2.6684x + 1.599x^2 + 0.5525x^3 - 1.4876x^4$$
$$OC3 = 10^y.$$

Appendix B

This section contain results using different settings discussed in Section IV.

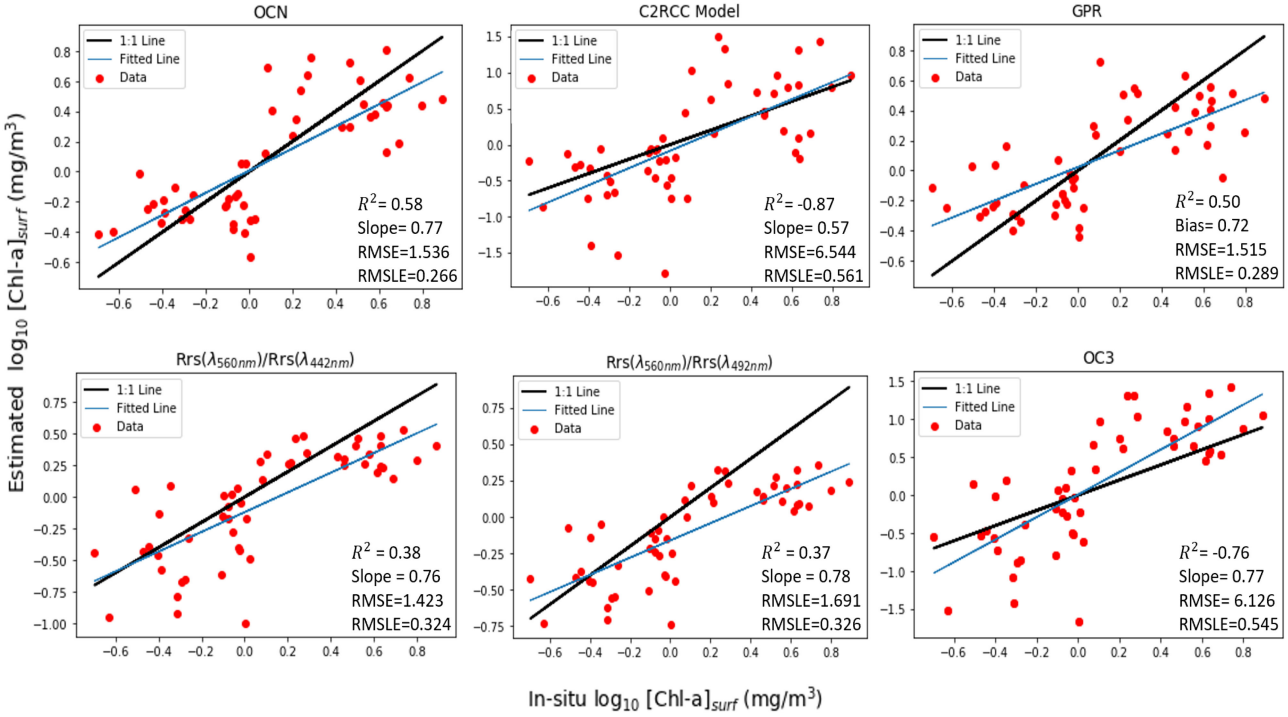

Fig. B.1. Performance evaluation of surface Chl-a retrievals using OCN, C2RCC-net, GPR, band ratios, and OC3 algorithms using one-to-one (central pixel) configuration. The total number of test samples are 52. The overall and range-specific performances are included in Table IV, respectively.

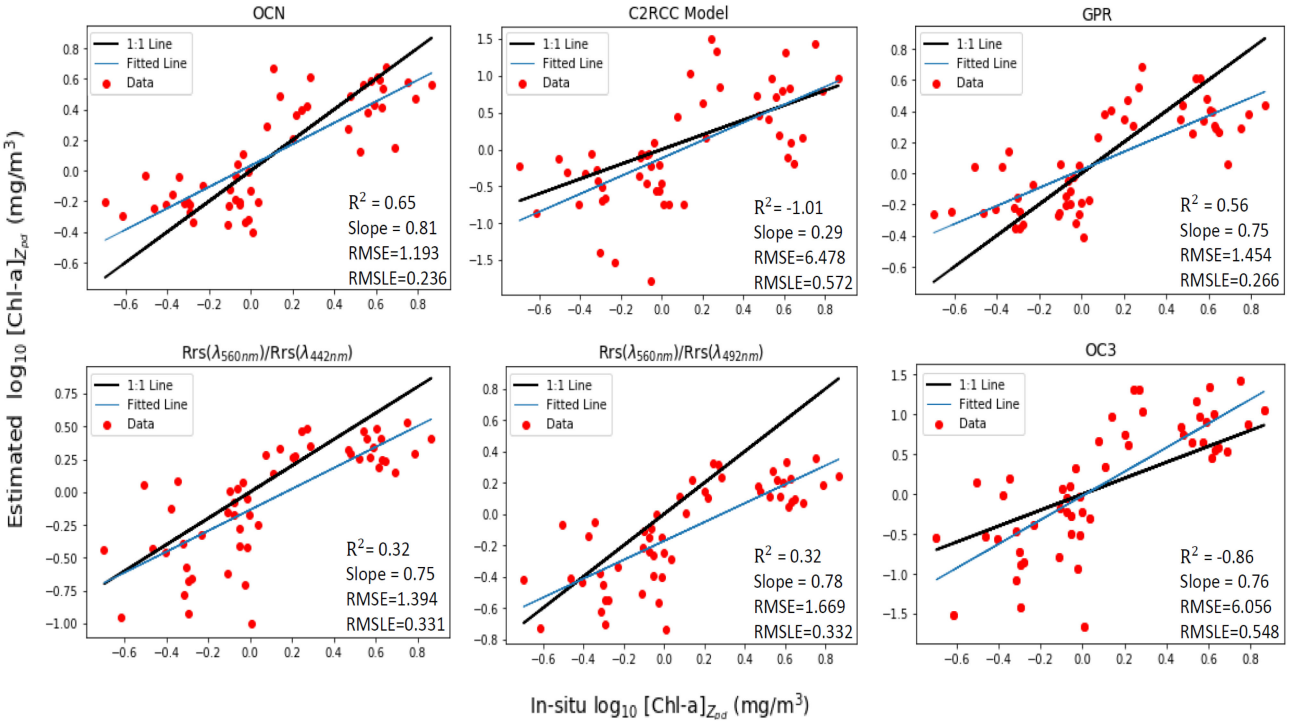

Fig. B.2. Performance evaluation of $[\text{Chl-a}]_{Zpd}$ retrievals using OCN, C2RCC-net, GPR, band ratios, and OC3 algorithms using one-to-one (central pixel) configuration. The total number of test samples are 53.

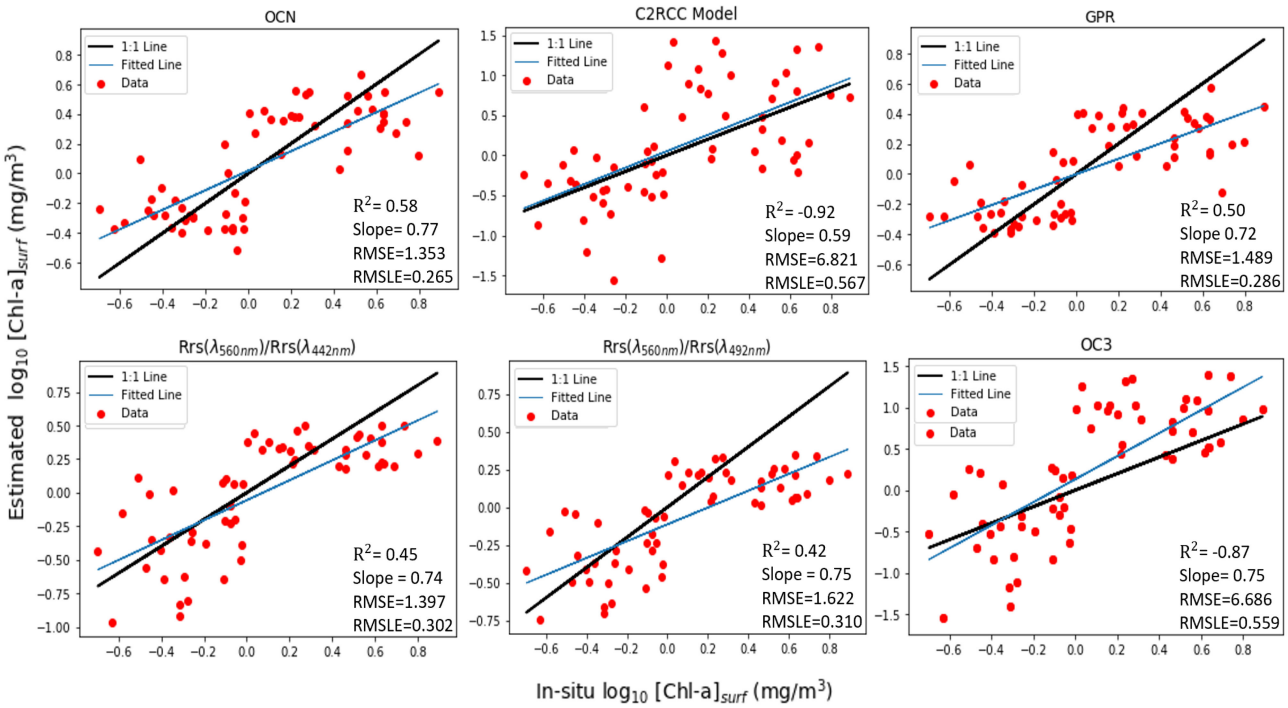

Fig. B.3. Performance evaluation of surface Chl-a retrievals using OCN, C2RCC-net, GPR, band ratios, and OC3 algorithms using one-to-one (median of 3×3 pixels) configuration. The total number of test samples are 59.

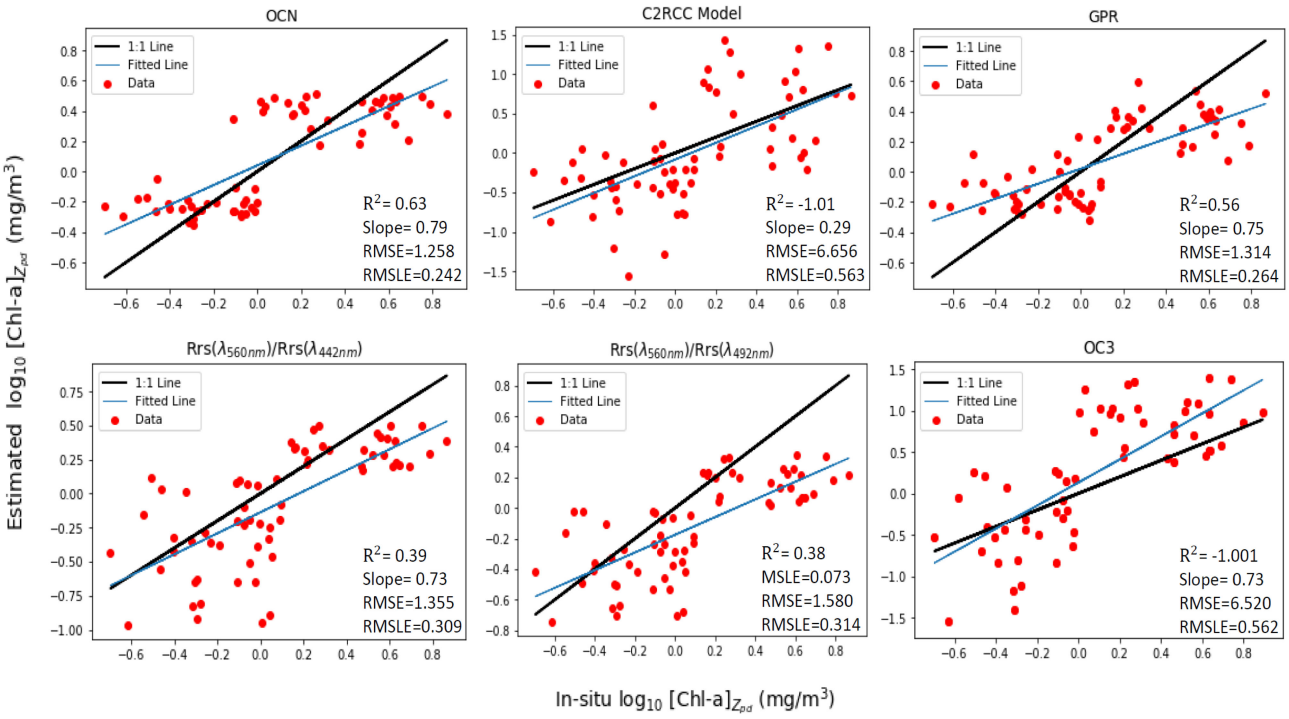

Fig. B.4. Performance evaluation of $[\text{Chl-a}]_{Zpd}$ retrievals using OCN, C2RCC-net, GPR, band ratios, and OC3 algorithms using one-to-one ((median of 3×3 pixels) configuration. The number of test samples are 62.

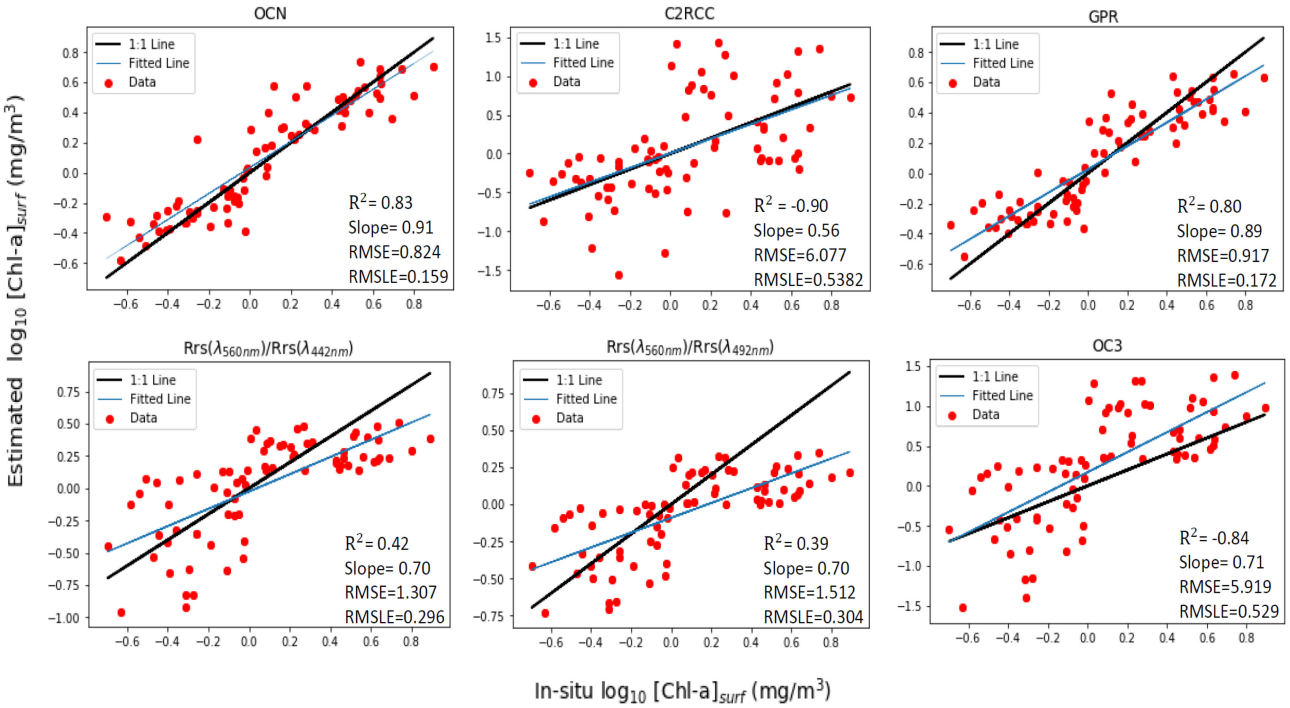

Fig. B.5. Performance evaluation of surface Chl-a retrievals using OCN, C2RCC-net, GPR, band ratios, and OC3 algorithms using one-to-window approach. The number of test samples are 75.

ACKNOWLEDGMENT

The authors would like to thank the Institute of Marine Research, Norway for providing them the *in situ* Chl-a data.

REFERENCES

[1] V. Le Fouest, C. Postlethwaite, M. A. M. Maqueda, S. Belanger, and M. Babin, "On the role of tides and strong wind events in promoting summer primary production in the Barents sea," *Continental Shelf Res.*, vol. 31, no. 17, pp. 1869–1879, 2011.

[2] H. Loeng, "Features of the physical oceanographic conditions of the Barents sea," *Polar Res.*, vol. 10, no. 1, pp. 5–18, 1991.

[3] E. Sakshaug, "Primary and secondary production in the Arctic seas," in *Proc. Organic Carbon Cycle Arctic Ocean.*, 2004, pp. 57–81.

[4] M. Årthun, T. Eldevik, L. Smedsrud, Ø. Skagseth, and R. Ingvaldsen, "Quantifying the influence of Atlantic heat on Barents sea ice variability and retreat," *J. Climate*, vol. 25, no. 13, pp. 4736–4743, 2012.

[5] T. Haug *et al.* "Future harvest of living resources in the Arctic ocean north of the Nordic and Barents seas: A review of possibilities and constraints," *Fisheries Res.*, vol. 188, pp. 38–57, 2017.

[6] P. Dalpadado *et al.*, "Climate effects on temporal and spatial dynamics of phytoplankton and zooplankton in the Barents sea," *Prog. Oceanogr.*, vol. 185, 2020, Art. no. 102320.

[7] A. Morel, H. Claustre, D. Antoine, and B. Gentili, "Natural variability of bio-optical properties in case 1 waters: Attenuation and reflectance within the visible and near-UV spectral domains, as observed in South Pacific and Mediterranean waters," *Biogeosciences*, vol. 4, no. 5, pp. 913–925, 2007.

[8] N. Pahlevan *et al.* "Seamless retrievals of chlorophyll-a from Sentinel-2 (MSI) and Sentinel-3 (OLCI) in inland and coastal waters: A machine-learning approach," *Remote Sens. Environ.*, vol. 240, 2020, Art. no. 111604.

[9] M. Asim, C. Brekke, A. Mahmood, T. Eltoft, and M. Reigstad, "Ocean color net (OCN) for the Barents sea," in *Proc. IGARSS 2020-2020 IEEE Int. Geosci. Remote Sens. Symp.*, 2020, pp. 5881–5884.

[10] C. J. Gobler, "Climate change and harmful algal blooms: Insights and perspective," *Harmful Algae*, vol. 91, 2020, Art. no. 101731.

[11] E. N. Hegseth, "Phytoplankton of the Barents sea-the end of a growth season," *Polar Biol.*, vol. 17, no. 3, pp. 235–241, 1997.

[12] H. Hodal and S. Kristiansen, "The importance of small-celled phytoplankton in spring blooms at the marginal ice zone in the northern Barents sea," *Deep Sea Res. Part II: Topical Stud. Oceanogr.*, vol. 55, no. 20-21, pp. 2176–2185, 2008.

[13] J. Holt *et al.*, "Potential impacts of climate change on the primary production of regional seas: A comparative analysis of five European seas," *Prog. Oceanogr.*, vol. 140, pp. 91–115, 2016.

[14] M. Reigstad, P. Wassmann, C. W. Riser, S. Øygarden, and F. Rey, "Variations in hydrography, nutrients and chlorophyll a in the marginal ice-zone and the central Barents sea," *J. Mar. Syst.*, vol. 38, no. 1-2, pp. 9–29, 2002.

[15] P. Wassmann *et al.*, "Food webs and carbon flux in the Barents sea," *Prog. Oceanogr.*, vol. 71, no. 2-4, pp. 232–287, 2006.

[16] O. V. Kopelevich, V. I. Burenkov, and S. V. Sheberstov, "Case studies of optical remote sensing in the Barents sea, Black sea and Caspian sea," in *Proc. Remote Sens. Eur. Seas*, 2008, pp. 53–66.

[17] O. Engelsen, E. N. Hegseth, H. Hop, E. Hansen, and S. Falk-Petersen, "Spatial variability of chlorophyll-a in the marginal ice zone of the barents sea, with relations to sea ice and oceanographic conditions," *J. Mar. Syst.*, vol. 35, no. 1/2, pp. 79–97, 2002.

[18] J. Kogeler and F. Rey, "Ocean colour and the spatial and seasonal distribution of phytoplankton in the Barents sea," *Int. J. Remote Sens.*, vol. 20, no. 7, pp. 1303–1318, 1999.

[19] K. R. Arrigo, P. A. Matrai, and G. L. Van Dijken, "Primary productivity in the Arctic ocean: Impacts of complex optical properties and subsurface chlorophyll maxima on large-scale estimates," *J. Geophysical Res.: Oceans*, vol. 116, no. C11, 2011.

[20] V. J. Hill *et al.*, "Synthesis of integrated primary production in the arctic ocean: II. In situ and remotely sensed estimates," *Prog. Oceanogr.*, vol. 110, pp. 107–125, 2013.

[21] M. Ardyna, M. Babin, M. Gosselin, E. Devred, L. Rainville, and J.-É. Tremblay, "Recent Arctic ocean sea ice loss triggers novel fall phytoplankton blooms," *Geophysical Res. Lett.*, vol. 41, no. 17, pp. 6207–6212, 2014.

[22] K. R. Arrigo and G. L. van Dijken, "Continued increases in arctic ocean primary production," *Prog. Oceanogr.*, vol. 136, pp. 60–70, 2015.

[23] I. Kostakis *et al.*, "Development of a bio-optical model for the barents sea to quantitatively link glider and satellite observations," *Philos. Trans. Roy. Soc. A*, vol. 378, no. 2181, 2020, Art. no. 20190367.

[24] L. E. Keiner and X.-H. Yan, "A neural network model for estimating sea surface chlorophyll and sediments from thematic mapper imagery," *Remote Sens. Environ.*, vol. 66, no. 2, pp. 153–165, 1998.

[25] G. Camps-Valls, L. Bruzzone, J. L. Rojo-Alvarez, and F. Melgani, "Robust support vector regression for biophysical variable estimation from remotely sensed images," *IEEE Geosci. Remote Sens. Lett.*, vol. 3, no. 3, pp. 339–343, Jul. 2006.

[26] G. Camps-Valls, L. Gómez-Chova, J. Muñoz-Marí, J. Vila-Francés, J. Amorós-López, and J. Calpe-Maravilla, "Retrieval of oceanic chlorophyll concentration with relevance vector machines," *Remote Sens. Environ.*, vol. 105, no. 1, pp. 23–33, 2006.

[27] P. M. Maier, S. Hinz, and S. Keller, "Estimation of chlorophyll a, diatoms and green algae based on hyperspectral data with machine learning approaches," *Tagungsband* der, vol. 27, pp. 49–57, 2018.

[28] L. Pasolli, F. Melgani, and E. Blanzieri, "Gaussian process regression for estimating chlorophyll concentration in subsurface waters from remote sensing data," *IEEE Geosci. Remote Sens. Lett.*, vol. 7, no. 3, pp. 464–468, Jul. 2010.

[29] K. Blix, J. Li, P. Massicotte, and A. Matsuoka, "Developing a new machine-learning algorithm for estimating chlorophyll-a concentration in optically complex waters: A case study for high northern latitude waters by using Sentinel 3 OLCI," *Remote Sens.*, vol. 11, no. 18, 2019, Art. no. 2076.

[30] S. Hafeez *et al.*, "Comparison of machine learning algorithms for retrieval of water quality indicators in case-II waters: A case study of hong kong," *Remote Sens.*, vol. 11, no. 6, pp. 617–640, 2019.

[31] J. Verrelst *et al.*, "Machine learning regression algorithms for biophysical parameter retrieval: Opportunities for Sentinel-2 and-3," *Remote Sens. Environ.*, vol. 118, pp. 127–139, 2012.

[32] J. He, Y. Chen, J. Wu, D. A. Stow, and G. Christakos, "Space-time chlorophyll-a retrieval in optically complex waters that accounts for remote sensing and modeling uncertainties and improves remote estimation accuracy," *Water Res.*, vol. 171, 2020, Art. no. 115403.

[33] J. Uitz, H. Claustre, A. Morel, and S. B. Hooker, "Vertical distribution of phytoplankton communities in open ocean: An assessment based on surface chlorophyll," *J. Geophysical Res., Oceans*, vol. 111, no. C8, 2006.

[34] L. G. Vilas, E. Spyrakos, and J. M. T. Palenzuela, "Neural network estimation of chlorophyll a from MERIS full resolution data for the coastal waters of Galician rias (*NW Spain*)," *Remote Sens. Environ.*, vol. 115, no. 2, pp. 524–535, 2011.

[35] D. Zhang, S. Lavender, J.-P. Muller, D. Walton, B. Karlson, and J. Kronsell, "Determination of phytoplankton abundances (chlorophyll-a) in the optically complex inland water-the Baltic sea," *Sci. Total Environ.*, vol. 601, pp. 1060–1074, 2017.

[36] S. W. Bailey and P. J. Werdell, "A multi-sensor approach for the on-orbit validation of ocean color satellite data products," *Remote Sens. Environ.*, vol. 102, no. 1-2, pp. 12–23, 2006.

[37] M. A. Warren *et al.*, "Assessment of atmospheric correction algorithms for the Sentinel-2A multispectral imager over coastal and inland waters," *Remote Sens. Environ.*, vol. 225, pp. 267–289, 2019.

[38] M. Pereira-Sandoval *et al.*, "Evaluation of atmospheric correction algorithms over spanish inland waters for Sentinel-2 multi spectral imagery data," *Remote Sens.*, vol. 11, no. 12, 2019, Art. no. 1469.

[39] R. Smith and K. Baker, "Oceanic chlorophyll concentrations as determined by satellite (Nimbus-7 coastal zone color scanner)," *Mar. Biol.*, vol. 66, no. 3, pp. 269–279, 1982.

[40] H. Loisel and A. Morel, "Light scattering and chlorophyll concentration in case 1 waters: A reexamination," *Limnol. Oceanogr.*, vol. 43, no. 5, pp. 847–858, 1998.

[41] H. R. Gordon, D. K. Clark, J. W. Brown, O. B. Brown, R. H. Evans, and W. W. Broenkow, "Phytoplankton pigment concentrations in the middle atlantic bight: Comparison of ship determinations and CZCS estimates," *Appl. Opt.*, vol. 22, no. 1, pp. 20–36, 1983.

[42] S. Jain and J. Miller, "Subsurface water parameters: Optimization approach to their determination from remotely sensed water color data," *Appl. Opt.*, vol. 15, no. 4, pp. 886–890, 1976.

[43] C. S. Yentsch, "The influence of phytoplankton pigments on the colour of sea water," *Deep Sea Res.* (1953), vol. 7, no. 1, pp. 1–9, 1960.

[44] J. E. O'Reilly *et al.*, "Ocean color chlorophyll algorithms for seawifs," *J. Geophysical Res., Oceans*, vol. 103, no. C11, pp. 24 937–24 953, 1998.

[45] J. E. O'Reilly and P. J. Werdell, "Chlorophyll algorithms for ocean color sensors-OC4, OC5 & OC6," *Remote Sens. Environ.*, vol. 229, pp. 32–47, 2019.

[46] G. Liu *et al.* "An OLCI-based algorithm for semi-empirically partitioning absorption coefficient and estimating chlorophyll a concentration in various turbid case-2 waters," *Remote Sens. Environ.*, vol. 239, 2020, Art. no. 111648.

[47] K. G. Ruddick, H. J. Gons, M. Rijkeboer, and G. Tilstone, "Optical remote sensing of chlorophyll a in case 2 waters by use of an adaptive two-band algorithm with optimal error properties," *Appl. Opt.*, vol. 40, no. 21, pp. 3575–3585, 2001.

[48] A. A. Gitelson *et al.*, "A simple semi-analytical model for remote estimation of chlorophyll-a in turbid waters: Validation," *Remote Sens. Environ.*, vol. 112, no. 9, pp. 3582–3593, 2008.

[49] C. Le, C. Hu, D. English, J. Cannizzaro, and C. Kovach, "Climate-driven chlorophyll-a changes in a turbid estuary: Observations from satellites and implications for management," *Remote Sens. Environ.*, vol. 130, pp. 11–24, 2013.

[50] X.-G. Xing, D.-Z. Zhao, Y.-G. Liu, J.-H. Yang, P. Xiu, and L. Wang, "An overview of remote sensing of chlorophyll fluorescence," *Ocean. Sci. J.*, vol. 42, no. 1, pp. 49–59, 2007.

[51] M. W. Matthews and D. Odermatt, "Improved algorithm for routine monitoring of cyanobacteria and eutrophication in inland and near-coastal waters," *Remote Sens. Environ.*, vol. 156, pp. 374–382, 2015.

[52] M. E. Smith, L. R. Lain, and S. Bernard, "An optimized chlorophyll a switching algorithm for meris and OLCI in phytoplankton-dominated waters," *Remote Sens. Environ.*, vol. 215, pp. 217–227, 2018.

[53] V. Piermattei *et al.*, "Cost-effective technologies to study the Arctic ocean environment," *Sensors*, vol. 18, no. 7, 2018, Art. no. 2257.

[54] Y. Fan *et al.*, "Atmospheric correction over coastal waters using multilayer neural networks," *Remote Sens. Environ.*, vol. 199, pp. 218–240, 2017.

[55] F. Pu, C. Ding, Z. Chao, Y. Yu, and X. Xu, "Water-quality classification of inland lakes using Landsat8 images by convolutional neural networks," *Remote Sens.*, vol. 11, no. 14, 2019, Art. no. 1674.

[56] J. Pyo *et al.*, "A convolutional neural network regression for quantifying cyanobacteria using hyperspectral imagery," *Remote Sens. Environ.*, vol. 233, 2019, Art. no. 111350.

[57] N. Pahlevan, S. Sarkar, B. Franz, S. Balasubramanian, and J. He, "Sentinel-2 multispectral instrument (MSI) data processing for aquatic science applications: Demonstrations and validations," *Remote Sens. Environ.*, vol. 201, pp. 47–56, 2017.

[58] Q. Wang and P. M. Atkinson, "Spatio-temporal fusion for daily Sentinel-2 images," *Remote Sens. Environ.*, vol. 204, pp. 31–42, 2018.

[59] M. Drusch *et al.*, "Sentinel-2: ESA's optical high-resolution mission for gmes operational services," *Remote Sens. Environ.*, vol. 120, pp. 25–36, 2012.

[60] R. Coluzzi, V. Imbrenda, M. Lanfredi, and T. Simoniello, "A first assessment of the Sentinel-2 level 1-C cloud mask product to support informed surface analyses," *Remote Sens. Environ.*, vol. 217, pp. 426–443, 2018.

[61] C. Kuhn *et al.*, "Performance of Landsat-8 and Sentinel-2 surface reflectance products for river remote sensing retrievals of chlorophyll-a and turbidity," *Remote Sens. Environ.*, vol. 224, pp. 104–118, 2019.

[62] X. Pan, A. Mannino, M. E. Russ, and S. B. Hooker, "Remote sensing of the absorption coefficients and chlorophyll a concentration in the united states southern middle Atlantic bight from seaWiFS and MODIS-aqua," *J. Geophysical Res.: Oceans*, vol. 113, no. C11, 2008.

[63] C. D. Mobley, *Light and Water: Radiative Transfer in Natural Waters*. New York, NY, USA: Academic Press, 1994.

[64] S. Bernard *et al.*, Earth observations in support of global water quality monitoring, SER. reports and monographs of the international ocean colour coordinating group, *Int. Ocean-Colour Coordinating Group*, Canada, vol. *IOCCG Report* 17, no. 17, 2018.

[65] A. Morel and J.-F. Berthon, "Surface pigments, algal biomass profiles, and potential production of the Euphotic layer: Relationships reinvestigated in view of remote-sensing applications," *Limnol. Oceanogr.*, vol. 34, no. 8, pp. 1545–1562, 1989.

[66] N. Almaadeed, M. Asim, S. Al-Maadeed, A. Bouridane, and A. Beghdadi, "Automatic detection and classification of audio events for road surveillance applications," *Sensors*, vol. 18, no. 6, 2018, Art. no. 1858.

[67] S. Javed *et al.*, "Cellular community detection for tissue phenotyping in colorectal cancer histology images," *Med. Image Anal.*, 2020, Art. no. 101696.

[68] S. Ioffe and C. Szegedy, "Batch normalization: Accelerating deep network training by reducing internal covariate shift," 2015, *arXiv:1502.03167*.

[69] X. Glorot and Y. Bengio, "Understanding the difficulty of training deep feedforward neural networks," in *Proc. 13th Int. Conf. Artif. Intell. Statist.*, 2010, pp. 249–256.

[70] F. Pedregosa *et al.*, "Scikit-learn: Machine learning in Python," *J. Mach. Learn. Res.*, vol. 12, pp. 2825–2830, 2011.

[71] B. N. Seegers, R. P. Stumpf, B. A. Schaeffer, K. A. Loftin, and P. J. Werdell, "Performance metrics for the assessment of satellite data products: An ocean color case study," *Opt. Exp.*, vol. 26, no. 6, pp. 7404–7422, 2018.

[72] E. Spyrakos *et al.* "Optical types of inland and coastal waters," *Limnol. Oceanogr.*, vol. 63, no. 2, pp. 846–870, 2018.
[73] J. Li and D. P. Roy, "A global analysis of Sentinel-2A, Sentinel-2B and Landsat-8 data revisit intervals and implications for terrestrial monitoring," *Remote Sens.*, vol. 9, no. 9, pp. 902–919, 2017, Art. no. 902.

Muhammad Asim received the bachelor's degree in electronics from the Department of Electrical Engineering, Comsats University, Abbottabad, Pakistan, in October 2010, and the master's degree in electrical engineering with emphases on signal processing from the Department of Electrical Engineering, Blekinge Institute of Technology, Sweden, in February 2013. He is currently working toward the Ph.D. degree in remote sensing with the Center for Integrated Remote Sensing and Forecasting for Arctic Operations (CIRFA), Department of Physics and Technology, UiT The Arctic University of Norway, Tromsø, Norway.

He worked as a Research Assistant on different projects with the Qatar University, Qatar including audio processing, biomedical signal processing, and computer vision. His research interest includes optical remote sensing of ocean areas, water quality assessment, retrieval of in-water optical properties, and machine learning.

Camilla Brekke received the Cand. Mag. (BSc) and Cand. Scient. (MSc), in informatics (computing science), and Ph.D. degrees in remote sensing and image analysis from the Department of Informatics, University of Oslo, Oslo, Norway, in 1998, 2001, and 2008, respectively.

She is a Professor with the Department of Physics and Technology, UiT The Arctic University of Norway, Tromsø, Norway. She is currently the Vice-Dean Research with Faculty of Science and Technology and Deputy Centre Leader at Centre for Integrated Remote Sensing and Forecasting for Arctic Operations. Her current research interests include synthetic aperture radar and ocean color remote sensing for Arctic and marine applications.

Arif Mahmood is a Professor with the Department of Computer Science, Information Technology University, Lahore, Pakistan. Previously he worked as Research Assistant Professor with the University of Western Australia, Crawley WA, Australia, and a PostDoc Researcher in Qatar University, Doha, Qatar. His research interests include computer vision and machine learning applications. More specifically, he has worked on moving objects detection in videos, visual object tracking, visual object categorization, nucleus detection and tissue phenotyping in cancer histology images, face detection and facial expression synthesis, action detection and recognition, visual crowd analysis, anomalous event detection, human body pose estimation, scale-able spectral clustering, community detection in complex networks, ocean color monitoring using remote sensing, and applications of machine learning in cloud and fog computing.

Torbjorn Eltoft received the M.Sc. degree in 1981 and the Ph.D. degee in 1984.

He joined the Faculty of Science and Technology, UiT the Arctic University of Norway, in 1988, where he is employed as a Professor in remote sensing at the Department of Physics and Technology. He is Director of the Centre for Integrated Remote Sensing and Forecasting for Arctic Operations (CIRFA). He has a significant publication record. His research interests include signal and image analysis, statistical modelling, and machine learning with applications in synthetic aperture radar and ocean colour remote sensing.

Dr. Eltoft and was the co-recipient of the year 2000 Outstanding Paper Award in Neural Networks awarded by IEEE Neural Networks Council, and of the Honourable Mention for the 2003 Pattern Recognition Journal Best Paper Award. He was the recipient of the " UiT Award for Research and Development" in 2017. He served as an Associate Editor for the Elsevier journal *Pattern Recognition* for the period 2005–2011, and was Guest-Editor for the journal *Remote Sensing* on the Special Issue for the PolInSAR 2017 conference.

Marit Reigstad received the master's degree in marine zoology 1994, and her Ph.D. in marine biology in 2000.

She is a Field Biologist, and enjoys interdisciplinary collaboration. She has participated, initiated, and lead several Arctic marine research projects, and is now leading the Norwegian collaborative research project The Nansen Legacy. This project aims to build a multidisciplinary knowledge basis for the changing Arctic marine region in the northern Barents Sea and adjacent Arctic Ocean. The Nansen Legacy includes ten institutions and more than 150 scientists focusing on the eco-and climate system of the Northern Barents Sea and adjacent Arctic Ocean. She is a Professor in marine ecology with the UiT, since 2009. She teaches ecology and marine systems, including supervision on Master, Ph.D. and Post doc level. She has also been involved in developing the Norwegian strategy for the Decade of ocean science for sustainability. She has authored or coauthored 71 peer-reviewed papers. Her research interests includes productivity, plankton and their fate in marine ecosystems, with a special interest for vertical flux and for ice-impacted areas.

Dr. Reigstad was a Guest Editor for the special issue *CarbonBridge* to the Arctic in Frontiers of Marine Science, 2020. She has been involved in international science planning, since 2011. She serves at the Board of Tromsø Forskningsstiftelse, the Scientific Liason Panel of the EU project ARICE, and the scientific advisory board of Chinese-Norwegian research project STRESSOR .

8

Paper II: A new spectral harmonization algorithm for Landsat-8 and Sentinel-2 remote sensing reflectance products using machine learning: a case study for the Barents Sea (European)

9

Paper III: Spectral harmonization of Landsat-8 and Sentinel-2 remote sensing reflectance products for mapping Chlorophyll-a and CDOM in coastal and inland waters

Spectral harmonization of Landsat-8 and Sentinel-2 remote sensing reflectance products for mapping Chlorophyll-a and CDOM in coastal and inland waters

Muhammad Asim, Atsushi Matsuoka, Sidrah Hafeez, Torbjørn Eltoft, Member IEEE, and Katalin Blix

***Abstract*—Combining data products from Sentinel-2 Multispectral Imager (MSI) and Landsat-8 Operational Land Imager (OLI) can provide an excellent opportunity to improve the temporal resolution of time series, increase match-ups with in-situ observations, and thus improve the monitoring of water quality over coastal and inland waters. The current study aims to harmonize OLI and MSI aquatic remote sensing reflectance (ρ_w) products in order to obtain more match-ups (OLI and MSI combined) and, as a result, better optimize the regression models to accurately retrieve Chlorophyll-a (Chl-a) and color dissolved organic matter (CDOM) concentrations in global coastal, and inland waters. To harmonize OLI-MSI ρ_w products, first, we evaluate the performance of atmospheric correction (AC) models such as Acolite, Polymer, C2RCC, OC-SMART, and ICOR against the in-situ ρ_w. Results suggest that the OC-SMART-derived ρ_w products are in good agreement with in-situ observations with a median absolute percentage difference (MAPD) $< 30\%$ across all the visible bands of OLI and MSI. To spectrally merge OLI and MSI, we apply a new machine learning(ML)-based bandpass adjustment (BA) model [1] to near-simultaneous OLI and MSI images acquired in the year 2021. We demonstrate that after BA, the averaged spectral differences are significantly reduced from 21% to $< 5\%$ in the common bands of OLI and MSI. The weights and bias terms optimized during the transformation from MSI to OLI-derived ρ_w are then used to BA MSI-derived ρ_w products. The OLI and BA MSI (MSI*)-derived ρ_w products are then combined in a single dataset for training and validation of the Chl-a and CDOM retrieval algorithms including the previously developed ocean color net (OCN) [2], Gaussian Process Regression (GPR) and the three-band ratio based algorithm (OC3). Chl-a retrievals indicate that using the proposed OLI-MSI* ρ_w data improved the performance of the OCN by 41%, GPR by 21% and the OC3 by 27% in terms of mean absolute error compared to the OLI ρ_w data. Similarly, all the algorithms yielded a reduced root mean square difference in CDOM retrievals using the purposed OLI-MSI* data.**

***Index Terms*—Ocean Color, Spectral harmonization, Band adjustment, Machine Learning, Water quality.**

I. Introduction

RELIABLE estimation of global water quality indicators (WQIs) products plays a critical role in understanding the dynamic nature of aquatic ecosystems. Due to climate change and ever-increasing human activities, coastal and inland waters are facing significant changes [3]. These alterations are evident in the form of periodic occurrences of harmful algal blooms (HABs) that pose major threats to global water security [4]. Therefore, effective and continuous monitoring of these natural resources is of significant importance to ensuring the environmental health and sustainability of aquatic ecosystems [5]. Traditional point-based or section-based sampling methods of monitoring these resources are expensive and time-consuming. Alternatively, remote sensing techniques can be used to monitor the WQ from space. However, due to the dynamic nature of aquatic systems especially, inland and coastal waters, where high spatial and temporal variability may exists in concentrations of in-water constituents such as Chlorophyll-a (Chl-a), remote sensing of these optically complicated water resources require frequent observations (e.g., daily) at a high spatial resolution [5], [6].

Most of the existing ocean color (OC) satellites with high temporal resolution have a coarse spatial resolution of $\geq$ 300 m, not suitable for detecting fine features in natural waters, especially in small lakes, rivers, and inland waters [7], [8]. Contrarily, high spatial resolution satellite sensors, such as the Operational Land Imager (OLI) onboard Landsat-8/9 with a spatial resolution of 30 m and the Multispectral Imager (MSI) aboard Sentinel-2A/2B with 10-20-60 m spatial resolution, have considerable potential for monitoring optically significant water quality indicators (WQIs) with more spatial-detailed information not feasible with other OC satellites. These sensors, however, have low-frequency revisit times of 16 and 5 days. In addition, frequent cloud coverage may mask the desired information which further reduces the frequency of OC observations. Thus, the longer revisit time makes them insufficient for near-daily monitoring of water surface [7]. The similar band design of OLI and MSI sensors makes it possible to combine their imagery with a global median average revisit interval of ~2.9 days at a spatial resolution of 10-60 m [9]. Considering cloud coverage, such frequent revisit times are essential to capture the biogeochemical variations in dynamic coastal and inland waters [5]. This work is focused on harmonizing OLI and MSI radiometric data to increase the frequency of OC observations, increase the number of training examples, and, hence, improve the performance of

M. Asim, K. Blix, T. Eltoft are with the Department of Physics and Technology, UiT The Arctic University of Norway (UiT), Tromsø, Norway, e-mails: {muhammad.asim, camilla.brekke, torbjørn.eltoft}@uit.no.

A. Matsuoka is with the Institute for the Study of Earth, Oceans, and Space, University of New Hampshire, Durham, NH, 03824, USA, e-mail: {atsushi.matsuoka}@unh.edu.

WQ retrieval algorithms.

Several studies have demonstrated the utility of these sensors for WQ monitoring utilizing OLI or MSI images alone [2], [10]–[13], but quite a few have used combined OLI-MSI data products for a similar application [4], [5], [9], [14]–[19]. Using combined OLI-MSI imagery, the literature studies can be classified into two categories, i) comparing the performance of OLI and MSI in retrieving optically significant WQIs [4], [14], [15] and ii) evaluating the consistency in OLI-MSI derived data products to generate harmonized OLI-MSI products [5], [9], [16]–[19]. The studies found in the first category have evaluated the performance of OLI and MSI-derived remote sensing reflectance (R_{rs}) or aquatic remote sensing reflectance (rho_w) individually in estimating WQIs, whereas the latter demonstrate the utility of these sensors for improved temporal coverage by their combined use.

In the first category, Watanabe et al. evaluated the performance of OLI and MSI sensors using empirical algorithms for retrieving Chl-a concentrations in a hyper-eutrophic reservoir in Brazil [14]. Due to the presence of additional NIR bands in MSI, they achieved better results compared to OLI. A machine learning (ML)-based algorithm, Mixture Density Network (MDN), was demonstrated to outperform band ratio algorithms in retrieving Chl-a using images from different sensors acquired over inland and coastal waters around the globe [4]. Similarly, with a goal of producing consistent multi-mission global WQIs, the authors in [15] demonstrated the effectiveness of MDN for simultaneous retrieval of Chl-a, color dissolved organic matter (CDOM) and total suspended matter (TSM) from the OLI, MSI, and Sentinel-3 Ocean and Land Colour Instrument (OLCI) images.

In the second category, Kuhn et al. examined the influence of uncertainties in atmospheric correction (AC) on the performance of standard bio-optical algorithms for Chl-a and turbidity from OLI and MSI images [18]. Similarly, Page et al. used MSI and OLI images for mapping water clarity in several optically variable lake systems around the USA [16]. They concluded that the uncertainties in AC play a crucial role in the data consistency between these sensors. Chen et al. reported good consistency in estimating dissolved organic carbon (DOC) concentrations from OLI and MSI using empirical methods based on the band ratio of red and green bands. Their results illustrate that the combined use of these sensors can improve the OC observation frequency. OLI-MSI time series data were used for several terrestrial-monitoring applications in [9]. Similarly, Pahlavan et al. evaluated the spectral consistency between near-simultaneous OLI-MSI derived downstream OC products [5]. They concluded that OLI-MSI R_{rs} products are consistent within 6% and emphasized generating seamless data products record from combined OLI and MSI images.

In the aforementioned studies, researchers have either retrieved the WQIs from OLI and MSI-derived ρ_w products alone or compared their respective data products from near-simultaneous OLI-MSI images. In regards to harmonized OLI-MSI data products, despite their high data consistency reported in previous studies [1], [5], [20], as per our knowledge, no effort has been made on demonstrating the suitability of combined OLI-MSI ρ_w data for the simultaneous retrieval of downstream data products such as Chl-a and CDOM. As per our knowledge, this study is the first attempt to develop a single model based on neural networks (NNs) to estimate WQIs from combined MSI and OLI imagery. Combining OLI-MSI ρ_w products into a single dataset increases the number of training examples and improves the optimization of the retrieval models. The WQIs considered in this study include Chl-a, a proxy for phytoplankton biomass, and CDOM, measured as CDOM absorption at 440 nm ($a_{cdom}(440)$).

OC remote sensing algorithms require robust AC for the accurate retrieval of WQIs [21]. While AC schemes for water applications have existed for decades, yet they are not perfect. Currently, there is no AC algorithm that can generate seamless estimates of WQIs from OLI and MSI images [4]. Although Landsat-8 OLI and Sentinel-2 MSI have similar band designs, they are not strictly identical. These sensors have a different spatial resolution, the field of view, spectral bandwidth, and spectral response functions (SRFs) [6], [22]. In addition, different illumination and acquisition conditions as well as variations in the atmospheric conditions further increase the differences in the atmospherically corrected OLI-MSI ρ_w products. These differences in ρ_w estimates lead to inconsistencies in downstream products such as Chl-a and CDOM [23]. Therefore, AC plays a critical role in the combined use of these sensors.

To account for the differences in the atmospherically corrected OLI-MSI derived ρ_w products, most of the studies have either used linear regression and least squares regression models for spectral bandpass adjustment [6], [7], [20], [22]. Some studies have evaluated the spectral differences between their respective ρ_w products without validating against the in-situ ρ_w data [20], [24]–[27]. Lack of validation against the ground truth leads to uncertainties in satellite-derived ρ_w estimates, which in turn affect the retrieval of WQIs [28].

Different from the previous studies, the present study combined the OLI and MSI data into a single dataset using a three-step approach: i) we evaluate the performance of five state-of-the-art AC models, C2RCC [29], Acolite [30], Polymer [31], ICOR validated in [28] and OC-SMART [32] against above water in-situ ρ_w observations. The aforementioned step ensures realistic ρ_w estimates from satellite images for the study sites, ii) the top-performing AC scheme was then selected to estimate ρ_w products from near-simultaneous OLI and MSI images. Instead of fitting the transformation coefficients of a linear regression model, we applied the ML-based bandpass adjustment (BA) model proposed in [1] for spectral alignment of OLI-MSI ρ_w products for Arctic waters , iii) the wights and bias terms optimized during the transformation of MSI-derived ρ_w to that of OLI-derived ρ_w products were applied to the MSI-ρ_w products. This step transforms MSI-ρ_w data to the spectral domain of OLI and serves as the correction factor for merging OLI-

MSI $_w$ products. After integration of OLI-ρ_w and MSI*ρ_w products, the OCN model [2] was trained to estimate Chl-a and CDOM concentrations from combined OLI-MSI dataset. As per our knowledge, no such study has been conducted to estimate Chl-a and CDOM from combined OLI-MSI* images using a single retrieval model for different aquatic environments. A flowchart of the work is shown in Fig. 1.

The major contributions of the present study are as follow.

- Performance evaluation of five state-of-the-art AC methods against in-situ ρ_w using OLI and MSI images acquired over different optical regimes.
- We evaluate the performance of the BA model developed for Arctic waters in [1] for merging OLI and MSI ρ_w data products over different optically complex water types.
- We evaluate the performance of different WQ retrieval algorithms for estimating Chl-a and CDOM from OLI-ρ_w and MSI*ρ_w data.

This paper is organized as follows: Section II presents information on the material and satellite data acquisitions. Section III is devoted to the main methodology, the proposed spectral BA method, whereas the experimental results are discussed in section IV. Finally, conclusions are drawn in section V.

II. Data and pre-processing

A. Satellite data

In this study, imagery from Operational Land Imager (OLI) onboard Landsat-8 (L8) satellite and Multispectral Instrument (MSI) onboard Sentinel-2 A/B is used in three major experiments, as illustrated in Fig. 1. i) comparison of atmospherically corrected OLI-MSI ρ products with in-situ observations (match-ups; see Section III-B for details); ii) spectral harmonization of OLI-MSI data (inter-comparisons; see Section III-C for details); and iii) optimization of the WQ retrieval algorithms using the same match-up dataset described in Section III-B. Note that the OLI-MSI match-ups (matching in-situ data to satellite-derived data) obtained in Section III-B are used for the estimation of Chl-a and CDOM.

B. In-situ data

1) Radiometric observations: The in-situ radiometric measurements were acquired in a various water types, from oceanic to very turbid and absorbing environments from the year 2011 to 2017 (see Fig. 2). The measurement protocols and quality control procedures to collect the radiometric data are documented in [33]. Briefly, the in-situ data were collected using a compact optical profiling system (C-OPS) [34]. The optical data and all profiles in inland waters (the majority of the data) were measured using the Compact-Propulsion Option for profiling Systems (C-PrOPS) accessory in conjunction with the C-OPS hydrobaric buoyancy system. In total, 25 field campaigns were conducted, spanning the years 2013–2017, covering 318 stations with at least three consecutive castings at each station [33], [35].

The radiometric quantity utilized in this study is the in-situ aquatic reflectance (ρ_w) defined as:

$$\rho_w(z,\lambda) = \pi \times \frac{L_u(z,\lambda)}{E_d(z,\lambda)} = \pi \times R_{rs} \tag{1}$$

where $L_u(z,\lambda)$ and $E_d(z,\lambda)$ represent the up-welling radiance and downwelling irradiance measured simultaneously at 19 wavebands between 320 and 875 nm. Here, z and λ represent depth and wavelength respectively. More details are listed in [35].

2) Chl-a and CDOM: Along with the radiometric observations, the Chl-a (mg m^3) and the CDOM absorption coefficient ($a_{cdom}(\lambda)$, m^{-1}) from near water surface were also obtained simultaneously. Duplicate or triplicate water samples were collected at each station as explained in detail by [33]. The Chl-a data were obtained systematically using the high-performance liquid chromatography (HPLC) method following SeaHARRE protocols ([36]). The $a_{cdom}(440)$ measurements were estimated with a spectrophotometer or UltraPathliquid waveguide [33].

III. Methods

A. AC methods

The total received signal at TOA received by satellite sensor (L_t) can be partitioned linearly into contributions from different radiometric components [37].

$$L_t = L_r(\lambda) + L_a(\lambda) + L_{ra}(\lambda) + tL_w(\lambda) \tag{2}$$

These components include L_r which represents Rayleigh scattering by air molecules in the absence of aerosols, L_a is the radiance from the result of scattering due to aerosols in the absence of air molecules, L_{ra} is the interaction between molecules and aerosols, t is diffuse transmission; and L_w is the water leaving radiance which can be converted in ρ_w using methodology defined in [38].

The purpose of AC is to accurately retrieve ρ_w from L_t. Once accurately retrieved, ρ_w can be mapped into WQIs using the retrieval models [39].

In this study we have evaluated the performance of five state-of-the-art AC processors, i.e., C2RCC v1.0 [29], Polymer v4.13 [31], Acolite python version version 20211124.0 [30], [40], ICOR validated in [28] and OC-SMART [32] for comparison of satellite derived ρ_w with in-situ ρ_w observations (section III-B). Several studies have used these AC schemes for processing OLI and MSI imagery and achieved reasonable success over different water types [3], [18], [28], [41], [42]. Yet their performances have not been evaluated for spectral harmonization of OLI-MSI ρ_w products and estimation of WQI using the harmonized ρ_w products. Notably, despite years of study in the field of OC remote sensing, there is yet no optimal AC approach that can provide seamless Chl-a from these sensors.

Note that, in this study, bidirectional water correction was applied to in-situ and satellite-derived ρ_w data retrieved

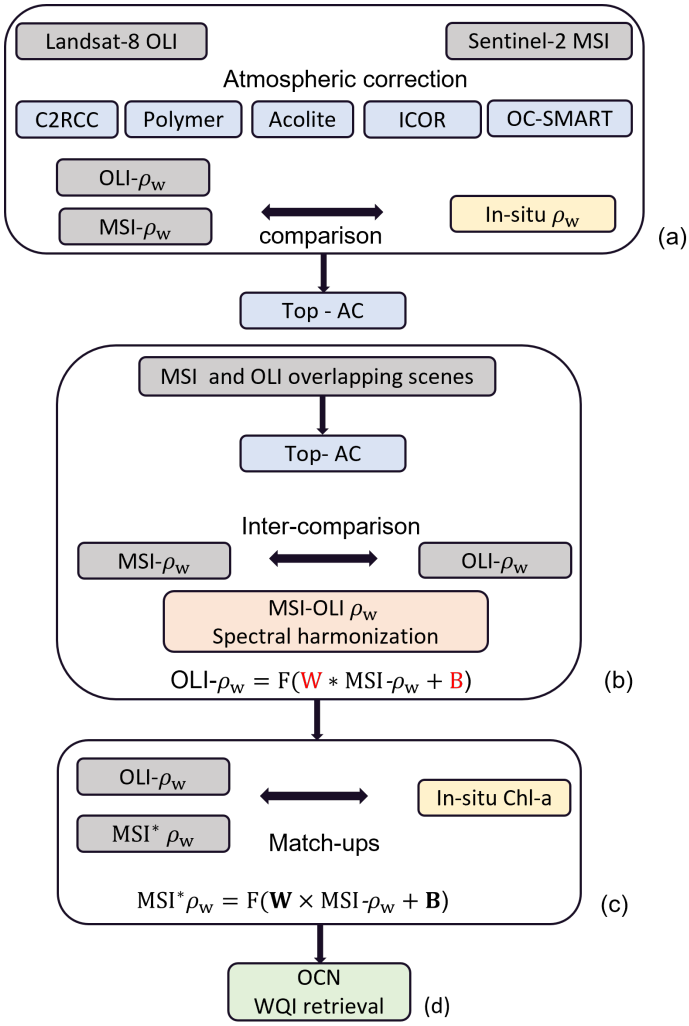

Fig. 1: Flow chart of the proposed methodology. a) Acquisition of OLI-MSI scenes corresponding to in-situ data (match-ups). Validation of AC schemes against the in-situ ρ_w. b) The AC scheme in agreement with in-situ ρ_w is selected to process near-simultaneous OLI-MSI images acquired at TOA with the spatially overlapping regions of interest. The MSI ρ_w products are bandpass adjusted to that of OLI ρ_w products. c) The optimized weights and biases, W and B, during step (b) serve as a correction factor to transform MSI-derived ρ_w to that of OLI-derived ρ_w. d) The match-up dataset (in-situ WQIs and OLI-MSI* ρ_w products) are used to train the OCN model. The trained OCN model is then demonstrated to map OLI and MSI* ρ_w products to concentrations of Chl-a and CDOM.

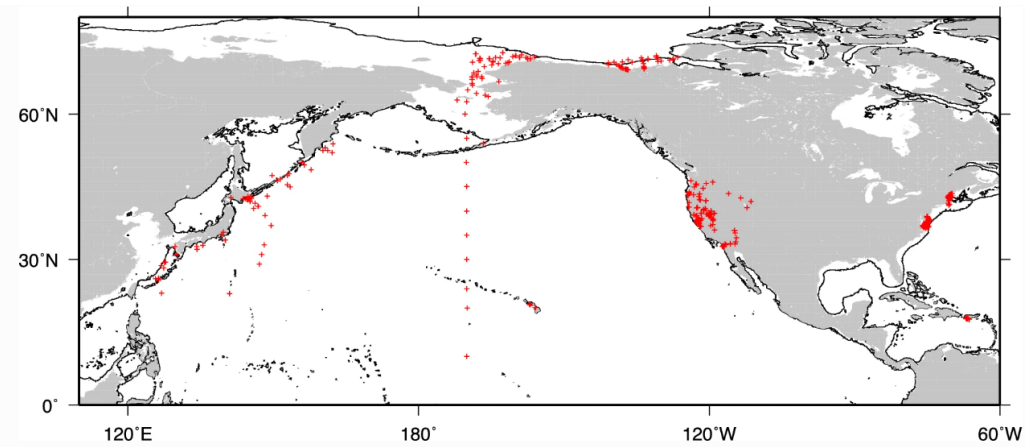

Fig. 2: Geographic locations of the sampling stations [35].

via Polymer, OC-SMART, and C2RCC. The present versions of the Acolite DSF and ICOR schemes do not correct for bidirectional effects.

B. Match-up selection

For match-up selection, matching in-situ data products with satellite-derived products, we permitted a time window of ±3 hours for coastal waters [28] and same-day overpasses (both OLI and MSI) for inland waters [3], [15], [28], of the in-situ observations. Note that these match-ups were used to validate the performance of AC followed by the retrieval of WQIs (see section III-D).

The ρ_w data were computed over a 3×3 pixels window centered around the in-situ location [39]. A median ρ_w estimate that passed the quality flags of the AC scheme was used as a match-up value. To remove the pixels affected by cloud cover, land, and sun glint, we used AC pixel quality flags in their default settings. The ρ_w pixels within the window were discarded if pixel values were ≥ 1 or negative at any wavelength [3]. In addition, a window was excluded if the number of non-masked ρ_w pixels were < 5 or coefficient of variation (CV) > 0.15 [39].

As each individual AC scheme has different masking criteria, after matching in-situ ρ_w measurements with satellite-derived ρ_w data, we extracted 25 match-up pixels for Acolite, 26 for C2RCC, 47 for Polymer, 40 for OC-SMART and 34 for ICOR, respectively. Note that a large portion of our in-situ observations were collected from narrow lakes and nearshore coastal waters, making it challenging to obtain enough match-ups. More than half of the overlapping satellite images, both OLI and MSI were discarded due to high adjacency due to land and sun-glint.

C. Spectral harmonization of OLI-MSI ρ_w

This section is dedicated to the spectral harmonization of OLI-MSI ρ_w products. In the following section, we explain the criteria for inter-comparisons, followed by BA of MSI-derived ρ_w products to combine OLI and MSI-ρ_w products into a single match-up dataset that will be used to tune the retrieval models to estimate Chl-a and CDOM in section III-D. Note that, as illustrated in Fig. 1, the main purpose of spectral harmonization (the transformation of MSI into OLI-derived ρ_w) is to optimize the weights and bias terms of the BA model (see Fig. 1 (c)) on a larger dataset to transform MSI-ρ_w data into those of OLI.

1) Inter-comparisons selection: For the OLI and MSI inter-comparisons, we permit a time difference of ±30 minutes with low to no cloud cover. In addition, scenes with low aerosol loading are considered in this study. Limiting the spectral inter-comparisons to ±30 minutes difference ensures similar atmospheric and aquatic conditions, while low aerosol loading indicates near-ideal environmental conditions. Under these conditions, discrepancies in data products can, to a large extent, be attributed to differences in the absolute radiometric responses of OLI and MSI [5]. Our analysis covers different environmental and aquatic conditions, covering both bloom and non-bloom conditions in open oceanic, coastal, and inland waters.

The n-SNO overpasses were selected automatically using the metadata files, allowing a time difference of ±30 mins between the overpasses with low or no cloud cover. To ensure low aerosol loading, spectral pixels were excluded from inter-comparison if the median value over the OC-SMART estimated aerosol optical thickness (AOT) product, i.e., AOT-550 in a window of 6×6 and 3×3 pixels for OLI and MSI images, exceeds 0.5. A median ρ_w value over non-masked 6×6 and 3×3 pixels window was estimated from 30 m OLI, and 60 m re-sampled MSI images respectively, to eliminate outliers and artifacts from our analysis [1]. To ensure spatial homogeneity, ρ_w window was excluded from inter-comparisons if the CV across the window (OLI or MSI) was greater than 50%. Note that our dataset covers different water types, oceanic or highly absorbing waters, therefore, we did not apply any restriction of the magnitude of ρ_w values. However, to avoid over-correction by AC processors, the negative ρ_w retrievals across the window were excluded. Similar to studies [5], [6], we have considered the common bands in both sensors, i.e., coastal aerosol, blue, green, and red bands. In the absence of global in-situ data for validation of remotely sensed data products, one of the sensors has to be considered a reference for performance evaluation [25]. Due to the improved radiometric calibration [43] and high signal-to-noise ratio (SNR) of OLI [44], in this study the OLI-derived ρ_w products are considered as the reference to adjust MSI-derived ρ_w products [6].

2) MSI reflectance adjustment: The MSI-derived ρ_w are adjusted to that of OLI using the BA model proposed in [2] for Arctic waters. Briefly, the BA model is based on NNs and tuned to transform MSI-derived ρ_w products to that of OLI-derived ρ_w products. The transformation from MSI to OLI-derived ρ_w products is done pixel by pixel. The tuned weight and bias terms obtained during the training process are then used to adjust MSI-derived ρ_w data (see Fig. 1 (c)). The architecture and experimental setup for validating the BA model are detailed in [1]. Briefly, the inter-comparisons were randomly split into 80% training and 20% test data using 5-fold cross-validation.

D. Water constituent retrieval

1) Retrieval models: For the estimation of Chl-a and CDOM, in this study, we have compared the performance of two sets of algorithms, namely the ML and band ratio-based algorithms. In the ML-based models, we have employed the recently developed OCN [2] based on NNs and the Gaussian process Regression (GPR) [10], [45]. Note that the OC-SMART does not retrieve ρ_w in the NIR band, therefore, we have only used the type-1 OC algorithm (OC3) [46] that utilizes the visible bands for retrievals) for Chl-a retrievals. Type-II algorithms (that require both visible and NIR bands) are only applicable for Chl-a retrievals from MSI matchups. Due to the small number of MSI match-ups (N=10), we have used the bands common in OLI and MSI. For CDOM retrievals, we have implemented the band ratio-based exponential algorithm proposed in [47].

2) Chl-a and CDOM match-ups with satellite data: The performance of these algorithms is evaluated in three different settings, i.e., the algorithms are trained and tested on Chl-a and CDOM match-ups with i) OLI ρ_w products alone (setting I), ii) combined OLI-MSI ρ_w (setting II) and ii) combined OLI-MSI* ρ_w (setting III).

3) Experimental setup: The match-ups were randomly divided into 90% training and 10% test samples using 10-fold cross-validation in order to assess the performance of the OCN. Each split's training samples were further split into training (80%) and validation (20%) samples. The OCN model was trained for 3000 epochs in each split using the training data only. In order to prevent over-fitting and better tuning of the hyper-parameters, during the training phase, the OCN model with weights and bias terms with a minimum validation error was used to estimate Chl-a and CDOM on the unseen data. The GPR and band ratio-based models are trained and validated using the same samples. More details about optimizing the parameters of the GPR model are provided in [2], [45]. The band ratio-based algorithms for Chl-a (OC3) and CDOM (exponential model) retrievals were locally tuned by combining training and validation splits. The formulations for the retrieval algorithms are provided in Appendix A.

4) Evaluation Metrics: We used the median absolute percentage difference (MAPD), the median relative percentage difference (MRPD), the root mean square difference (RMSD), the root mean square difference in log scale (RMSLD), and the coefficient of determination (R^2) to compute the differences between the in-situ and OLI-MSI derived ρ_w or WQIS. The evaluation metrics are represented by Eqs.(3), (4),(5), (6), and (7), respectively.

$$MAPD = 100\% \times median\left(\frac{|X_i - Y_i|}{|Y_i|}\right) \tag{3}$$

$$MRPD = 100\% \times median\left(\frac{X_i - Y_i}{Y_i}\right) \tag{4}$$

$$RMSD = \sqrt{\frac{1}{N_t}\sum_{i=1}^{N_t}(X_i - Y_i)^2} \tag{5}$$

$$RMSLD = \sqrt{\frac{1}{N_t}\sum_{i=1}^{N_t}\left(\log_{10}(X_i) - \log_{10}(Y_i)\right)^2} \tag{6}$$

$$R^2 = 1 - \frac{\sqrt{\sum_{i=1}^{N_t}(Y_i - X_i)^2}}{\sqrt{\sum_{i=1}^{N_t}(Y_i - \bar{X})^2}} \tag{7}$$

where X_i represents satellite derived ρ_w (section IV-A), MSI derived ρ_w products (sections IV-B) or estimated Chl-a or CDOM concentrations (sections IV-C). Y_i represents in-situ ρ_w, Chl-a and CDOM, or OLI-derived ρ_w products (IV-B). Here, N_t, indicates the number of test samples.

IV. Results and Discussion

A. Match-up analysis

This section validates the performance of Acolite, C2RCC, ICOR, Polymer, and OC-SMART against the in-situ ρ_w. The performance analysis of AC processors is described in two settings: i) performance evaluation of each processor individually against the in-situ ρ_w using all the valid match-ups; ii) an assessment of common valid match-ups between processors. The latter offers a fair performance evaluation using identical match-ups (valid water pixels), while the former assesses their practicality, including the masking of non-water pixels and erroneous non-water pixels.

The scatter plots in Fig. 3 and the statistical metrics in Table. I provide a straightforward and qualitative assessment of individual performance for combined OLI and MSI data. Our analysis illustrates that all the processors have shown band-dependent performance. For instance, Polymer with MAPD=13.9% performed better in the blue band, while Acolite in the green band with MAPD=10.5% and OC-SMART with MAPD=13.8% in the red band. All the AC processors have yielded over/underestimated ρ_w products in the coastal aerosol band with MAPD > 28%. Overall, all the processors have exhibited superior performance in the green and red bands and worse in the coastal aerosol band. This may be partially attributed to the higher signal level in the green and red region of the ρ_w spectrum for the majority of our data.

Although the AC processors yield different numbers of match-ups (see Table. I), similarities and differences among the AC processors can further be highlighted. For instance, C2RCC, Polymer, ICOR, OC-SMART (except in the red band) have underestimated the ρ_w products, whereas, Acolite has shown positive bias irrespective of the wavelength. In the 443 nm band, Acolite overestimate (MRPD=22%); whereas, C2RCC, Polymer and OC-SMART have underestimated the ρ_w products. The highest negative bias is observed in the C2RCC estimates with MRPD=-20% while the minimum is in Polymer estimates, followed by ICOR. Similar distributions appear to exhibit in the 492 nm band; however, all the processors have shown improved performances compared to the 443 nm band except ICOR. In the green band, considerable improvement is observed in the estimates of all the processors. Acolite exhibits top performance with MAPD and RMSLD of 10.5% and 0.10 sr^{-1}, which is the minimum error reported for our dataset. In the 665 nm band, OC-SMART estimates have minimum difference from the in-situ observations followed by ICOR. Acolite overestimates with an MRPD=42.9%; almost all the estimates are above the 1:1 line. C2RCC underestimate the high ρ_w values (~> 0.025) with the highest RMSLD=0.60 sr^{-1} reported in our dataset. Compared to the other bands, Polymer has shown worse performance in the red band with MAPD> 35%; whereas ICOR retrievals have shown minimum error with MAPD=21.8%.

Overall, individual performance evaluation of the five AC processors shows that OC-SMART is the top performer with MAPD < 30% across all the visible bands. To answer

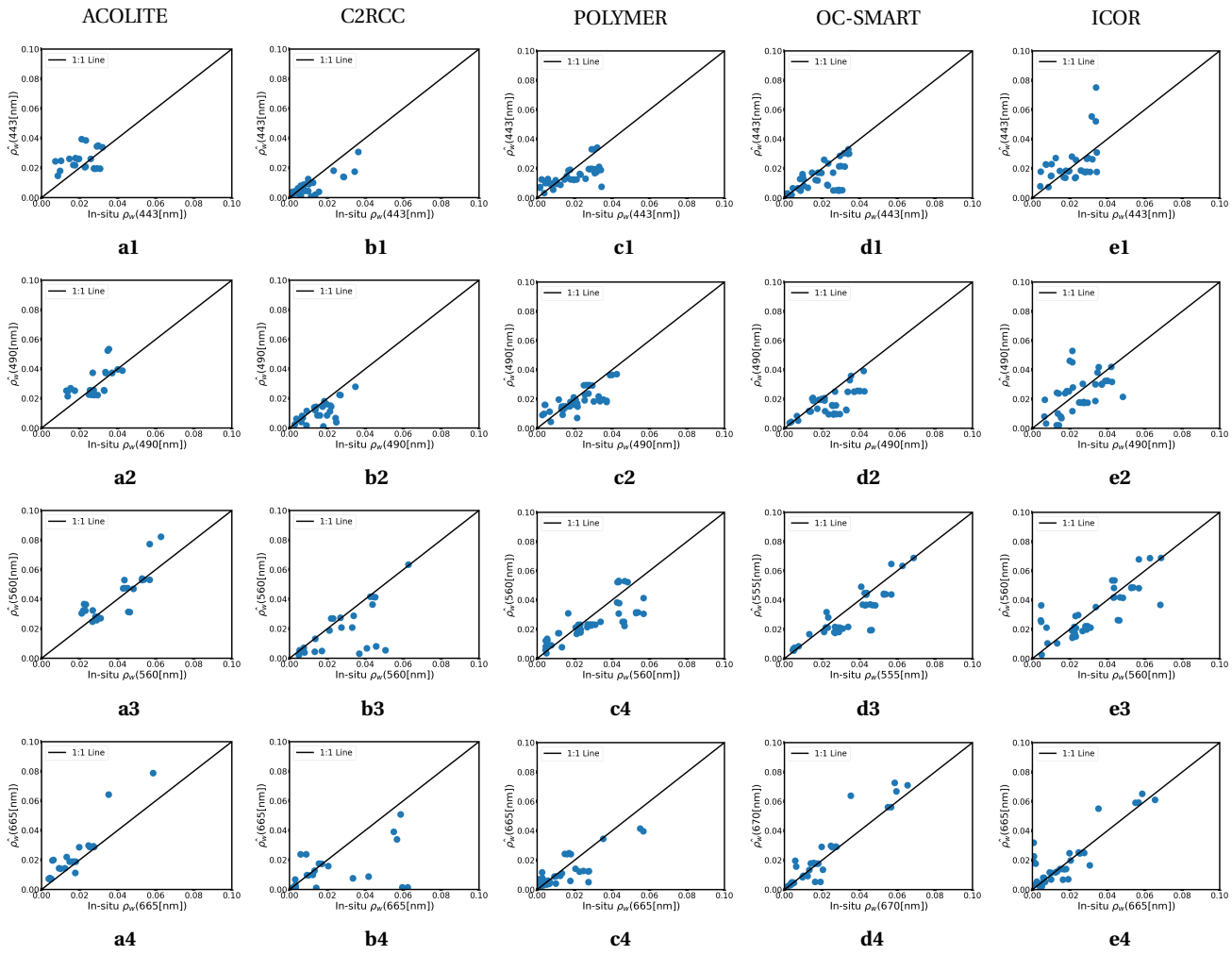

Fig. 3: Overall performance comparison of AC processors using inland and lakes match-ups with MSI and OLI data combined. Detailed statistical metrics and the number of match-ups per processor are reported in Table. I. The solid black lines are the 1:1 match.

whether the AC schemes meet the currently defined 30% threshold requirements (Global Climate Observing System; GCOS [28]) across all the bands, it is noticeable that among the five AC schemes validated in this study, only OC-SMART appears to meet the < 30% retrieval accuracy across the four visible bands. The number of match-ups (N=40) is also considered adequate compared to C2RCC, Acolite, and ICOR (see Table. I).

Using the common match-ups between the AC processors, on average no significant differences are observed and our discussion remains the same as using all valid match-ups. For example, the averaged MAPD remains the same for OC-SMART and Polymer and <2% increase for Polymer. The RMSLD reduces by 14% for OC-SMART, 19% for Polymer; however, raised by 12% for ICOR retrieved ρ_w data.

B. Spectral bandpass adjustment for ρ_w

Our results in section IV-A indicate that the ρ_w products retrieved via OC-SMART are in good agreement with the in-situ observations compared to the other AC algorithms. Therefore, the near-simultaneous OLI and MSI TOA images were processed via OC-SMART to estimate ρ_w products, also called inter-comparisons (section III-C). As mentioned in section I, the primary objective of this study is to harmonize OLI-MSI ρ_w products to increase the number of match-ups to better tune the retrieval models. The relationships between the OLI and MSI-derived ρ_w products retrieved via OC-SMART are shown in Fig. 4 (a1-a4). Whereas, the regression plots between OLI-ρ_w and the band adjusted MSI-ρ_w products ($MSI^*\rho_w$) using OLS regression, and the proposed BA model, in the common visible bands, are shown in Fig. 4.

From 30 concurrent OLI and MSI observations selected over the study region, 4040 inter-comparisons were created after the filtering criteria described in section III-C.

The average differences in ρ_w products retrieved via OC-SMART (without spectral BA) are estimated to range from 13 to ~ 35% (Table. II). Visual inspection of the scatter

TABLE I: Performance comparison associated with match-ups acquired over inland and coastal waters for each processor.

Bands	N	RMSD (10^{-2})	RMSLD	MAPD	MRPD
All match-ups					
443 nm Acolite	25	0.93	0.20	32.2	22.1
492 nm Acolite	25	0.83	0.14	18.8	0.60
560 nm Acolite	25	0.92	0.10	10.5	2.1
665 nm Acolite	25	0.90	0.23	42.9	42.9
443 nm C2RCC	26	0.73	0.41	42.2	-20.1
492 nm C2RCC	26	0.88	0.397	29.3	-18.1
560 nm C2RCC	26	1.72	0.43	22.1	-19.2
665 nm C2RCC	26	2.06	0.60	49.1	-26.7
443 nm Polymer	47	0.81	0.28	30.9	-6.0
492 nm Polymer	47	0.74	0.21	13.9	-6.1
560 nm Polymer	47	1.09	0.19	25.4	-14.5
665 nm Polymer	47	0.79	0.40	35.1	-7.8
443 nm OC-SMART	40	1.03	0.33	28.9	-14.0
492 nm OC-SMART	40	1.15	0.278	20.3	-20.3
560 nm OC-SMART	40	0.89	0.13	21.5	-13.3
665 nm OC-SMART	40	0.70	0.18	13.8	8.6
443 nm ICOR	34	1.21	0.241	37.2	-7.1
492 nm ICOR	34	1.16	0.30	36.2	-18.9
560 nm ICOR	34	1.13	0.26	23.2	-8.9
665 nm ICOR	34	0.87	0.51	21.8	-5.9
Common match-ups					
443 nm OC-SMART	26	0.98	0.29	26.72	-13.6
492 nm OC-SMART	26	0.91	0.19	25.3	-17.3
560 nm OC-SMART	26	0.08	0.14	21.8	-15.5
665 nm OC-SMART	26	0.72	0.17	12.1	7.3
443 nm Polymer	26	0.90	0.22	30.9	-28.8
492 nm Polymer	26	0.80	0.17	18.3	-13.2
560 nm Polymer	26	0.17	0.15	25.42	-20.4
665 nm Polymer	26	0.32	0.33	31.3	-7.3
443 nm ICOR	26	1.3	0.26	38.4	-0.6
492 nm ICOR	26	1.2	0.23	36.9	-16.4
560 nm ICOR	26	1.1	0.29	21.5	-8.4
665 nm ICOR	26	1.05	0.66	30.7	2.2

TABLE II: Inter-comparison of OLI-MSI ρ_w products for N=4040 pixel pairs.

Method	RMSD (10^{-3} sr^{-1})	RMSLD	MAPD	MRPD	R^2	Slope
Coastal aerosol (443 nm)						
Proposed NN	1.95	0.055	7.266	0.9	0.949	1.001
OLS	3.72	0.07	10.878	-0.6	0.815	0.884
No Bandpass Adjustment	3.40	0.248	20.066	-11.154	0.844	0.784
Blue (482 nm)						
Proposed NN	1.73	0.044	3.76	-1.009	0.972	1.017
OLS	4.76	0.052	4.951	-1.244	0.788	0.822
No Bandpass Adjustment	3.90	0.171	13.732	6.274	0.857	0.753
Green (561 nm)						
Proposed NN	2.70	0.031	3.658	-0.818	0.985	1.018
OLS	7.09	0.096	14.301	-6.296	0.897	0.893
No Bandpass Adjustment	5.94	0.15	18.372	-17.276	0.928	1.134
Red (665 nm)						
Proposed NN	2.75	0.057	7.646	0.079	0.981	1.004
OLS	3.29-03	0.094	14.356	-1.832	0.973	0.972
No Bandpass Adjustment	10.02	0.199	35.298	-35.284	0.752	1.521

plots in Fig. 4 (a1-a4) and the distributions of OLI-MSI ρ_w products (Fig. 5) illustrate that MSI underestimates at all wavebands except in the blue band. However, besides over/underestimation, both sensors show either uni or multi-modal distribution in all the bands, as shown in Fig. 5. For instance, in the green band, a bi-modal distribution is observed where the histograms are comparatively more aligned especially for the first peak (lower values of ρ_w).

Comparing all the evaluation metrics, the minimum spectral difference between the reflectance products is achieved in the ρ_w (561 nm) products with RMSLD=0.15 and R^2 =∼ 0.93%. The MAPD is higher than the ρ_w(482 nm); however, comparable to ρ_w(443 nm) products. The highest bias is observed in the ρ_w(665 nm) products with MRPD of ∼ −35% and RMSLD=0.199. The worst performance in the red band is likely due to the optical diversity of our dataset; i.e., coastal and inland waters. In addition, it is partially due to the minimum percentage of overlap in the SRF and larger difference in the central wavelengths in the red band [48], which also contributes to the higher bias.

After applying the proposed spectral BA, the average

spectral difference was significantly reduced from < 21% to < 6%. The histograms are much more aligned, demonstrating the effectiveness of the proposed approach (Fig. 5 (c1-c4)). For instance, in the ρ_w(483 nm) products, significant improvement is achieved in the alignment of the three density curves compared to the linear adjustment (see Fig. 5(c2)). The OLS method has improved the alignment in the first peak; however, significant differences are observed in the second and third peak positions (see Fig. 5(c2)). Considering RMSLD and MAPD as performance measures in Table. II, on average, the proposed BA approach reduced the MAPD and RMSLD by ~ 15% and ~ 76%, compared to the ~ 11% and ~ 59% improvement caused by OLS regression model. The highest improvement is achieved in the ρ_w(665 nm) products by the NN method, with 72% reduction in the RMSD. Overall, our results indicate that the proposed BA model has caused significant improvement in the spectral consistency with %15 increase in the R^2 score. As illustrated in Table. II, the spectral differences are reduced in all the bands.

The average difference of MAPD=21% in the OLI-MSI ρ_w products could be due to several factors including the optical complexity of water (lakes and coastal areas), adjacency effect from the neighboring pixels especially in the smaller lakes, inaccurate removal of sky reflectance or differences between the estimated optical depth (AOD) between OLI and MSI [3], [28]. The difference between OLI-MSI aod-560 and Chl-a products is illustrated in Fig. 6. The differences in OLI-MSI aod-560 products may be due to a change in atmospheric conditions such as aerosol loads within the short (±30 minutes) time-difference, while the differences in OLI-MSI Chl-a products are likely to be attributed to the differences in their respective aod-560 and ρ_w products.

C. Estimation of biogeochemical variables

In this section, we have compared the performance of OCN in the estimation of Chl-a and CDOM with an ML-based model, GPR, and band ratio-based (OC3 for Chl-a and exponential model for CDOM). A summary of algorithms performances in terms of retrieval errors is illustrated in Table. III and Table. IV.

1) Chl-a retrievals: Considering the Chl-a retrievals, using only OLI-ρ_w data (setting I), Table. III and scatter plots in Fig. 7 (a1-a4) show that, all the algorithms exhibit high bias. For instance, the RMSD> $2sr^{-1}$ and $R^2 < 0.7$ illustrating their degraded performance using OLI-ρ_w match-ups only. Comparing all the evaluation metrics, the highest uncertainties are obtained in the OC-SMART retrievals with MAPD=68.7% and MAE=138% showing high over/underestimating of Chl-a content. The ML-based algorithms, the OCN, and GPR retrievals also exhibit high errors with MAE=73 and 78% illustrating significant over/underestimation of Chl-a values. The degraded performance of all the algorithms in setting I (using only OLI math-ups) is may be due to the limited amount of training data.

In setting II (using OLI-MSI ρ_w data), all the algorithms are found to return more accurate products with RMSD< $1.2sr^{-1}$ and $R^2 > 0.78$ (excluding OC-SMART). Comparing all the evaluation metrics in Table. III and scatter plots in Fig. 7 (b1-b4), the OCN has outperformed the ML and band ratio-based algorithms with R^2 ~= 0.9 and MAE=42%. The obtained results show that the combined OLI-MSI ρ_w data have resulted in better training and optimization of the retrieval algorithms.

In setting III (OLI-MSI$^*\rho_w$ data), both GPR and OCN achieved improved performances, for instance, the MAE is reduced by 9% and 21% illustrating a decrease in the degree of over/underestimation of Chl-a estimates (see Fig. 7 (c1-c3)). The improved performances using OLI-MSI$^*\rho_w$data are due to the spectral alignment of OLI-MSI ρ_w products. In contrarily, no significant differences are observed in OC3 retrievals.

2) CDOM retrievals: Using only OLI-ρ_w data (setting I), similar to Chl-a retrievals, the ML-based algorithms have outperformed the band ratio-based model in estimating CDOM. Table. IV and scatter plots in Fig. 8 (a1) and (a3) illustrate that the OCN and GPR results are close to each other. In setting II, a significant reduction in RMSD (50% for GPR and 15% for band ratio) algorithms is observed. In addition, R^2 also shows considerable improvement, especially for the band ratio algorithm (increased from 0.58 to 0.77). However, significant overestimation is observed in band ratio-based algorithm retrievals and data is spread above the central line (see Fig. 8(b2)). Comparing all the evaluation metrics, the best results are obtained by using combined $OLI-MSI^*\rho_w$ data. The RMSD and RMSLD are minimum and R^2 is close to 1. Comparing the three settings, the OCN and GPR are top performers in CDOM retrievals.

It is noted that in all settings, the ML-based algorithms have outperformed the band ratio-based models in estimating in-water quantities illustrating their superior performance in optically complex waters. A shown in Fig. 8 (c1-c3), the best results are obtained using the combined OLI-MSI$^*\rho_w$ match-ups which further encourage to use of harmonized MSI and OLI data products.

D. Visual comparison of OLI-MSI* Chl-a and CDOM products

To further elaborate on the consistent retrieval of Chl-a and CDOM using combined OLI and MSI$^*\rho_w$ data, we have used additional OLI and MSI image pairs that were not included in the training of the BA model (Section III-C). Fig. 9 shows the near-simultaneous OLI and MSI images acquired on March 3, 2021, over the Green Salt Lake in the US.

Fig. 10 illustrates the Chl-a and CDOM products retrieved from OLI-ρ_w, MSI-ρ_w, and MSI$^*\rho_w$ products shown in Fig. 9. It can be seen that the spatial details and variations are preserved in the Chl-a and CDOM products estimated from MSI$^*\rho_w$ products with a decrease in the difference between the pixel values. For example, Chl-a

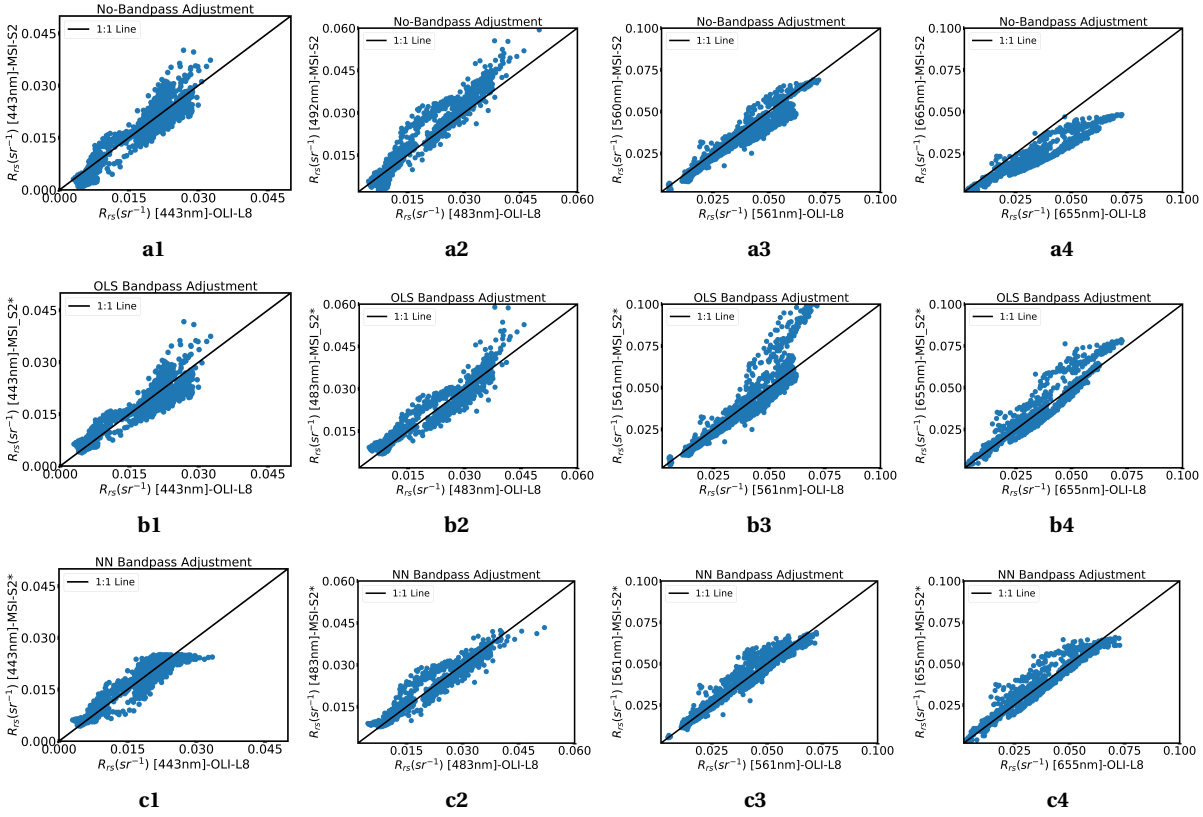

Fig. 4: Inter-comparison of OLI-MSI ρ_w products in the common visible bands before spectral BA (a1-a4), and after spectral BA using OLS regression (b1-b4) and the proposed BA model (c1-c4). Detailed statistical metrics are available in Table. II.

products retrieved from MSI are higher in values than OLI especially away from the coast. After bandpass adjustment, the differences are significantly reduced. The Chl-a values estimated from OLI and MSI* ρ_w are below 5 mg/m^3 away from the shore. Nearshore, both OLI and MSI-derived Chl-a products indicate higher values, which are retained in the MSI* derived Chl-a products with a slight reduction.

Similarly, CDOM products retrieved from MSI-ρ_w are higher in magnitude especially near shore compared to OLI. Away from the shore, OLI-derived Chl-a products are higher in magnitude than MSI. These differences are reduced significantly in the MSI* derived Chl-a products.

The Chl-a and CDOM products are retrieved from ρ_w products.Therefore, the consistency between OLI and MSI-drived CDOM and Chl-a products are dependent on the similarities and differences in their perspective ρ_w products. To further investigate the improvement in consistency in OLI and MSI*-derived Chl-a and CDOM products illustrated in Fig. 10, we have shown the ρ_w products retrieved from OLI, MSI, and MSI* side by side in Fig. 9. The differences between OLI and MSI-derived ρ_w products in common bands are highlighted by ellipses. These discrepancies are minimized after BA of MSI-derived products as illustrated by the ellipses.

V. Conclusion and Future Work

In this paper, we made an effort to retrieve Chl-a and CDOM from combined Sentinel-2 MSI and Landsat-8 OLI ρ_w products over global coastal and inland waters.

To achieve our objective, we processed Landsat-8 and Sentinel-2 level-1 imagery via Acolite (DSF), C2RCC, ICOR, OC-SMART and Polymer for atmospheric correction. The atmospherically corrected ρ_w products were then compared with the in-situ ρ_w measurements. Our analysis demonstrates that overall, all the processors have degraded performance in the coastal aerosol band center at 443 nm with MAPD ranges from 28 (OC-SMART) to 42% (C2RCC). In the blue band, Polymer retrieved ρ_w products were found in close agreement with in-situ ρ_w data followed by OC-SMART. Acolite was top performer in the green band with MAPD $<$ 11% and REMSD=0.0092 sr^-1 whereas, the remaining AC processes underestimated the ρ_w values. Comparatively, OC-SMART was found to be more reliable in the red band with a MAPD=13.8% compared to 21 to 42 % errors in the retrieval of other AC schemes. Overall, OC-SMART showed the minimum deviation from the in-situ ρ_w observations with MAPD $<$ 30% across the visible bands, indicating consistent performance over different water types.

To generate harmonized ρ_w products from OLI and

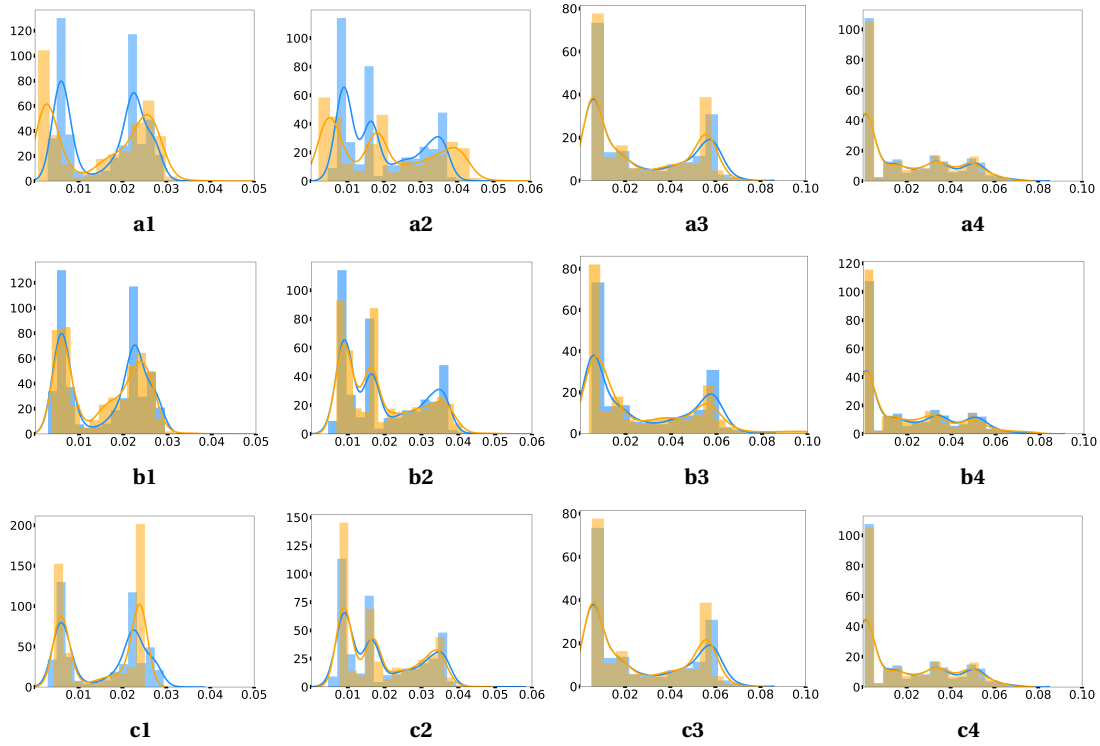

Fig. 5: Distribution of of OLI-MSI ρ_w products before adjustment (a1-a4), and after adjustment using OLS regression (b1-b4) and proposed BA model (c1-c4) in the common visible bands.

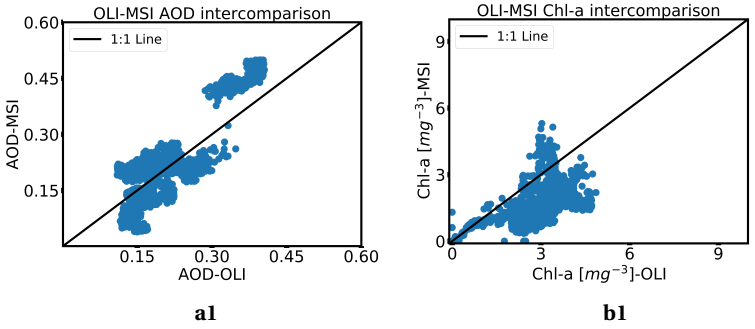

Fig. 6: Inter-comparison of a) AOD and b) Chl-a products for OLI and MSI estimated from OC-SMART.

TABLE III: Performance comparison between OCN, GPR, OC-SMART and OC3 in estimating Ch-a in three different settings.

Method	RMSD sr^{-1})	RMSLD	MAPD	MRPD	R^2	MAE
			setting I			
Proposed NN	2.0539	0.3005	47.7834	1.2044	0.6783	1.7302
GPR	2.3974	0.3861	23.574	-1.226	0.469	1.7863
OC-SMART	2.45	0.439	68.77	-2.61	0.31	2.3813
OC3	2.3371	0.33324	49.438	-7.619	0.604691	1.8059
			setting II			
Proposed NN	0.7661	0.2147	26.66	-2.636	0.8951	1.4196
GPR	1.07255	0.29949	24.5182	-1.6029	0.7959	1.5728
OC-SMART	2.19	0.49	69.09	-0.911	0.42	2.54
OC3	1.1667	0.2635	24.456	-4.985	0.842	1.5373
			setting III			
Proposed NN	1.539	0.2054	10.7673	2.6292	0.9040	1.3265
GPR	1.74470	0.21841	13.33	-1.05	0.8915	1.3645
OC3	1.20594	0.289	28.168	-3.5849	0.809	1.6323

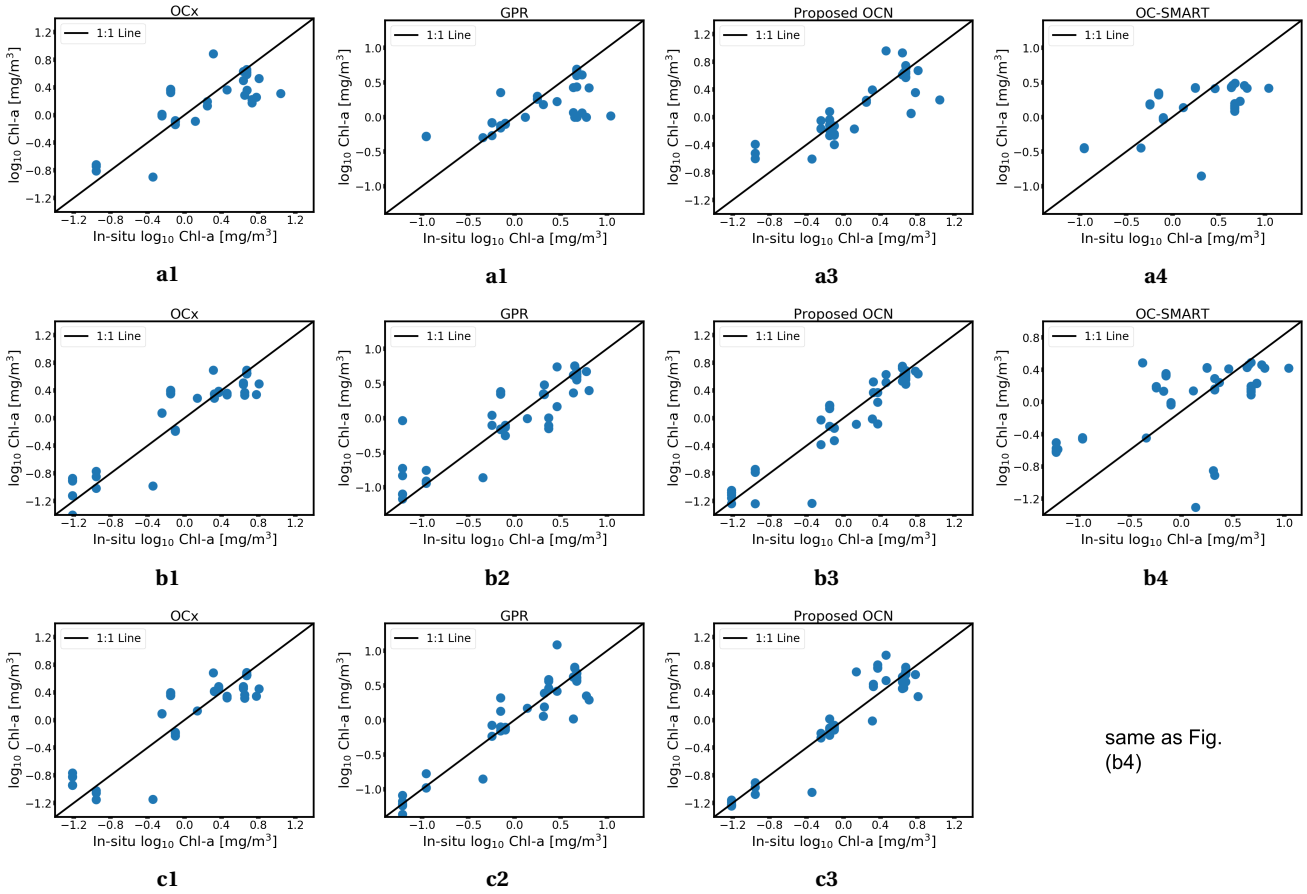

Fig. 7: Estimated Chl-a from OCx, GPR, OCN and OC-SMART using OLI (a1-a4), combined OLI-MSI (b1-b4) and combined OLI-MSI* ρ_w data (c1-c3).

MSI images for seamless retrieval of WQI, we processed Landsat-8 and Sentinel-2 level-1 imaginary via OC-SMART for atmospheric correction. Our results indicate that the ρ_w products processed via OC-SMART are estimated to range from 13 to 35% in the common visible bands. Landsat-8 OLI-derived ρ_w products are higher in magnitude than that of Sentinel-2 MSI-derived ρ_w products. The highest bias is found in the ρ_w (665 nm) products with MAPD= ~ 5%. The minimum spectral difference is achieved in the blue band with MAPD and RMSD of 13% and 3.9×10^{-3}. To merge OLI and MSI-derived ρ_w products for retrieval of Chl-a and CDOM, an NN-based BA model is applied for spectral alignment of OLI-MSI ρ_w products in the common visible bands. After applying the NN-based BA model, the spectral difference were found in the range from 3 to < 8%, indicating relatively consistent products for real-world Landsat-8 and Sentinel-2 imagery. The weights and bias terms optimized during the transformation of near-simultaneous MSI images to that of OLI images were applied to MSI-derived ρ_w data.

The OLI and MSI-derived ρ_w data were then used in three different settings to train and validate the performance of retrieval models in estimating Chl-a and CDOM. Our results show that using OLI data only, high bias is found in the Chl-a estimates by all the algorithms. Using the OLI-MSI dataset, considerable improvement was observed in all the methods. For instance, MAE was reduced by 32% for OCN, 20% for GRP and 27% for OC3. The MAE was further reduced by 8% and 21% for OCN and GPR after using OLI-MSI* data. Similarly, improved performances were observed in CDOM estimation using OLI-MSI* data.The RMSD was reduced by 9% for OCN, 62% for GPR, and 15% for the band ratio-based algorithm.

Overall, our results indicate that using combined OLI and MSI* data, remarkable improvement was observed in the estimation of WQIs. Our approach to integrating real word imagery of MSI-OLI demonstrates that MSI is an ideal candidate to augment Landsat-8 for water monitoring applications. The combined products will not only fill the data gaps in future scientific applications but also beneficial for Landsat data continuity [22]. However, as the results are strongly dependent on the performance of AC, caution should be used in the selection and optimization of the AC algorithm. In addition, the additional NIR bands in MSI which have been proven beneficial for Chl-a retrievals in highly turbid waters, there must be a compromise in the combined use of these sensors [5], [25]. For example, MSI-derived WQIs can be produced independent of OLI over

TABLE IV: Performance comparison between OCN, GPR, OC-SMART and band-ratio based method in estimating CDOM in three different settings.

Method	RMSD sr^{-1})	RMSLD	MAPD	MRPD	R^2	MAE
			setting I			
Proposed NN	0.369	0.278	19.315	-6.0244	0.834	1.4337
GPR	0.872	0.3241	7.9697	1.484	0.7751	1.444
Band Ratio	0.5768	0.4418	53.231	1.934	0.5822	2.2490
			setting II			
Proposed NN	0.36684	0.2450	21.51	3.937	0.915	1.4534
GPR	0.440	0.352	13.291	0.84254	0.824	1.4335
Band Ratio	0.4983	0.3967	45.3911	-10.2	0.777	2.0792
			setting III			
Proposed NN	0.33531	0.2236	30.364	9.627	0.9292	1.4337
GPR	0.32949	0.2717	9.739	0.3007	0.89550	1.3208
Band Ratio	0.486548	0.39377	53.011	-10.2	0.780	2.0397

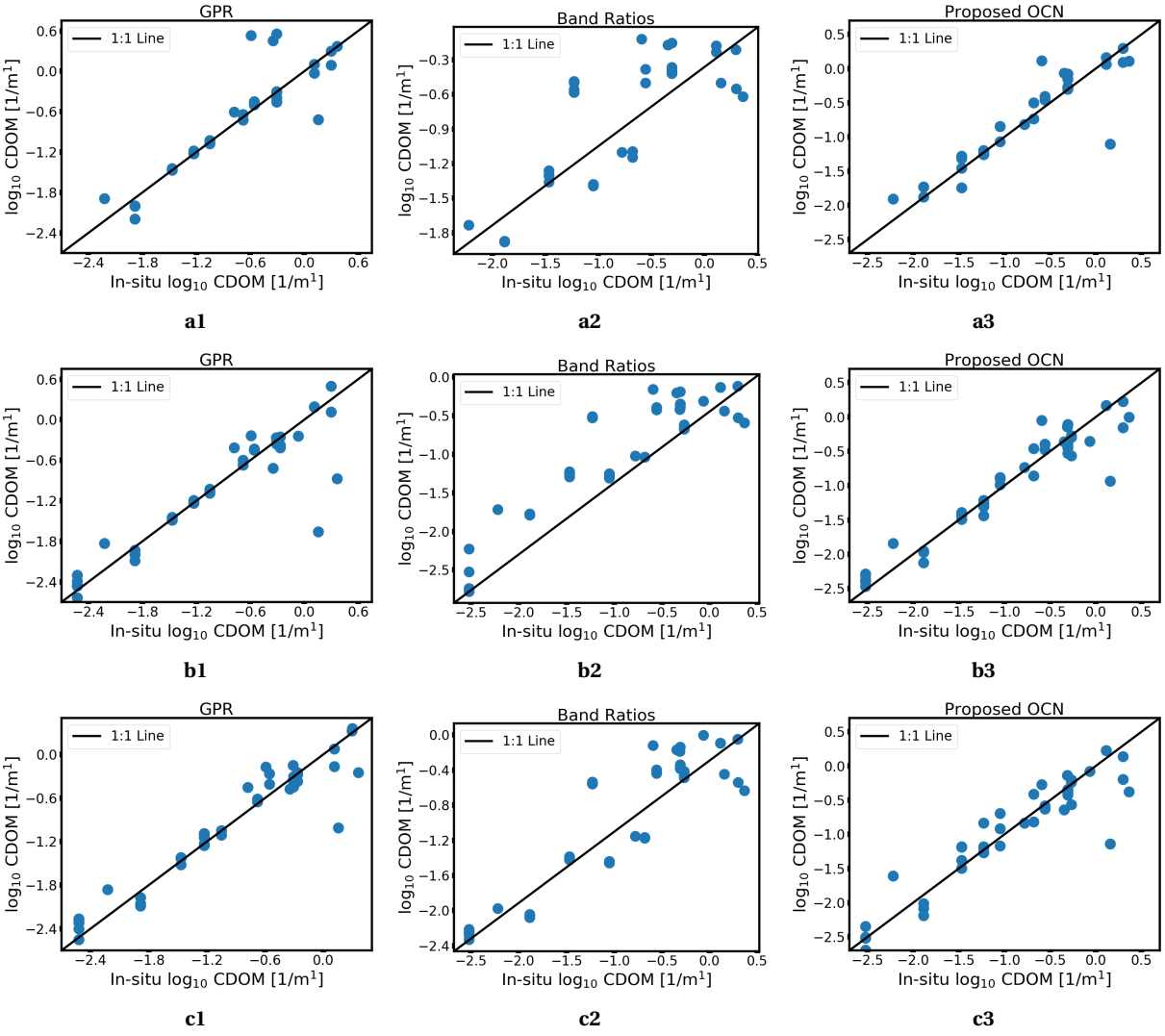

Fig. 8: Estimated CDOM concentrations from GPR, band-ratio algorithm, and OCN using OLI (a1-a3), combined OLI-MSI (b1-b3) and combined OLI-MSI* ρ_w data (c1-c3) .

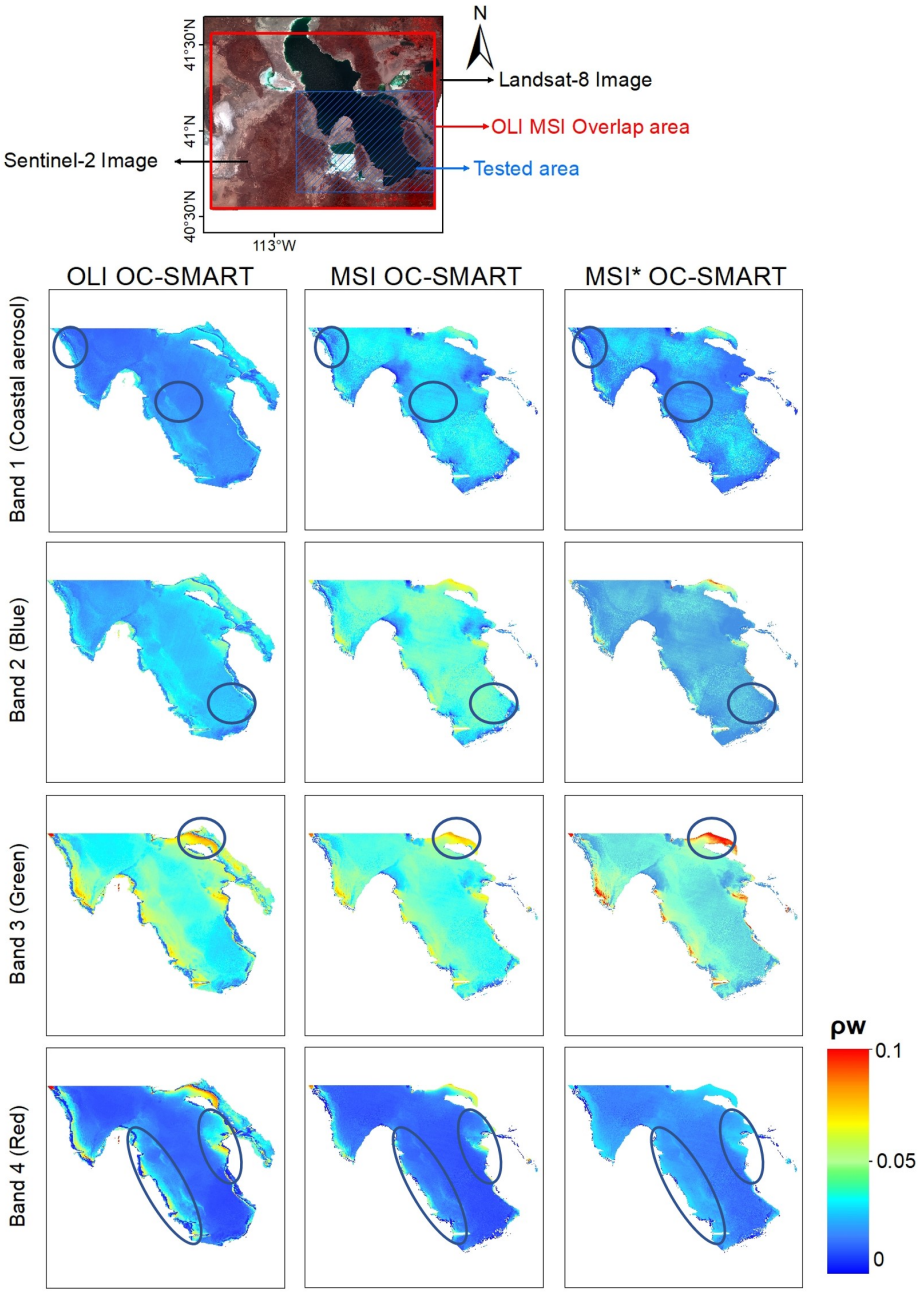

Fig. 9: Comparison between near-simultaneous OLI-ρ_w, MSI-ρ_w and MSI*ρ_w products. The ρ_w products from OLI and MSI images are derived via OC-SMART for the common bands. The areas indicated by ellipses show differences in OLI and MSI-derived ρ_w values. These differences are minimized after applying the proposed BA model. The OLI-ρ_w, MSI-ρ_w and MSI*ρ_w products are used in Fig. 10 to derive Chla and CDOM maps.

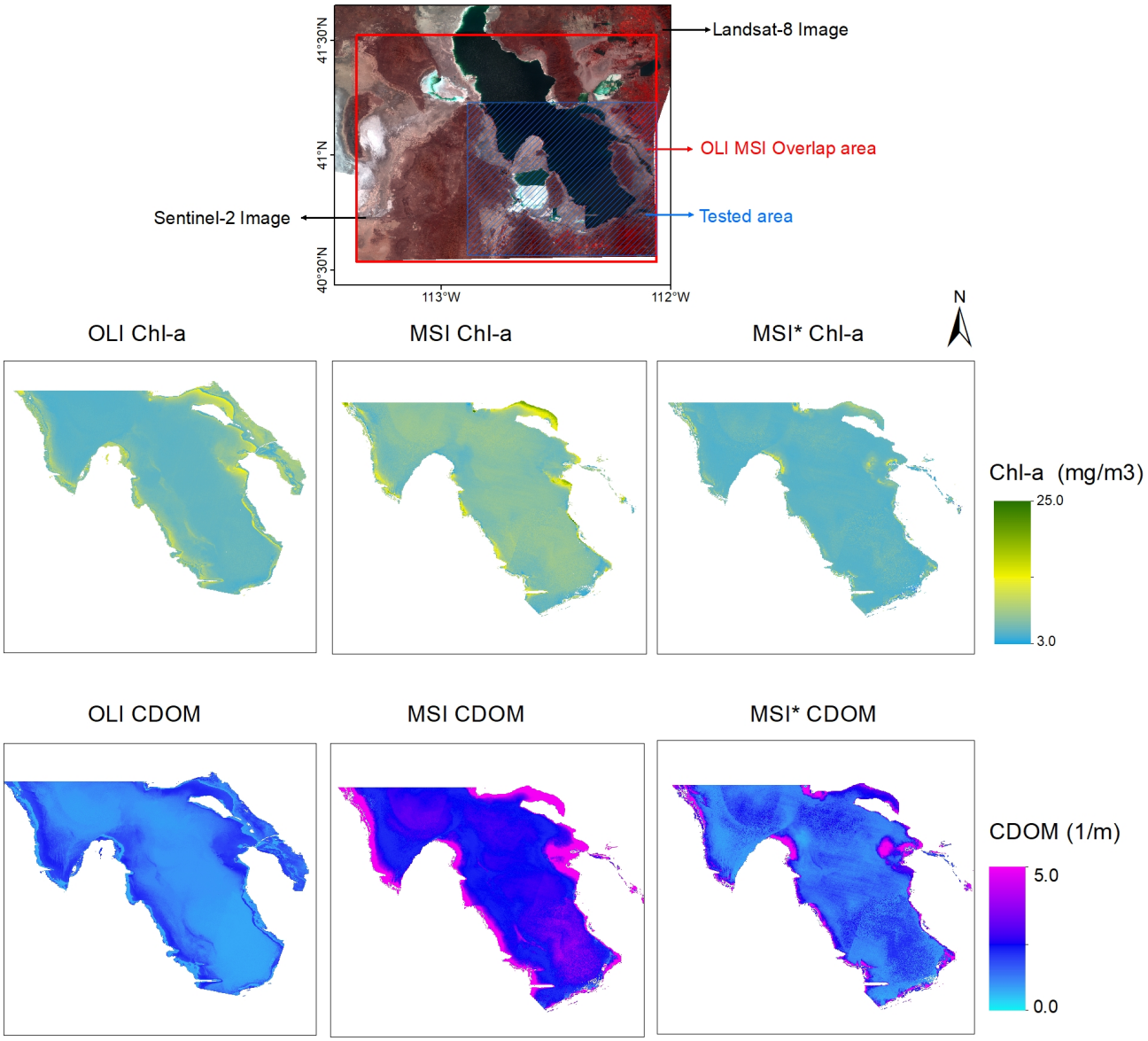

Fig. 10: Comparison between Chl-a and CDOM maps derived from OLI, MSI and MSI*.

highly turbid waters while the combined MSI and OLI data can be used for moderately turbid waters.

Future directions include exploiting virtual constellations for different water types from mesotrophic to hypereutrophic waters. In addition, we intend to demonstrate the capabilities of combining Landsat-8, Landsat-9, and Sentinel-2 imagery for the estimation of Inherent optical properties for continuous monitor the biogeochemical changes occurring at a smaller spatial scale especially.

APPENDIX A

The OC3 Chl-a retrieval algorithm [46] is given by Eq. (A.1). The value of x is configured with respect to both OLI and MSI bands (B).

$$x = log_{10}[(max[R_{rs}(B1), R_{rs}(B2)]) * R_{rs}(B3)^{-1}] \quad \text{(A.1)}$$

$$y = a_0 + a_1 x + a_2 x^2 + a_3 x^3 + a_4 x^4$$
$$OC3_{LT} = 10^y$$

The values of coefficients of the polynomial expression are computed by minimization of sum of Least Error Squares for each split (k-fold) using the training data only.

$$Y = Xa$$
$$a = (X^T X)^{-1} X^T Y$$

The CDOM retrieval algorithm [47] is given by Eq. (A.2). The value of x is configured with respect to both OLI and MSI bands (B).

$$x = R_{rs}(B3)/R_{rs}(B4)$$

$$a_{CDOM}(440) = ae^{bx} \tag{A.2}$$

The parameters a and b are tuned by fitting a polynomial function to data using the polyfit function in Python.

CONTRIBUTION

DECLARATION OF COMPETING INTERESTS

None.

ACKNOWLEDGMENT

The research is funded by the following projects: The Nansen Legacy (RCN number 276730), CIRFA (RCN number 237906), and partners. The authors would like to acknowledge U.S Geological Survey (USGS) and Copernicus Open Access Hub European space agency (ESA) for providing Landsat-8 (OLI) and Sentinel-2 image archives.

REFERENCES

[1] M. Asim, A. Matsuoka, P. G. Ellingsen, C. Brekke, T. Eltoft, and K. Blix, "A new spectral harmonization algorithm for landsat-8 and sentinel-2 remote sensing reflectance products using machine learning: a case study for the barents sea (european arctic)," *IEEE Transactions on Geoscience and Remote Sensing*, 2022.

[2] M. Asim, C. Brekke, A. Mahmood, T. Eltoft, and M. Reigstad, "Improving chlorophyll-a estimation from sentinel-2 (msi) in the barents sea using machine learning," *IEEE Journal of Selected Topics in Applied Earth Observations and Remote Sensing*, 2021.

[3] M. A. Warren, S. G. Simis, V. Martinez-Vicente, K. Poser, M. Bresciani, K. Alikas, E. Spyrakos, C. Giardino, and A. Ansper, "Assessment of atmospheric correction algorithms for the sentinel-2a multispectral imager over coastal and inland waters," *Remote sensing of environment*, vol. 225, pp. 267–289, 2019.

[4] N. Pahlevan, B. Smith, J. Schalles, C. Binding, Z. Cao, R. Ma, K. Alikas, K. Kangro, D. Gurlin, N. Hà *et al.*, "Seamless retrievals of chlorophyll-a from sentinel-2 (msi) and sentinel-3 (olci) in inland and coastal waters: A machine-learning approach," *Remote Sensing of Environment*, p. 111604, 2020.

[5] N. Pahlevan, S. K. Chittimalli, S. V. Balasubramanian, and V. Vellucci, "Sentinel-2/landsat-8 product consistency and implications for monitoring aquatic systems," *Remote sensing of Environment*, vol. 220, pp. 19–29, 2019.

[6] M. Claverie, J. Ju, J. G. Masek, J. L. Dungan, E. F. Vermote, J.-C. Roger, S. V. Skakun, and C. Justice, "The harmonized landsat and sentinel-2 surface reflectance data set," *Remote sensing of environment*, vol. 219, pp. 145–161, 2018.

[7] R. Shang and Z. Zhu, "Harmonizing landsat 8 and sentinel-2: A time-series-based reflectance adjustment approach," *Remote Sensing of Environment*, vol. 235, p. 111439, 2019.

[8] Q. Vanhellemont and K. Ruddick, "Acolite for sentinel-2: Aquatic applications of msi imagery," in *Proceedings of the 2016 ESA Living Planet Symposium, Prague, Czech Republic*, 2016, pp. 9–13.

[9] J. Li and D. P. Roy, "A global analysis of sentinel-2a, sentinel-2b and landsat-8 data revisit intervals and implications for terrestrial monitoring," *Remote Sensing*, vol. 9, no. 9, p. 902, 2017.

[10] S. Hafeez, M. S. Wong, H. C. Ho, M. Nazeer, J. Nichol, S. Abbas, D. Tang, K. H. Lee, and L. Pun, "Comparison of machine learning algorithms for retrieval of water quality indicators in case-ii waters: a case study of hong kong," *Remote Sensing*, vol. 11, no. 6, p. 617, 2019.

[11] T. Zhang, M. Huang, and Z. Wang, "Estimation of chlorophyll-a concentration of lakes based on svm algorithm and landsat 8 oli images," *Environmental Science and Pollution Research*, vol. 27, no. 13, pp. 14 977–14 990, 2020.

[12] M. Asim, C. Brekke, A. Mahmood, T. Eltoft, and M. Reigstad, "Ocean color net (ocn) for the barents sea," in *IGARSS 2020-2020 IEEE International Geoscience and Remote Sensing Symposium*. IEEE, 2020, pp. 5881–5884.

[13] S. Li, K. Song, S. Wang, G. Liu, Z. Wen, Y. Shang, L. Lyu, F. Chen, S. Xu, H. Tao *et al.*, "Quantification of chlorophyll-a in typical lakes across china using sentinel-2 msi imagery with machine learning algorithm," *Science of the Total Environment*, vol. 778, p. 146271, 2021.

[14] F. Watanabe, E. Alcantara, T. Rodrigues, L. Rotta, N. Bernardo, and N. Imai, "Remote sensing of the chlorophyll-a based on oli/landsat-8 and msi/sentinel-2a (barra bonita reservoir, brazil)," *Anais da Academia Brasileira de Ciências*, vol. 90, pp. 1987–2000, 2017.

[15] N. Pahlevan, B. Smith, K. Alikas, J. Anstee, C. Barbosa, C. Binding, M. Bresciani, B. Cremella, C. Giardino, D. Gurlin *et al.*, "Simultaneous retrieval of selected optical water quality indicators from landsat-8, sentinel-2, and sentinel-3," *Remote Sensing of Environment*, vol. 270, p. 112860, 2022.

[16] B. P. Page, L. G. Olmanson, and D. R. Mishra, "A harmonized image processing workflow using sentinel-2/msi and landsat-8/oli for mapping water clarity in optically variable lake systems," *Remote Sensing of Environment*, vol. 231, p. 111284, 2019.

[17] I. Caballero, A. Román, A. Tovar-Sánchez, and G. Navarro, "Water quality monitoring with sentinel-2 and landsat-8 satellites during the 2021 volcanic eruption in la palma (canary islands)," *Science of the Total Environment*, vol. 822, p. 153433, 2022.

[18] C. Kuhn, A. de Matos Valerio, N. Ward, L. Loken, H. O. Sawakuchi, M. Kampel, J. Richey, P. Stadler, J. Crawford, R. Striegl *et al.*, "Performance of landsat-8 and sentinel-2 surface reflectance products for river remote sensing retrievals of chlorophyll-a and turbidity," *Remote Sensing of Environment*, vol. 224, pp. 104–118, 2019.

[19] H. Wang, J. Wang, Y. Cui, and S. Yan, "Consistency of suspended particulate matter concentration in turbid water retrieved from sentinel-2 msi and landsat-8 oli sensors," *Sensors*, vol. 21, no. 5, p. 1662, 2021.

[20] S. Hafeez, M. S. Wong, S. Abbas, and M. Asim, "Evaluating landsat-8 and sentinel-2 data consistency for high spatiotemporal inland and coastal water quality monitoring," *Remote Sensing*, vol. 14, no. 13, p. 3155, 2022.

[21] J. Wang, Z. Lee, D. Wang, S. Shang, J. Wei, and A. Gilerson, "Atmospheric correction over coastal waters with aerosol properties constrained by multi-pixel observations," *Remote Sensing of Environment*, vol. 265, p. 112633, 2021.

[22] H. K. Zhang, D. P. Roy, L. Yan, Z. Li, H. Huang, E. Vermote, S. Skakun, and J.-C. Roger, "Characterization of sentinel-2a and landsat-8 top of atmosphere, surface, and nadir brdf adjusted reflectance and ndvi differences," *Remote sensing of environment*, vol. 215, pp. 482–494, 2018.

[23] D. Scheffler, D. Frantz, and K. Segl, "Spectral harmonization and red edge prediction of landsat-8 to sentinel-2 using land cover optimized multivariate regressors," *Remote Sensing of Environment*, vol. 241, p. 111723, 2020.

[24] K. T. Peterson, V. Sagan, and J. J. Sloan, "Deep learning-based water quality estimation and anomaly detection using landsat-8/sentinel-2 virtual constellation and cloud computing," *GIScience & Remote Sensing*, vol. 57, no. 4, pp. 510–525, 2020.

[25] M. A. Warren, S. G. Simis, and N. Selmes, "Complementary water quality observations from high and medium resolution sentinel sensors by aligning chlorophyll-a and turbidity algorithms," *Remote Sensing of Environment*, vol. 265, p. 112651, 2021.

[26] J. Chen and W. Zhu, "Comparing landsat-8 and sentinel-2 top of atmosphere and surface reflectance in high latitude regions: case study in alaska," *Geocarto International*, pp. 1–20, 2021.

[27] S. Xie, L. Sun, L. Liu, and X. Liu, "Global cross-sensor transformation functions for landsat-8 and sentinel-2 top of atmosphere and surface reflectance products within google earth engine," *IEEE Transactions on Geoscience and Remote Sensing*, 2022.

[28] N. Pahlevan, A. Mangin, S. V. Balasubramanian, B. Smith, K. Alikas, K. Arai, C. Barbosa, S. Bélanger, C. Binding, M. Bresciani *et al.*, "Acix-aqua: A global assessment of atmospheric correction methods for landsat-8 and sentinel-2 over lakes, rivers, and coastal waters," *Remote Sensing of Environment*, vol. 258, p. 112366, 2021.

[29] C. Brockmann, R. Doerffer, M. Peters, S. Kerstin, S. Embacher, and A. Ruescas, "Evolution of the c2rcc neural network for sentinel 2 and 3 for the retrieval of ocean colour products in normal and extreme

optically complex waters," in *Living Planet Symposium*, vol. 740, 2016, p. 54.
[30] Q. Vanhellemont, "Adaptation of the dark spectrum fitting atmospheric correction for aquatic applications of the landsat and sentinel-2 archives," *Remote Sensing of Environment*, vol. 225, pp. 175–192, 2019.
[31] F. Steinmetz, P.-Y. Deschamps, and D. Ramon, "Atmospheric correction in presence of sun glint: application to meris," *Optics express*, vol. 19, no. 10, pp. 9783–9800, 2011.
[32] Y. Fan, W. Li, N. Chen, J.-H. Ahn, Y.-J. Park, S. Kratzer, T. Schroeder, J. Ishizaka, R. Chang, and K. Stamnes, "Oc-smart: A machine learning based data analysis platform for satellite ocean color sensors," *Remote Sensing of Environment*, vol. 253, p. 112236, 2021.
[33] S. B. Hooker, A. Matsuoka, R. M. Kudela, Y. Yamashita, K. Suzuki, and H. F. Houskeeper, "A global end-member approach to derive a cdom (440) from near-surface optical measurements," *Biogeosciences*, vol. 17, no. 2, pp. 475–497, 2020.
[34] J. H. Morrow, S. B. Hooker, C. R. Booth, G. Bernhard, R. N. Lind, and J. W. Brown, "Advances in measuring the apparent optical properties (aops) of optically complex waters," *NASA Tech. Memo*, vol. 215856, pp. 42–50, 2010.
[35] A. Matsuoka, J. W. Campbell, S. B. Hooker, F. Steinmetz, K. Ogata, T. Hirata, H. Higa, V. S. Kuwahara, T. Isada, K. Suzuki *et al.*, "Performance of jaxa's sgli standard ocean color products for oceanic to coastal waters: chlorophyll a concentration and light absorption coefficients of colored dissolved organic matter," *Journal of Oceanography*, vol. 78, no. 4, pp. 187–208, 2022.
[36] S. B. Hooker, *Second SeaWiFS HPLC analysis round-robin experiment (SeaHARRE-2)*. National Aeronautics and Space Administration, Goddard Space Flight Center, 2005, vol. 212785.
[37] H. R. Gordon and M. Wang, "Retrieval of water-leaving radiance and aerosol optical thickness over the oceans with seawifs: a preliminary algorithm," *Appl. Opt.*, vol. 33, no. 3, pp. 443–452, Jan 1994. [Online]. Available: http://ao.osa.org/abstract.cfm?URI=ao-33-3-443
[38] C. Mobley *et al.*, "The oceanic optics book," 2022.
[39] C. D. Mobley, L. K. Sundman, C. O. Davis, J. H. Bowles, T. V. Downes, R. A. Leathers, M. J. Montes, W. P. Bissett, D. D. Kohler, R. P. Reid *et al.*, "Interpretation of hyperspectral remote-sensing imagery by spectrum matching and look-up tables," *Applied Optics*, vol. 44, no. 17, pp. 3576–3592, 2005.
[40] Q. Vanhellemont, "Sensitivity analysis of the dark spectrum fitting atmospheric correction for metre-and decametre-scale satellite imagery using autonomous hyperspectral radiometry," *Optics Express*, vol. 28, no. 20, pp. 29 948–29 965, 2020.
[41] Q. Vanhellemont and K. Ruddick, "Atmospheric correction of metre-scale optical satellite data for inland and coastal water applications," *Remote sensing of environment*, vol. 216, pp. 586–597, 2018.
[42] K. P. Klein, H. Lantuit, B. Heim, D. Doxaran, B. Juhls, I. Nitze, D. Walch, A. Poste, and J. E. Søreide, "The arctic nearshore turbidity algorithm (anta)-a multi sensor turbidity algorithm for arctic nearshore environments," *Science of Remote Sensing*, vol. 4, p. 100036, 2021.
[43] B. Markham, J. Barsi, G. Kvaran, L. Ong, E. Kaita, S. Biggar, J. Czapla-Myers, N. Mishra, and D. Helder, "Landsat-8 operational land imager radiometric calibration and stability," *Remote Sensing*, vol. 6, no. 12, pp. 12 275–12 308, 2014.
[44] J. R. Schott, A. Gerace, C. E. Woodcock, S. Wang, Z. Zhu, R. H. Wynne, and C. E. Blinn, "The impact of improved signal-to-noise ratios on algorithm performance: Case studies for landsat class instruments," *Remote Sensing of Environment*, vol. 185, pp. 37–45, 2016.
[45] K. Blix, J. Li, P. Massicotte, and A. Matsuoka, "Developing a new machine-learning algorithm for estimating chlorophyll-a concentration in optically complex waters: A case study for high northern latitude waters by using sentinel 3 olci," *Remote Sensing*, vol. 11, no. 18, p. 2076, 2019.
[46] J. E. O'Reilly and P. J. Werdell, "Chlorophyll algorithms for ocean color sensors-oc4, oc5 & oc6," *Remote sensing of environment*, vol. 229, pp. 32–47, 2019.
[47] J. Chen, W.-N. Zhu, Y. Q. Tian, and Q. Yu, "Estimation of colored dissolved organic matter from landsat-8 imagery for complex inland water: case study of lake huron," *IEEE Transactions on Geoscience and Remote Sensing*, vol. 55, no. 4, pp. 2201–2212, 2017.
[48] R. Chastain, I. Housman, J. Goldstein, M. Finco, and K. Tenneson, "Empirical cross sensor comparison of sentinel-2a and 2b msi, landsat-8 oli, and landsat-7 etm+ top of atmosphere spectral characteristics over the conterminous united states," *Remote sensing of environment*, vol. 221, pp. 274–285, 2019.

10

Conclusions

The main study area of this thesis is the Barents Sea, which is the northernmost shelf sea in the world and supports 40% of its total primary productivity. The Barents Sea is home to Norway's most lucrative fishing industry and is also an important region due to its reserves of petroleum and natural gas. As a result of ongoing climate changes, the Barents Sea is experiencing significant changes in its ecosystem function and net primary productivity. Optical satellite sensors can be used to monitor these changes. However, it is frequently covered with clouds and experiences polar nights in the winter, which hinders the application of OC remote sensing. This thesis proposes and analyzes novel remote sensing methods to increase the frequency of high-resolution OC observations allowing for better monitoring of ecosystem function and the biogeochemical changes occurring in the Barents Sea. It presents novel, robust OC methods, and algorithms to better estimate WQIs from remotely sensed optical data compared to those in the literature. The algorithms presented in this thesis are globally applicable and validated in different water types. To achieve an increased frequency of high-resolution OC observations, we combined data from the Landsat 8 OLI and the Sentinel 2A/B MSI sensors, by developing a spectral harmonization method to allow for a consistent retrieval of Chl-a and CDOM products from OLI and MSI-derived R_{rs} using a single algorithm.

The Chl-a data used in this study was provided by the Norwegian Institute of Marine Research (IMR). The data was collected over a wide area of the Barents Sea and the Norwegian coast between the years 2016 and 2018 as part

of the IMR Ecosystem Program. Different match-up dataset creation methods were investigated for the retrieval of Chl-a from remotely sensed data. Our analysis indicates that depth-integrated Chl-a is more sensitive to satellite-derived R_{rs} products for the Barents Sea. To better tune the regression models, a new spatial window-based match-up dataset creation method was proposed to increase the number of match-ups. We demonstrated that the proposed match-up creation scheme has improved the performance of the Chl-a retrieval algorithms. In addition to that, an NN-based model, the OCN was also proposed. Our results indicate that the proposed OCN produced realistic Chl-a products in the study region compared to existing ML-based techniques, including the GPR, the regionally tuned empirical techniques, including the OCx algorithm and the spectral band ratios, as well as the globally trained C2RCC-nets. The proposed model was also validated on global inland, coastal and open waters for estimating Chl-a and CDOM concentrations using OLI and MSI images.

To find the top-performing AC processor for the Barents Sea, we collected ship-based above-water R_{rs} measurements using TRIOS RAMSES sensors, covering a large part of the Barents Sea which has not been explored before. We compared sentinel-2A/B and Landsat-8 derived R_{rs} processed through Acolite, C2RCC, OC-SMART, ICOR and Polymer against the in-situ R_{rs}, both in open ocean and the coastal regions of the Barents Sea. Our analysis demonstrates that the Acolite retrived R_{rs} are in good agreement with the in-situ R_{rs} observations, especially in the blue-green bands. The MAPD was found $< 14\%$ compared to $\sim 23\%$ and $\sim 25\%$ using C2RCC and Polymer. The present version of OC-SMART masked both OLI and MSI scenes at land pixels at latitudes $> 75N^{\circ}$, therefor those results are not included in this thesis. Similarly, ICOR was originally developed for coastal waters, failed to estimate AOT from the match-up scenes (both OLI and MSI) and was therefore not included in the AC analysis for the Barents Sea region. Over global waters, OC-SMART showed the minimum deviation from in-situ observations, with MAPD $< 30\%$ across the visible bands, indicating consistent performance over different water types.

ML-based algorithms have previously been widely used for WQ retrieval, however, the ML-based algorithms need an extensive amount of training examples. In this thesis, we attempt to harmonize OLI and MSI images to increase the frequency of OC observations and, hence, increase the satellite match-ups with in-situ observations to better tune the regression models. To do this, we evaluated the spectral consistency between near-simultaneous OLI and MSI overpasses with a time difference of less than 30 minutes in terms of TOA reflectance (ρ_t), and R_{rs} over the Barents Sea region. Our analysis suggests that ρ_t products of OLI and MSI are consistent in the visible as well as in the NIR channel ($< 4\%$). However, significant differences were observed in OLI-MSI R_{rs} products retrieved via Acolite, C2RCC, and Polymer. Results indicate that, OLI-MSI R_{rs} products via Acolite outperformed other methods and are

estimated to range from 8 to 15% in the common visible bands. To further minimize the spectral differences in the R_{rs} products, an NN-based model was developed to spectrally adjust the S2-A/B radiometry to replicate the spectral bandpasses of OLI for the common bands. After applying the proposed BA model, the spectral difference was significantly reduced from <10% to 2% (relative to 6-12% without any spectral adjustment), indicating the effectiveness of the BA for MSI imagery.

In Paper III, we harmonize OLI and MSI aquatic reflectance (ρ_w) products using the proposed BA model to acquire more match-ups (OLI and BA MSI (MSI*) combined), and hence better tune the retrieval models. The combined OLI and MSI* ρ_w products were combined in a single dataset and used for training and validation of the Chl-a and CDOM retrieval algorithms, including the OCN, GPR, and band ratio-based models. The performance of WQ retrieval models was evaluated in three different settings, i) using OLI data alone, ii) combined OLI-MSI data and iii) using combined OLI and MSI* data. The Chl-a retrieval analysis indicates that using the proposed OLI-MSI* data, improved the performance of the OCN by 41%, GPR by 21% and OCx by 27% in terms of mean absolute error compared to the OLI match-ups. Similarly, all the algorithms yielded a reduced root mean square difference in CDOM retrievals using the purposed OLI-MSI* data. In addition, we demonstrated that the BA model proposed in Paper II is generic and applicable to global waters. Our results show that after BA, the averaged spectral difference was significantly reduced from 21% to <5% in the common bands of OLI and MSI.

10.1 Future Work

In this work, five state-of-the-art AC processors, Acolite, Polymer, C2RCC, OC-SMART, and ICOR are validated against the in-situ R_{rs} observations. Future directions include validation of remaining AC processors, such as SeaDAS and MEETC2 [27], in order to derive an AC approach suitable for the Barents Sea. In Paper II, we evaluated the performance of AC processors using four MSI images; however, more field campaigns are required to increase the number of match-up scenes for a thorough performance comparison. Our AC validation results in Papers II and III demonstrate that research in this area is highly relevant and more effort is required to reduce uncertainties in the downstream data products, such as IOPs and water constituents. In this thesis, the performance of these processors is evaluated in terms of spectral consistency in the R_{rs} products between OLI and MSI only. Future research should compare the spectral consistency of R_{rs} products derived from MSI-OLCI and MSI-Landsat-9.

For the Barents Sea, only Chl-a data was collected to train the OCN model. To investigate the source of error in the retrieval of WQ indicators, other WQIs, CDOM, and TSM, should be collected simultaneously along with the radiometric data. The OCN implementation should be extended to simultaneously estimate other WQIs, such as TSM and CDOM. Additionally, it is important to investigate the correlation between optically active (such as Chl-a, CDOM, and TSM) and non-optically active water components, as well as the use of OCN to extract these in-active water constituents utilizing R_{rs}, WQIs as input features.

In this work, we have proposed an MLP-based model for spectral alignment of OLI-MSI R_{rs} products. The MLP considers each pixel individually and does not utilize the spatial relationship between the pixels in an image. In addition, the entire image is vectorized, treating it as one long feature vector, thereby retaining some spatial relations. However, this limits its applicability to small-sized images. Future work will include exploring the capability of CNNs in spectral harmonization of data products from multi-sensor missions. This may reduce the dependency of a network on the performance of AC algorithms. In addition, in Paper II and Paper III, we performed patch-wise training of the BA model. The inter-comparison OLI-MSI pixels were randomly split into 80% training samples and 20% test samples using 5-fold cross-validation. Future work should explore image-based training and testing of the BA model, i.e., the BA will be trained and tested on inter-comparison OLI-MSI images instead of patches.

Bibliography

[1] M. Reigstad, J. Carroll, D. Slagstad, I. Ellingsen, and P. Wassmann, "Intra-regional comparison of productivity, carbon flux and ecosystem composition within the northern barents sea," *Progress in Oceanography*, vol. 90, no. 1-4, pp. 33–46, 2011.

[2] P. Wassmann, M. Reigstad, T. Haug, B. Rudels, M. L. Carroll, H. Hop, G. W. Gabrielsen, S. Falk-Petersen, S. G. Denisenko, E. Arashkevich *et al.*, "Food webs and carbon flux in the barents sea," *Progress in Oceanography*, vol. 71, no. 2-4, pp. 232–287, 2006.

[3] E. Sakshaug, "Primary and secondary production in the arctic seas," in *The organic carbon cycle in the Arctic Ocean*. Springer, 2004, pp. 57–81.

[4] H. Loeng, "Features of the physical oceanographic conditions of the barents sea," *Polar research*, vol. 10, no. 1, pp. 5–18, 1991.

[5] Ø. Skagseth, T. Eldevik, M. Årthun, H. Asbjørnsen, V. S. Lien, and L. H. Smedsrud, "Reduced efficiency of the barents sea cooling machine," *Nature Climate Change*, pp. 1–6, 2020.

[6] Ø. Skagseth, K. F. Drinkwater, and E. Terrile, "Wind-and buoyancy-induced transport of the norwegian coastal current in the barents sea," *Journal of Geophysical Research: Oceans*, vol. 116, no. C8, 2011.

[7] M. Reigstad, T. Eldevik, and S. Gerland, "The nansen legacy," *The Nansen Legacy Report Series*, no. 24, 2021.

[8] M. Årthun, T. Eldevik, L. Smedsrud, Ø. Skagseth, and R. Ingvaldsen, "Quantifying the influence of atlantic heat on barents sea ice variability and retreat," *Journal of Climate*, vol. 25, no. 13, pp. 4736–4743, 2012.

[9] P. Dalpadado, K. R. Arrigo, G. L. van Dijken, H. R. Skjoldal, E. Bagøien, A. Dolgov, I. Prokopchuk, and E. Sperfeld, "Climate effects on temporal and spatial dynamics of phytoplankton and zooplankton in the barents

sea," *Progress in Oceanography*, p. 102320, 2020.

[10] Y. Huot, M. Babin, F. Bruyant, C. Grob, M. Twardowski, and H. Claustre, "Relationship between photosynthetic parameters and different proxies of phytoplankton biomass in the subtropical ocean," *Biogeosciences*, vol. 4, no. 5, pp. 853–868, 2007.

[11] C. J. Gobler, "Climate change and harmful algal blooms: Insights and perspective," *Harmful Algae*, vol. 91, p. 101731, 2020.

[12] N. Pahlevan, B. Smith, J. Schalles, C. Binding, Z. Cao, R. Ma, K. Alikas, K. Kangro, D. Gurlin, N. Hà *et al.*, "Seamless retrievals of chlorophyll-a from sentinel-2 (msi) and sentinel-3 (olci) in inland and coastal waters: A machine-learning approach," *Remote Sensing of Environment*, p. 111604, 2020.

[13] N. Pahlevan, B. Smith, K. Alikas, J. Anstee, C. Barbosa, C. Binding, M. Bresciani, B. Cremella, C. Giardino, D. Gurlin *et al.*, "Simultaneous retrieval of selected optical water quality indicators from landsat-8, sentinel-2, and sentinel-3," *Remote Sensing of Environment*, vol. 270, p. 112860, 2022.

[14] A. Matsuoka, J. W. Campbell, S. B. Hooker, F. Steinmetz, K. Ogata, T. Hirata, H. Higa, V. S. Kuwahara, T. Isada, K. Suzuki *et al.*, "Performance of jaxa's sgli standard ocean color products for oceanic to coastal waters: chlorophyll a concentration and light absorption coefficients of colored dissolved organic matter," *Journal of Oceanography*, vol. 78, no. 4, pp. 187–208, 2022.

[15] C. Kuhn, A. de Matos Valerio, N. Ward, L. Loken, H. O. Sawakuchi, M. Kampel, J. Richey, P. Stadler, J. Crawford, R. Striegl *et al.*, "Performance of landsat-8 and sentinel-2 surface reflectance products for river remote sensing retrievals of chlorophyll-a and turbidity," *Remote Sensing of Environment*, vol. 224, pp. 104–118, 2019.

[16] C. D. Mobley, *Light and water: radiative transfer in natural waters*. Academic press, 1994.

[17] D. Blondeau-Patissier, J. F. Gower, A. G. Dekker, S. R. Phinn, and V. E. Brando, "A review of ocean color remote sensing methods and statistical techniques for the detection, mapping and analysis of phytoplankton blooms in coastal and open oceans," *Progress in oceanography*, vol. 123, pp. 123–144, 2014.

[18] E. Novo, J. Hansom, and P. Curran, "The effect of sediment type on the re-

lationship between reflectance and suspended sediment concentration," *Remote Sensing*, vol. 10, no. 7, pp. 1283–1289, 1989.

[19] R. P. Bukata, J. H. Jerome, K. Y. Kondratyev, and D. V. Pozdnyakov, *Optical properties and remote sensing of inland and coastal waters*. CRC press, 2018.

[20] R. Smith and K. Baker, "Oceanic chlorophyll concentrations as determined by satellite (nimbus-7 coastal zone color scanner)," *Marine Biology*, vol. 66, no. 3, pp. 269–279, 1982.

[21] K. Blix, J. Li, P. Massicotte, and A. Matsuoka, "Developing a new machine-learning algorithm for estimating chlorophyll-a concentration in optically complex waters: A case study for high northern latitude waters by using sentinel 3 olci," *Remote Sensing*, vol. 11, no. 18, p. 2076, 2019.

[22] A. A. Gilerson, A. A. Gitelson, J. Zhou, D. Gurlin, W. Moses, I. Ioannou, and S. A. Ahmed, "Algorithms for remote estimation of chlorophyll-a in coastal and inland waters using red and near infrared bands," *Optics Express*, vol. 18, no. 23, pp. 24 109–24 125, 2010.

[23] S. Mishra and D. R. Mishra, "Normalized difference chlorophyll index: A novel model for remote estimation of chlorophyll-a concentration in turbid productive waters," *Remote Sensing of Environment*, vol. 117, pp. 394–406, 2012.

[24] D. Odermatt, A. Gitelson, V. E. Brando, and M. Schaepman, "Review of constituent retrieval in optically deep and complex waters from satellite imagery," *Remote sensing of environment*, vol. 118, pp. 116–126, 2012.

[25] J. Wang, Z. Lee, D. Wang, S. Shang, J. Wei, and A. Gilerson, "Atmospheric correction over coastal waters with aerosol properties constrained by multi-pixel observations," *Remote Sensing of Environment*, vol. 265, p. 112633, 2021.

[26] M. A. Warren, S. G. Simis, V. Martinez-Vicente, K. Poser, M. Bresciani, K. Alikas, E. Spyrakos, C. Giardino, and A. Ansper, "Assessment of atmospheric correction algorithms for the sentinel-2a multispectral imager over coastal and inland waters," *Remote sensing of environment*, vol. 225, pp. 267–289, 2019.

[27] N. Pahlevan, A. Mangin, S. V. Balasubramanian, B. Smith, K. Alikas, K. Arai, C. Barbosa, S. Bélanger, C. Binding, M. Bresciani *et al.*, "Acix-aqua: A global assessment of atmospheric correction methods for landsat-8

and sentinel-2 over lakes, rivers, and coastal waters," *Remote Sensing of Environment*, vol. 258, p. 112366, 2021.

[28] S. Bélanger, J. K. Ehn, and M. Babin, "Impact of sea ice on the retrieval of water-leaving reflectance, chlorophyll a concentration and inherent optical properties from satellite ocean color data," *Remote Sensing of Environment*, vol. 111, no. 1, pp. 51–68, 2007.

[29] N. Pahlevan, S. K. Chittimalli, S. V. Balasubramanian, and V. Vellucci, "Sentinel-2/landsat-8 product consistency and implications for monitoring aquatic systems," *Remote sensing of Environment*, vol. 220, pp. 19–29, 2019.

[30] J. Li and D. P. Roy, "A global analysis of sentinel-2a, sentinel-2b and landsat-8 data revisit intervals and implications for terrestrial monitoring," *Remote Sensing*, vol. 9, no. 9, p. 902, 2017.

[31] D. Scheffler, D. Frantz, and K. Segl, "Spectral harmonization and red edge prediction of landsat-8 to sentinel-2 using land cover optimized multivariate regressors," *Remote Sensing of Environment*, vol. 241, p. 111723, 2020.

[32] M. Claverie, J. Ju, J. G. Masek, J. L. Dungan, E. F. Vermote, J.-C. Roger, S. V. Skakun, and C. Justice, "The harmonized landsat and sentinel-2 surface reflectance data set," *Remote sensing of environment*, vol. 219, pp. 145–161, 2018.

[33] S. Hafeez *et al.*, "Integrating remote sensing and machine learning technologies for coastal water quality monitoring in hong kong and the pearl river estuary," 2022.

[34] H. Loisel and A. Morel, "Light scattering and chlorophyll concentration in case 1 waters: A reexamination," *Limnology and Oceanography*, vol. 43, no. 5, pp. 847–858, 1998.

[35] H. R. Gordon, D. K. Clark, J. W. Brown, O. B. Brown, R. H. Evans, and W. W. Broenkow, "Phytoplankton pigment concentrations in the middle atlantic bight: comparison of ship determinations and czcs estimates," *Applied optics*, vol. 22, no. 1, pp. 20–36, 1983.

[36] S. Jain and J. Miller, "Subsurface water parameters: optimization approach to their determination from remotely sensed water color data," *Applied optics*, vol. 15, no. 4, pp. 886–890, 1976.

[37] N. Pahlevan, B. Smith, C. Binding, and D. O'Donnell, "Spectral band adjustments for remote sensing reflectance spectra in coastal/inland waters," *Optics Express*, vol. 25, no. 23, pp. 28 650–28 667, 2017.

[38] IOCCG, "Mission requirements for future ocean-colour sensors," 2012.

[39] S. Hafeez, M. S. Wong, H. C. Ho, M. Nazeer, J. Nichol, S. Abbas, D. Tang, K. H. Lee, and L. Pun, "Comparison of machine learning algorithms for retrieval of water quality indicators in case-ii waters: a case study of hong kong," *Remote Sensing*, vol. 11, no. 6, p. 617, 2019.

[40] G. Liu, L. Li, K. Song, Y. Li, H. Lyu, Z. Wen, C. Fang, S. Bi, X. Sun, Z. Wang *et al.*, "An olci-based algorithm for semi-empirically partitioning absorption coefficient and estimating chlorophyll a concentration in various turbid case-2 waters," *Remote Sensing of Environment*, vol. 239, p. 111648, 2020.

[41] P. J. Werdell and S. W. Bailey, "An improved in-situ bio-optical data set for ocean color algorithm development and satellite data product validation," *Remote sensing of environment*, vol. 98, no. 1, pp. 122–140, 2005.

[42] W. Hou, K. Carder, and D. Costello, "Coastal bottom feature classification using 2-d and 3-d moment invariants," *Proc. Ocean Optics XVI, Sante Fe, New Mexico*, 2002.

[43] J. E. O'Reilly and P. J. Werdell, "Chlorophyll algorithms for ocean color sensors-oc4, oc5 & oc6," *Remote sensing of environment*, vol. 229, pp. 32–47, 2019.

[44] M. Asim, C. Brekke, A. Mahmood, T. Eltoft, and M. Reigstad, "Improving chlorophyll-a estimation from sentinel-2 (msi) in the barents sea using machine learning," *IEEE Journal of Selected Topics in Applied Earth Observations and Remote Sensing*, 2021.

[45] Z. Lee, K. L. Carder, and R. A. Arnone, "Deriving inherent optical properties from water color: a multiband quasi-analytical algorithm for optically deep waters," *Applied optics*, vol. 41, no. 27, pp. 5755–5772, 2002.

[46] W. Yang, B. Matsushita, J. Chen, and T. Fukushima, "Estimating constituent concentrations in case ii waters from meris satellite data by semi-analytical model optimizing and look-up tables," *Remote Sensing of Environment*, vol. 115, no. 5, pp. 1247–1259, 2011.

[47] C. D. Mobley, J. Werdell, B. Franz, Z. Ahmad, and S. Bailey, "Atmospheric correction for satellite ocean color radiometry," 2016.

[48] K. Cheng, S. N. Chan, and J. H. Lee, "Remote sensing of coastal algal blooms using unmanned aerial vehicles (uavs)," *Marine Pollution Bulletin*, vol. 152, p. 110889, 2020.

[49] S. B. Hooker, G. Lazin, G. Zibordi, and S. McLean, "An evaluation of above-and in-water methods for determining water-leaving radiances," *Journal of Atmospheric and Oceanic Technology*, vol. 19, no. 4, pp. 486–515, 2002.

[50] N. Pahlevan, S. Sarkar, B. Franz, S. Balasubramanian, and J. He, "Sentinel-2 multispectral instrument (msi) data processing for aquatic science applications: Demonstrations and validations," *Remote sensing of environment*, vol. 201, pp. 47–56, 2017.

[51] C. R. McClain, G. Meister *et al.*, "Mission requirements for future ocean-colour sensors." 2012.

[52] R. E. O'Shea, S. R. Laney, and Z. Lee, "Evaluation of glint correction approaches for fine-scale ocean color measurements by lightweight hyperspectral imaging spectrometers," *Applied Optics*, vol. 59, no. 7, pp. B18–B34, 2020.

[53] S. W. Bailey and P. J. Werdell, "A multi-sensor approach for the on-orbit validation of ocean color satellite data products," *Remote Sensing of Environment*, vol. 102, no. 1-2, pp. 12–23, 2006.

[54] C. R. McClain, "A decade of satellite ocean color observations," *Annual Review of Marine Science*, vol. 1, pp. 19–42, 2009.

[55] R. Shang and Z. Zhu, "Harmonizing landsat 8 and sentinel-2: A time-series-based reflectance adjustment approach," *Remote Sensing of Environment*, vol. 235, p. 111439, 2019.

[56] Q. Vanhellemont and K. Ruddick, "Acolite for sentinel-2: Aquatic applications of msi imagery," in *Proceedings of the 2016 ESA Living Planet Symposium, Prague, Czech Republic*, 2016, pp. 9–13.

[57] Z. Shao, J. Cai, P. Fu, L. Hu, and T. Liu, "Deep learning-based fusion of landsat-8 and sentinel-2 images for a harmonized surface reflectance product," *Remote Sensing of Environment*, vol. 235, p. 111425, 2019.

[58] P. G. Falkowski, E. A. Laws, R. T. Barber, and J. W. Murray, "Phytoplankton and their role in primary, new, and export production," in *Ocean biogeochemistry*. Springer, 2003, pp. 99–121.

[59] B. W. Brooks, J. M. Lazorchak, M. D. Howard, M.-V. V. Johnson, S. L. Morton, D. A. Perkins, E. D. Reavie, G. I. Scott, S. A. Smith, and J. A. Steevens, "Are harmful algal blooms becoming the greatest inland water quality threat to public health and aquatic ecosystems?" *Environmental toxicology and chemistry*, vol. 35, no. 1, pp. 6–13, 2016.

[60] O. Abirhire, R. L. North, K. Hunter, D. Vandergucht, and J. Hudson, "Do human activities affect phytoplankton biomass and composition in embayments on lake diefenbaker?" *Journal of Freshwater Ecology*, vol. 31, no. 4, pp. 597–608, 2016.

[61] D. M. Anderson, "The growing problem of harmful algae," *Oceanus*, vol. 43, no. 1, pp. 1–5, 2004.

[62] Z. Cao, R. Ma, H. Duan, N. Pahlevan, J. Melack, M. Shen, and K. Xue, "A machine learning approach to estimate chlorophyll-a from landsat-8 measurements in inland lakes," *Remote Sensing of Environment*, vol. 248, p. 111974, 2020.

[63] W. Zhou, J. Gao, J. Liao, R. Shi, T. Li, Y. Guo, and A. Long, "Characteristics of phytoplankton biomass, primary production and community structure in the modaomen channel, pearl river estuary, with special reference to the influence of saltwater intrusion during neap and spring tides," *Plos one*, vol. 11, no. 12, p. e0167630, 2016.

[64] A. Morel *et al.*, "Minimum requirements for an operational, ocean-colour sensor for the open ocean." 1998.

[65] J. Gower, S. King, G. Borstad, and L. Brown, "Detection of intense plankton blooms using the 709 nm band of the meris imaging spectrometer," *International Journal of Remote Sensing*, vol. 26, no. 9, pp. 2005–2012, 2005.

[66] M. W. Matthews, S. Bernard, and L. Robertson, "An algorithm for detecting trophic status (chlorophyll-a), cyanobacterial-dominance, surface scums and floating vegetation in inland and coastal waters," *Remote Sensing of Environment*, vol. 124, pp. 637–652, 2012.

[67] H. J. Gons, "Optical teledetection of chlorophyll a in turbid inland waters," *Environmental science & technology*, vol. 33, no. 7, pp. 1127–1132, 1999.

[68] A. Gitelson, "The peak near 700 nm on radiance spectra of algae and water: relationships of its magnitude and position with chlorophyll concentration," *International Journal of Remote Sensing*, vol. 13, no. 17, pp. 3367–3373, 1992.

[69] S. Hafeez, M. S. Wong, S. Abbas, C. Y. Kwok, J. Nichol, K. H. Lee, D. Tang, and L. Pun, "Detection and monitoring of marine pollution using remote sensing technologies," *Monitoring of Marine Pollution*, 2018.

[70] A. Morel, H. Claustre, D. Antoine, and B. Gentili, "Natural variability of bio-optical properties in case 1 waters: attenuation and reflectance within the visible and near-uv spectral domains, as observed in south pacific and mediterranean waters," *Biogeosciences*, vol. 4, no. 5, pp. 913–925, 2007.

[71] A. Morel and J.-F. Berthon, "Surface pigments, algal biomass profiles, and potential production of the euphotic layer: Relationships reinvestigated in view of remote-sensing applications," *Limnology and oceanography*, vol. 34, no. 8, pp. 1545–1562, 1989.

[72] K. Toming, T. Kutser, R. Uiboupin, A. Arikas, K. Vahter, and B. Paavel, "Mapping water quality parameters with sentinel-3 ocean and land colour instrument imagery in the baltic sea," *Remote Sensing*, vol. 9, no. 10, p. 1070, 2017.

[73] Y. Shang, G. Liu, Z. Wen, P.-A. Jacinthe, K. Song, B. Zhang, L. Lyu, S. Li, X. Wang, and X. Yu, "Remote estimates of cdom using sentinel-2 remote sensing data in reservoirs with different trophic states across china," *Journal of Environmental Management*, vol. 286, p. 112275, 2021.

[74] J. Xu, C. Fang, D. Gao, H. Zhang, C. Gao, Z. Xu, and Y. Wang, "Optical models for remote sensing of chromophoric dissolved organic matter (cdom) absorption in poyang lake," *ISPRS journal of photogrammetry and remote sensing*, vol. 142, pp. 124–136, 2018.

[75] S. Koizumi, N. Craig, J. A. Zwart, P. T. Kelly, J. P. Ziegler, B. C. Weidel, S. E. Jones, and C. T. Solomon, "Experimental whole-lake dissolved organic carbon increase alters fish diet and density but not growth or productivity," *Canadian journal of fisheries and aquatic sciences*, vol. 75, no. 11, pp. 1859–1867, 2018.

[76] C. Nima, Ø. Frette, B. Hamre, J. J. Stamnes, Y.-C. Chen, K. Sørensen, M. Norli, D. Lu, Q. Xing, D. Muyimbwa *et al.*, "Cdom absorption properties of natural water bodies along extreme environmental gradients," *Water*,

vol. 11, no. 10, p. 1988, 2019.

[77] C. Mobley, "Light and water: Radiative transfer in natural waters can be downloaded from the publications page of the ocean optics web book."

[78] J. Chen, W.-N. Zhu, Y. Q. Tian, and Q. Yu, "Estimation of colored dissolved organic matter from landsat-8 imagery for complex inland water: case study of lake huron," *IEEE Transactions on Geoscience and Remote Sensing*, vol. 55, no. 4, pp. 2201–2212, 2017.

[79] S. V. Balasubramanian, N. Pahlevan, B. Smith, C. Binding, J. Schalles, H. Loisel, D. Gurlin, S. Greb, K. Alikas, M. Randla *et al.*, "Robust algorithm for estimating total suspended solids (tss) in inland and nearshore coastal waters," *Remote Sensing of Environment*, vol. 246, p. 111768, 2020.

[80] L. Sokoletsky, S. Fang, X. Yang, and X. Wei, "Evaluation of empirical and semianalytical spectral reflectance models for surface suspended sediment concentration in the highly variable estuarine and coastal waters of east china," *IEEE Journal of Selected Topics in Applied Earth Observations and Remote Sensing*, vol. 9, no. 11, pp. 5182–5192, 2016.

[81] K. Shi, Y. Li, L. Li, and H. Lu, "Absorption characteristics of optically complex inland waters: Implications for water optical classification," *Journal of Geophysical research: biogeosciences*, vol. 118, no. 2, pp. 860–874, 2013.

[82] M. A. Warren, S. G. Simis, and N. Selmes, "Complementary water quality observations from high and medium resolution sentinel sensors by aligning chlorophyll-a and turbidity algorithms," *Remote Sensing of Environment*, vol. 265, p. 112651, 2021.

[83] H. R. Gordon and M. Wang, "Retrieval of water-leaving radiance and aerosol optical thickness over the oceans with seawifs: a preliminary algorithm," *Appl. Opt.*, vol. 33, no. 3, pp. 443–452, Jan 1994. [Online]. Available: http://ao.osa.org/abstract.cfm?URI=ao-33-3-443

[84] D. Antoine and A. Morel, "A multiple scattering algorithm for atmospheric correction of remotely sensed ocean colour (meris instrument): principle and implementation for atmospheres carrying various aerosols including absorbing ones," *International Journal of Remote Sensing*, vol. 20, no. 9, pp. 1875–1916, 1999.

[85] C. D. Mobley, L. K. Sundman, C. O. Davis, J. H. Bowles, T. V. Downes, R. A. Leathers, M. J. Montes, W. P. Bissett, D. D. Kohler, R. P. Reid *et al.*,

"Interpretation of hyperspectral remote-sensing imagery by spectrum matching and look-up tables," *Applied Optics*, vol. 44, no. 17, pp. 3576–3592, 2005.

[86] M. Wang, "Atmospheric correction for remotely-sensed ocean-colour products," *Reports and Monographs of the International Ocean-Colour Coordinating Group (IOCCG)*, 2010.

[87] M. Babin, K. Arrigo, S. Bélanger, M.-H. Forget *et al.*, "Ocean colour remote sensing in polar seas." 2015.

[88] H. R. Gordon and M. Wang, "Retrieval of water-leaving radiance and aerosol optical thickness over the oceans with seawifs: a preliminary algorithm," *Applied optics*, vol. 33, no. 3, pp. 443–452, 1994.

[89] T. Harmel and M. Chami, "Influence of polarimetric satellite data measured in the visible region on aerosol detection and on the performance of atmospheric correction procedure over open ocean waters," *Optics Express*, vol. 19, no. 21, pp. 20 960–20 983, 2011.

[90] B. Bulgarelli, V. Kiselev, and G. Zibordi, "Simulation and analysis of adjacency effects in coastal waters: a case study," *Applied optics*, vol. 53, no. 8, pp. 1523–1545, 2014.

[91] N. Pahlevan, J.-C. Roger, and Z. Ahmad, "Revisiting short-wave-infrared (swir) bands for atmospheric correction in coastal waters," *Optics express*, vol. 25, no. 6, pp. 6015–6035, 2017.

[92] Z. Ahmad, B. A. Franz, C. R. McClain, E. J. Kwiatkowska, J. Werdell, E. P. Shettle, and B. N. Holben, "New aerosol models for the retrieval of aerosol optical thickness and normalized water-leaving radiances from the seawifs and modis sensors over coastal regions and open oceans," *Applied optics*, vol. 49, no. 29, pp. 5545–5560, 2010.

[93] A. Matsuoka, Y. Huot, K. Shimada, S.-I. Saitoh, and M. Babin, "Bio-optical characteristics of the western arctic ocean: implications for ocean color algorithms," *Canadian Journal of Remote Sensing*, vol. 33, no. 6, pp. 503–518, 2007.

[94] Z. Malenovský, H. Rott, J. Cihlar, M. E. Schaepman, G. García-Santos, R. Fernandes, and M. Berger, "Sentinels for science: Potential of sentinel-1, -2, and -3 missions for scientific observations of ocean, cryosphere, and land," *Remote Sensing of Environment*, vol. 120, pp. 91–101, 2012, the Sentinel Missions - New Opportunities for Science.

[Online]. Available: https://www.sciencedirect.com/science/article/pii/S0034425712000648

[95] J. C. Comiso, D. Perovich, K. Stamnes, and V. Stuart, "Ioccg report number 16, 2015 ocean colour remote sensing in polar seas. chapter 2; the polar environment: Sun, clouds, and ice," 2015.

[96] C. Brockmann, R. Doerffer, M. Peters, S. Kerstin, S. Embacher, and A. Ruescas, "Evolution of the c2rcc neural network for sentinel 2 and 3 for the retrieval of ocean colour products in normal and extreme optically complex waters," in *Living Planet Symposium*, vol. 740, 2016, p. 54.

[97] Y. Fan, W. Li, N. Chen, J.-H. Ahn, Y.-J. Park, S. Kratzer, T. Schroeder, J. Ishizaka, R. Chang, and K. Stamnes, "Oc-smart: A machine learning based data analysis platform for satellite ocean color sensors," *Remote Sensing of Environment*, vol. 253, p. 112236, 2021.

[98] F. Steinmetz, P.-Y. Deschamps, and D. Ramon, "Atmospheric correction in presence of sun glint: application to meris," *Optics express*, vol. 19, no. 10, pp. 9783–9800, 2011.

[99] M. Main-Knorn, B. Pflug, J. Louis, V. Debaecker, U. Müller-Wilm, and F. Gascon, "Sen2cor for sentinel-2," in *Image and Signal Processing for Remote Sensing XXIII*, vol. 10427. International Society for Optics and Photonics, 2017, p. 1042704.

[100] Q. Vanhellemont and K. Ruddick, "Turbid wakes associated with offshore wind turbines observed with landsat 8," *Remote Sensing of Environment*, vol. 145, pp. 105–115, 2014.

[101] Q. Vanhellemont, "Adaptation of the dark spectrum fitting atmospheric correction for aquatic applications of the landsat and sentinel-2 archives," *Remote Sensing of Environment*, vol. 225, pp. 175–192, 2019.

[102] L. De Keukelaere, S. Sterckx, S. Adriaensen, E. Knaeps, I. Reusen, C. Giardino, M. Bresciani, P. Hunter, C. Neil, D. Van der Zande *et al.*, "Atmospheric correction of landsat-8/oli and sentinel-2/msi data using icor algorithm: validation for coastal and inland waters," *European Journal of Remote Sensing*, vol. 51, no. 1, pp. 525–542, 2018.

[103] Q. Vanhellemont, "Sensitivity analysis of the dark spectrum fitting atmospheric correction for metre-and decametre-scale satellite imagery using autonomous hyperspectral radiometry," *Optics Express*, vol. 28, no. 20, pp. 29 948–29 965, 2020.

[104] Z. Lee, K. L. Carder, R. Steward, T. Peacock, C. Davis, and J. Patch, "An empirical algorithm for light absorption by ocean water based on color," *Journal of Geophysical Research: Oceans*, vol. 103, no. C12, pp. 27 967–27 978, 1998.

[105] K. G. Ruddick, H. J. Gons, M. Rijkeboer, and G. Tilstone, "Optical remote sensing of chlorophyll a in case 2 waters by use of an adaptive two-band algorithm with optimal error properties," *Applied optics*, vol. 40, no. 21, pp. 3575–3585, 2001.

[106] A. A. Gitelson, G. Dall'Olmo, W. Moses, D. C. Rundquist, T. Barrow, T. R. Fisher, D. Gurlin, and J. Holz, "A simple semi-analytical model for remote estimation of chlorophyll-a in turbid waters: Validation," *Remote Sensing of Environment*, vol. 112, no. 9, pp. 3582–3593, 2008.

[107] C. Le, C. Hu, D. English, J. Cannizzaro, and C. Kovach, "Climate-driven chlorophyll-a changes in a turbid estuary: Observations from satellites and implications for management," *Remote Sensing of Environment*, vol. 130, pp. 11 – 24, 2013. [Online]. Available: http://www.sciencedirect.com/science/article/pii/S0034425712004439

[108] S. Sathyendranath *et al.*, "Remote sensing of ocean colour in coastal, and other optically-complex, waters." 2000.

[109] C. S. Yentsch, "The influence of phytoplankton pigments on the colour of sea water," *Deep Sea Research (1953)*, vol. 7, no. 1, pp. 1–9, 1960.

[110] J. E. O'Reilly, S. Maritorena, B. G. Mitchell, D. A. Siegel, K. L. Carder, S. A. Garver, M. Kahru, and C. McClain, "Ocean color chlorophyll algorithms for seawifs," *Journal of Geophysical Research: Oceans*, vol. 103, no. C11, pp. 24 937–24 953, 1998.

[111] X.-G. Xing, D.-Z. Zhao, Y.-G. Liu, J.-H. Yang, P. Xiu, and L. Wang, "An overview of remote sensing of chlorophyll fluorescence," *Ocean Science Journal*, vol. 42, no. 1, pp. 49–59, 2007.

[112] M. W. Matthews and D. Odermatt, "Improved algorithm for routine monitoring of cyanobacteria and eutrophication in inland and near-coastal waters," *Remote Sensing of Environment*, vol. 156, pp. 374–382, 2015.

[113] D. Gurlin, A. A. Gitelson, and W. J. Moses, "Remote estimation of chl-a concentration in turbid productive waters—return to a simple two-band nir-red model?" *Remote Sensing of Environment*, vol. 115, no. 12, pp.

3479–3490, 2011.

[114] M. Moradi and K. Kabiri, "Spatio-temporal variability of red-green chlorophyll-a index from modis data–case study: Chabahar bay, se of iran," *Continental Shelf Research*, vol. 184, pp. 1–9, 2019.

[115] R. M. Letelier and M. R. Abbott, "An analysis of chlorophyll fluorescence algorithms for the moderate resolution imaging spectrometer (modis)," *Remote Sensing of Environment*, vol. 58, no. 2, pp. 215–223, 1996.

[116] J. Gower, R. Doerffer, and G. Borstad, "Interpretation of the 685nm peak in water-leaving radiance spectra in terms of fluorescence, absorption and scattering, and its observation by meris," *International Journal of Remote Sensing*, vol. 20, no. 9, pp. 1771–1786, 1999.

[117] C. Hu, Z. Lee, and B. Franz, "Chlorophyll aalgorithms for oligotrophic oceans: A novel approach based on three-band reflectance difference," *Journal of Geophysical Research: Oceans*, vol. 117, no. C1, 2012.

[118] M. E. Smith, L. R. Lain, and S. Bernard, "An optimized chlorophyll a switching algorithm for meris and olci in phytoplankton-dominated waters," *Remote Sensing of Environment*, vol. 215, pp. 217–227, 2018.

[119] L. E. Keiner and X.-H. Yan, "A neural network model for estimating sea surface chlorophyll and sediments from thematic mapper imagery," *Remote sensing of environment*, vol. 66, no. 2, pp. 153–165, 1998.

[120] G. Camps-Valls, L. Bruzzone, J. L. Rojo-Alvarez, and F. Melgani, "Robust support vector regression for biophysical variable estimation from remotely sensed images," *IEEE Geoscience and remote sensing letters*, vol. 3, no. 3, pp. 339–343, 2006.

[121] G. Camps-Valls, L. Gómez-Chova, J. Muñoz-Marí, J. Vila-Francés, J. Amorós-López, and J. Calpe-Maravilla, "Retrieval of oceanic chlorophyll concentration with relevance vector machines," *Remote Sensing of Environment*, vol. 105, no. 1, pp. 23–33, 2006.

[122] P. M. Maier, S. Hinz, and S. Keller, "Estimation of chlorophyll a, diatoms and green algae based on hyperspectral data with machine learning approaches," *Tagungsband der*, vol. 37, 2018.

[123] L. Pasolli, F. Melgani, and E. Blanzieri, "Gaussian process regression for estimating chlorophyll concentration in subsurface waters from remote sensing data," *IEEE Geoscience and Remote Sensing Letters*, vol. 7, no. 3,

pp. 464–468, 2010.

[124] J. Verrelst, J. Muñoz, L. Alonso, J. Delegido, J. P. Rivera, G. Camps-Valls, and J. Moreno, "Machine learning regression algorithms for biophysical parameter retrieval: Opportunities for sentinel-2 and-3," *Remote Sensing of Environment*, vol. 118, pp. 127–139, 2012.

[125] J. He, Y. Chen, J. Wu, D. A. Stow, and G. Christakos, "Space-time chlorophyll-a retrieval in optically complex waters that accounts for remote sensing and modeling uncertainties and improves remote estimation accuracy," *Water Research*, vol. 171, p. 115403, 2020.

[126] B. Smith, N. Pahlevan, J. Schalles, S. Ruberg, R. Errera, R. Ma, C. Giardino, M. Bresciani, C. Barbosa, T. Moore *et al.*, "A chlorophyll-a algorithm for landsat-8 based on mixture density networks," *Frontiers in Remote Sensing*, vol. 1, p. 623678, 2021.

[127] S. Javed, A. Mahmood, M. M. Fraz, N. A. Koohbanani, K. Benes, Y.-W. Tsang, K. Hewitt, D. Epstein, D. Snead, and N. Rajpoot, "Cellular community detection for tissue phenotyping in colorectal cancer histology images," *Medical Image Analysis*, p. 101696, 2020.

[128] S. Hansen, "Leveraging supervoxels for medical image volume segmentation with limited supervision," 2022.

[129] R. Awan, K. Benes, A. Azam, T.-H. Song, M. Shaban, C. Verrill, Y. W. Tsang, D. Snead, F. Minhas, and N. Rajpoot, "Deep learning based digital cell profiles for risk stratification of urine cytology images," *Cytometry Part A*, vol. 99, no. 7, pp. 732–742, 2021.

[130] E. J. Kwiatkowska and G. S. Fargion, "Application of machine-learning techniques toward the creation of a consistent and calibrated global chlorophyll concentration baseline dataset using remotely sensed ocean color data," *IEEE Transactions on Geoscience and Remote Sensing*, vol. 41, no. 12, pp. 2844–2860, 2003.

[131] H. K. Zhang, D. P. Roy, L. Yan, Z. Li, H. Huang, E. Vermote, S. Skakun, and J.-C. Roger, "Characterization of sentinel-2a and landsat-8 top of atmosphere, surface, and nadir brdf adjusted reflectance and ndvi differences," *Remote sensing of environment*, vol. 215, pp. 482–494, 2018.

[132] D. P. Roy, H. Zhang, J. Ju, J. L. Gomez-Dans, P. E. Lewis, C. Schaaf, Q. Sun, J. Li, H. Huang, and V. Kovalskyy, "A general method to normalize landsat reflectance data to nadir brdf adjusted reflectance," *Remote Sensing of*

Environment, vol. 176, pp. 255–271, 2016.

[133] K. T. Peterson, V. Sagan, and J. J. Sloan, "Deep learning-based water quality estimation and anomaly detection using landsat-8/sentinel-2 virtual constellation and cloud computing," *GIScience & Remote Sensing*, vol. 57, no. 4, pp. 510–525, 2020.

[134] J. Chen and W. Zhu, "Comparing landsat-8 and sentinel-2 top of atmosphere and surface reflectance in high latitude regions: case study in alaska," *Geocarto International*, pp. 1–20, 2021.

[135] R. Sedona, C. Paris, G. Cavallaro, L. Bruzzone, and M. Riedel, "A high-performance multispectral adaptation gan for harmonizing dense time series of landsat-8 and sentinel-2 images," *IEEE journal of selected topics in applied earth observations and remote sensing*, vol. 14, pp. 10 134–10 146, 2021.

[136] M. Asim, A. Matsuoka, P. G. Ellingsen, C. Brekke, T. Eltoft, and K. Blix, "A new spectral harmonization algorithm for landsat-8 and sentinel-2 remote sensing reflectance products using machine learning: a case study for the barents sea (european arctic)," *IEEE Transactions on Geoscience and Remote Sensing*, 2022.

[137] I. Goodfellow, Y. Bengio, and A. Courville, *Deep Learning*. MIT Press, 2016, http://www.deeplearningbook.org.

[138] E. J. Hartman, J. D. Keeler, and J. M. Kowalski, "Layered neural networks with gaussian hidden units as universal approximations," *Neural computation*, vol. 2, no. 2, pp. 210–215, 1990.

[139] A. Burkov, *The hundred-page machine learning book*. Andriy Burkov Quebec City, QC, Canada, 2019, vol. 1.

[140] A. Mahapatra, "Prediction of daily ground-level ozone concentration maxima over new delhi," *Environmental monitoring and assessment*, vol. 170, no. 1, pp. 159–170, 2010.

[141] R. Gençay and M. Qi, "Pricing and hedging derivative securities with neural networks: Bayesian regularization, early stopping, and bagging," *IEEE Transactions on Neural Networks*, vol. 12, no. 4, pp. 726–734, 2001.

[142] N. Srivastava, G. Hinton, A. Krizhevsky, I. Sutskever, and R. Salakhutdinov, "Dropout: a simple way to prevent neural networks from overfitting," *The journal of machine learning research*, vol. 15, no. 1, pp. 1929–1958,

2014.

[143] C. Shorten and T. M. Khoshgoftaar, "A survey on image data augmentation for deep learning," *Journal of big data*, vol. 6, no. 1, pp. 1–48, 2019.

[144] F. L. de la Rosa, J. L. Gómez-Sirvent, R. Sánchez-Reolid, R. Morales, and A. Fernández-Caballero, "Geometric transformation-based data augmentation on defect classification of segmented images of semiconductor materials using a resnet50 convolutional neural network," *Expert Systems with Applications*, p. 117731, 2022.

[145] S. Ioffe and C. Szegedy, "Batch normalization: Accelerating deep network training by reducing internal covariate shift," *arXiv preprint arXiv:1502.03167*, 2015.

[146] C. D. Mobley, "Estimation of the remote-sensing reflectance from above-surface measurements," *Applied optics*, vol. 38, no. 36, pp. 7442–7455, 1999.

[147] K. G. Ruddick, V. De Cauwer, Y.-J. Park, and G. Moore, "Seaborne measurements of near infrared water-leaving reflectance: The similarity spectrum for turbid waters," *Limnology and Oceanography*, vol. 51, no. 2, pp. 1167–1179, 2006.

[148] K. Ruddick, V. De Cauwer, and B. Van Mol, "Use of the near infrared similarity reflectance spectrum for the quality control of remote sensing data," in *Remote Sensing of the Coastal Oceanic Environment*, vol. 5885. International Society for Optics and Photonics, 2005, p. 588501.

[149] S. B. Hooker, A. Matsuoka, R. M. Kudela, Y. Yamashita, K. Suzuki, and H. F. Houskeeper, "A global end-member approach to derive a cdom (440) from near-surface optical measurements," *Biogeosciences*, vol. 17, no. 2, pp. 475–497, 2020.

[150] S. B. Hooker, R. N. Lind, J. H. Morrow, J. W. Brown, K. Suzuki, H. F. Houskeeper, T. Hirawake, and E. d. R. Maúre, "Advances in above-and in-water radiometry, volume 1: enhanced legacy and state-of-the-art instrument suites," Tech. Rep., 2018.

[151] S. B. Hooker, *Second SeaWiFS HPLC analysis round-robin experiment (SeaHARRE-2)*. National Aeronautics and Space Administration, Goddard Space Flight Center, 2005, vol. 212785.

[152] M. Drusch, U. Del Bello, S. Carlier, O. Colin, V. Fernandez, F. Gascon, B. Hoersch, C. Isola, P. Laberinti, P. Martimort *et al.*, "Sentinel-2: Esa's optical high-resolution mission for gmes operational services," *Remote sensing of Environment*, vol. 120, pp. 25–36, 2012.

[153] B. P. Page, L. G. Olmanson, and D. R. Mishra, "A harmonized image processing workflow using sentinel-2/msi and landsat-8/oli for mapping water clarity in optically variable lake systems," *Remote Sensing of Environment*, vol. 231, p. 111284, 2019.

[154] "ESA Sentinel-2 MSI Radiometric Performance," accessed 2022-01-04. [Online]. Available: https://dragon3.esa.int/web/sentinel/technical-guides/sentinel-2-msi/performance

[155] P. K. Roy, M. B. Roy, and S. Pal, *Advances in Water Resources Management for Sustainable Use*. Springer Nature, 2021, vol. 131.

[156] "Landsat-8 science," accessed 2022-01-04. [Online]. Available: https://landsat.gsfc.nasa.gov/satellites/landsat-8/